NTNU – Trondheim
Norwegian University of
Science and Technology

Fatigue of Extruded AA6082 and AA7108 Alloys

The Effects of Natural Ageing Compared to Artificial Ageing

Marte Brynjulfsen

Materials Science and Engineering
Submission date: June 2015
Supervisor: Hans Jørgen Roven, IMTE
Co-supervisor: Trond Furu, Hydro

Norwegian University of Science and Technology
Department of Materials Science and Engineering

Preface

This report is the result of a master's thesis done at the Department of Materials Science and Engineering at the Norwegian University of Science and Technology (NTNU), during the spring of 2015. The aim of this thesis was to investigate the effects of natural ageing compared to artificial ageing on fatigue properties in two aluminium alloys. This work is a direct sequel of the specialization project carried out by the undersigned during the fall of 2014. Some of the experimental data from the latter are presented in chapter 3.2.

First, I will like to express my gratitude to my supervisor, Professor Hans Jørgen Roven for guidance and support during this work. Further, I would like to thank Trygve Lindahl Schanche for assisting me in the heat- and metallographic laboratories, and Pål Christian Skaret for assisting me in the MTS laboratory. I will give a thanks to Yingda Yu and Christian Oen Paulsen for helping me at the EM-laboratory. In addition, I would like to thank to Hydro Aluminium and Professor II Trond Furu, my co-supervisor, for supplying the material used. At last, I will thank Thorstein J. Stedje for patience, proof reading and feedback.

I declare that this master's thesis is done independently and in accordance with the regulations at NTNU.

Trondheim, June 2015

Marte Brynjulfsen

Abstract

Heat treatable aluminium alloys might have the potential to gain unexpected increase in mechanical properties when stored at room temperature (natural ageing) after extrusion, for long periods of time. The main aim of the present work is therefore to investigate the effects of long time natural ageing on fatigue life, under constant amplitude loading in ambient air, i.e. for alloys AA6082 and AA7108.

The extruded AA6082 and AA7108 alloys have been investigated in four different temper states, T1, T4, T5 and T6. The T1 and T4 tempers represents naturally aged conditions at different storage times, i.e. more than 10 years and 3 weeks, respectively. The T5 and T6 tempers represents artificially aged conditions. The fatigue testing was performed as one-axial, high cycle fatigue, with the fatigue properties between 10^5 and 10^6 cycles to failure in focus. The relationship between fatigue strength and non-strength providing parameters such as the recrystallized layer, surface roughness, crystallographic texture and humidity have been accounted for. The different precipitated particles, providing strength, have also been considered, as they have a direct effect on the fatigue strength. To underline the fatigue properties, hardness change due to cyclic loading was measured and finally fractured surfaces were investigated.

The results show that stored aluminium alloys can gain ultimate tensile strengths comparable to heat treated conditions. Never the less, it is not always a direct relation between high tensile properties and good fatigue properties. Further, the results reveal that the naturally aged temper state (T4) and the stored temper state (T1) have the best fatigue properties. In addition, for both alloys, the peak aged condition, T6, has the poorest fatigue properties.

Sammendrag

Utherdbare aluminiumslegeringer kan ha potensialet til å få en uventet økning i mekaniske egenskaper, dersom de lagres i romtemperatur (naturlig utherding) i lange tidsperioder etter ekstrudering. Målet med dette arbeidet er derfor å undersøke effekten av langtids naturlig utherding på utmattingslevetiden, ved konstant amplitude utmatting i luft, for legeringene AA6082 and AA7108.

Ekstrudert AA6082 og AA7108 har blitt undersøkt for fire ulike tilstander, T1, T4, T5 og T6. Tilstandene T1 og T4 representerer naturlig utherdede tilstander ved ulike lagringstider, det vil si, mer enn 10 år og 3 uker, respektivt. Tilstandene T5 og T6 representerer tilstander utherdet ved forhøyet utherdingstemperatur. Utmattingstestingen er gjort ved høysyklustesting, med utmattingsegenskapene mellom 10^5 og 10^6 antall sykler til brudd i fokus. Forholdet mellom utmattingsstyrke og parametere som ikke gir styrke som, rekrystallisert sjikt, overflateruhet, tekstur og luftfuktighet har blitt tatt med i vurderingen. Utfelte presipitater, ansvarlig for styrken til hver tilstand ble også diskutert, ettersom de har en direkte effekt på utmattingsstyrken. For å underbygge de utmattingsegenskapene som ble funnet, ble hardheten målt før og etter utmatting, samt at bruddflatene ble undersøkt.

Resultatene viser at lagrede aluminiumslegeringer kan oppnå en strekkfasthet sammenliknbar med varmebehandlede tilstander. Likevel er det ikke alltid en direkte sammenheng mellom gode spenning-tøyningsegenskaper og gode utmattingsegenskaper. Videre avslører resultatene at de naturlig herdede tilstandene (T1 og T4) har de beste utmattingsegenskapene. For begge legeringer er det T6 som viser de dårligste utmattingsegenskapene.

Table of contents

Abbreviations

β'':	Hardening precipitate in AA6082
$\beta(Mg_2Si)$:	Equilibrium precipitate in AA6082
ε_f:	Elongation at fracture (ductility)
η':	Dominant peak hardening precipitate in AA7108
$\eta(MgZn_2)$:	Equilibrium precipitate in AA7108
σ_y:	Yield strength
σ_{UTS}:	Ultimate tensile strength
σ_a:	Stress amplitude
σ_{max} :	Maximum stress
EBSD:	Electron backscatter diffraction
ED:	Extrusion direction
EDS:	Energy-dispersive x-ray spectroscopy
GB:	Grain boundary
GP-zone:	Guinier Preston zone
N_f :	Number of cycles until fracture
ND:	Normal direction
PFZ:	Precipitate free zone
PSB:	Persistent slip band
R:	Stress ratio
RT:	Room temperature
SEM:	Scanning electron microscope
TEM:	Transmission electron microscope
TD:	Transverse direction

1 Introduction

Fatigue is recognized as unpredictable failure on parts subjected to a cyclic stress and can therefore cause great damage [1]. The article *A history of fatigue* by W. Schülz [2], reveals the industrial importance of fatigue failure ever since the 1830s'. Further through the history, fatigue failure has led to several minor accidents with material and financial loss, and unfortunately some lethal accidents [2, 3]. Today, more than 90 present of the failure in the industry is due to fatigue [1].

Aluminium alloys are strong, light metal alloys used in building structures, marine applications, automotive- and aerospace industry [4]. All these applications need good control of fatigue failure to prevent material, financial and human loss. Therefore, the study of fatigue failure of aluminium alloys is important.

Several aluminium alloys, like the Al-Mg-Si alloys and the Al-Mg-Zn alloys, are heat treatable and increase their strength and hardness by heat treatment. The hardening sequences of these alloys, due to heat treatments are very well established [4-7]. The hardening sequences of these alloys stored for a long time (e.g. 10 years) are not well established. The aim of this study is to investigate how storage affects the fatigue properties of extruded aluminium alloys, compared to heat treated extruded aluminium alloys. If the fatigue properties of the long term stored aluminium alloys are sufficient compared to heat treated, one or several process steps can be eliminated leading to financial advantages.

2 Theory

2.1 Aluminium

Aluminium is a light metal with a density of 2.7 g/mm^3 (1/3 the density of steel). The low weight causes a reduction in cost and emission during transportation and in construction of buildings [8]. In addition, the recycling process of aluminium is very energy efficient, where only 5% of the energy used to produce aluminium is needed to recycle it. This saves energy and reduce CO_2-emission. Aluminium may therefore be called a green metal [9].

2.1.1 The 6000- and 7000 series

There are many different aluminium alloys. Aluminium alloys are divided into series depending on the main alloying elements. Such series can be the 6000 series where magnesium (Mg) and silicon (Si) are the main alloying elements, or the 7000 series where magnesium (Mg) and zinc (Zn) are the main alloying elements. These aluminium alloys are strong in contrast to pure aluminium.

Both the 6000- and 7000 series are heat treatable, and thus they can increase their strength by heat treatment. These alloys can be used for extrusion and rolling due to their low resistance against deformation [4].

The various effects of the main alloying elements in the 6000- and 7000 series are displayed in Table 1. In addition to the main alloying elements, manganese (Mn) improves strain hardenability and increase strength by grain refinement, copper (Cu) increases strength and reduces corrosion resistance while chromium (Cr) reduces stress corrosion. Titanium (Ti) or zirconium (Zr) may be added to promote a fine grained microstructure [10].

The 7000 series is stronger than the 6000 series [11], but the 7000 series are more prone to intergranular corrosion [12].

Table 1: The effect of the main alloying elements [4, 10, 13].

Series	**Main alloying elements**	**The effect of the main alloying elements**
6000	Magnesium (Mg) 0.5-1.3 wt%	Mg: increases strength during solid solution strengthening and improves strain hardenability
	Silicon (Si) 0.4-1.4 wt%	Si: produce precipitation hardening together with Mg and increases strength and ductility
7000	Zinc (Zn) 4-6 wt%	Zn: gives a great increase in strength and permits precipitation hardening
	Magnesium (Mg) 1-3 wt%	Mg: increases strength during solid solution strengthening and improves strain hardenability

2.2 Production and extrusion of aluminium

Extrusion of aluminium alloys can produce complex shapes in long length with a relatively low cost [14]. The process steps before, during and after extrusion are illustrated in Figure 1. First, alumina reacts with carbon in a smelter, producing melted aluminium and CO_2. The molten aluminium is then casted into an extrusion billet [15], followed by homogenization. Before extrusion, the billet is preheated to reduce the deformation resistance, and thus to increase the extrusion speed [14].

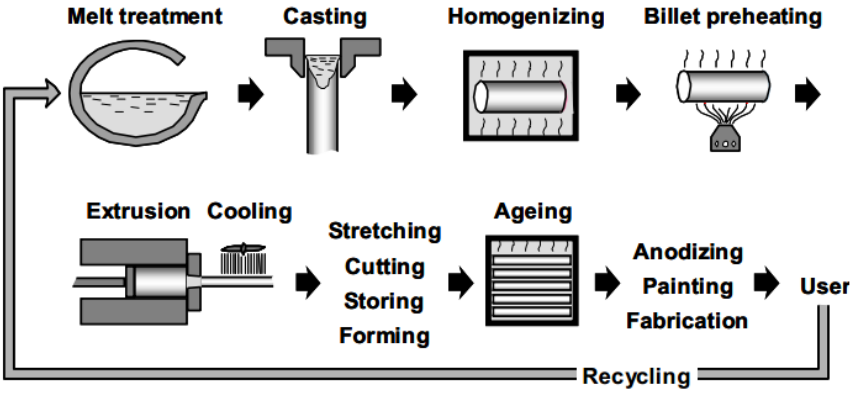

Figure 1: Process steps before, during and after extrusion [14].

During extrusion, the billet is forced through a die with a high pressure. Heat is developed due to high friction forces [16] and the temperature usually reaches a high value (~ 600ºC) [14]. The high temperature results in low deformation resistance in the material. After extrusion, the extruded product is cooled and then it can be formed, stored or artificially aged. An example of the temperature range before, during and after extrusion is illustrated in Figure 2.

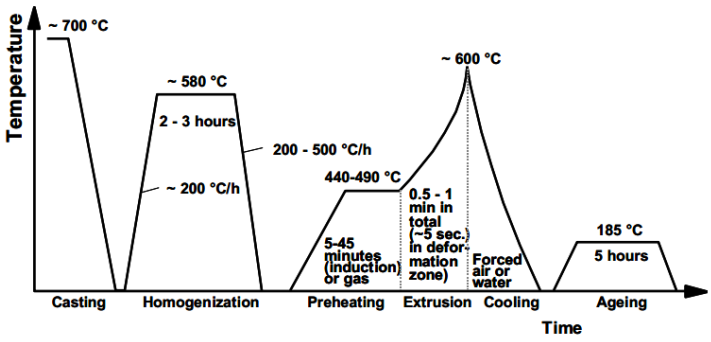

Figure 2: An example of the temperature range before, during and after extrusion [14].

2.3 The stress-strain curve

An engineering stress-stain curve is made by data from a tensile test, plotted as stress [MPa] versus strain [mm/mm], see in Figure 3 below. In a tensile test, the tensile specimen is subjected to a tensile force until fracture.

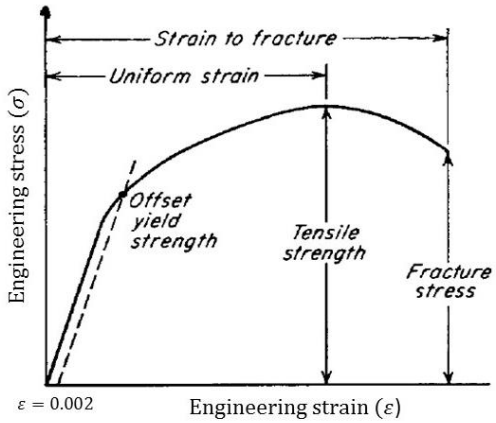

Figure 3: The engineering stress-strain curve [17].

During the linear part of the stress-strain curve, the material is not permanently deformed. This is called elastic deformation. After the linear part, the material is permanently deformed, this is called plastic deformation. The engineering stress (σ) is defined as the force (F) divided by the original area (A_0),

$$\sigma = \frac{F}{A_0} \tag{1}$$

The engineering strain (ε) is defined as the elongation of the material ($L - L_0$) divided by the original length (L_0),

$$\varepsilon = \frac{\delta}{L_0} = \frac{L - L_0}{L_0} \tag{2}$$

The stress-strain curve provides several features such as yield strength (σ_y) and ultimate tensile strength (σ_{UTS}). The yield strength is defined as the intersection between the stress-strain curve and a line drawn parallel to the curve from a strain equal to 0.002, see Figure 3. Thus, the yield strength is the stress which will produce a small amount of plastic strain.

Mathematically the yield strength is defined as [17],

$$\sigma_y = \frac{F_{strain\ offset=0.002}}{A_0} \quad (3)$$

Hence, plastic deformation is also called yielding. The maximum point of the curve equals the ultimate tensile strength and it is defined as [17],

$$\sigma_{UTS} = \frac{F_{max}}{A_0} \quad (4)$$

Another important feature from the stress-strain curve is the amount of work hardening. The amount of work hardening is the increase of stress from the yield strength to the ultimate tensile strength, hence strengthening during plastic deformation. Work hardening is defined as the increase in stress needed to induce slip as a consequence of previous plastic deformation [18]. Hence, work hardening happens as a consequence of dislocation movement and the generating of dislocations [19]. The process of slip will be further presented in chapter 2.4.

2.4 Crystal geometry and deformation by slip

2.4.1 Crystal geometry

The crystal structure of metals, as aluminium, are often described in terms of the smallest repeated entities of atoms, called unit cells. There are several different unit cells, one of them is the face centered cubic (FCC) unit cell. The FCC unit cell is a cube with an atom at each corner and at each side, and the unit cell of aluminium [18].

A crystallographic orientation can be described by Miller indices, (*hkl*)[*uvw*]. Here (*hkl*) indicates the crystallographic plane, and [*uvw*] indicates the crystallographic direction within a unit cell in xyz-coordinate system. The geometry of a cubic unit cell is illustrated in Figure 4, where the length of one side is a_0 [18].

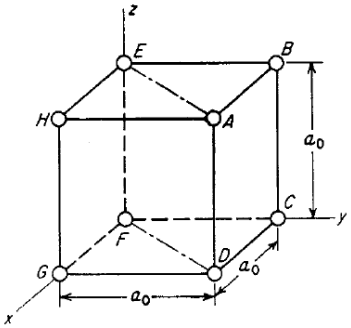

Figure 4: Geometry of a cubic unit cell [18].

2.4.2 Deformation by slip in aluminium

The most important defects in metals are called dislocations, which are abnormalities in the crystal lattice. These are often described as an extra half row of atoms in the structure, as can be seen above the line in Figure 5.

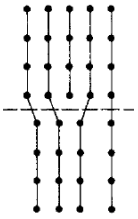

Figure 5: A schematic drawing of a dislocation [18].

During deformation of metals, dislocations glides along defined crystallographic planes in defined crystallographic directions. This process is called slip. Slip is the fundamental idea behind plastic deformation of metals. In FCC metals, as aluminium, the most favorable planes for slip are the {111} planes, and the most favorable direction of slip are the <110> direction. The most favorable planes and directions are the most close packed ones. Together these planes and directions constitutes the *slip system* of FCC metals as {111}<110>, which there are 12 possible variants [18].

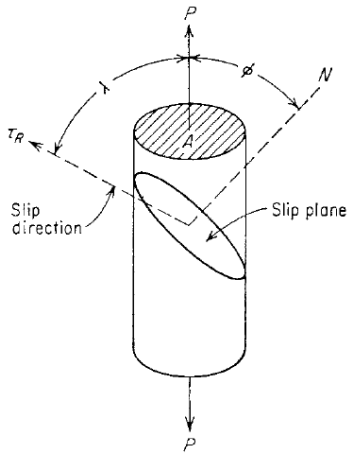

Figure 6: The resolved shear stress, τ_R, in the slip plane.

Slip occurs at the plane which experience the highest resolved shear stress. The resolved shear stress, τ_R, in the slip plane, can be illustrated as in Figure 6. The area of acting stress in the slip plane can be expressed as $A/cos\emptyset$ and the force component in the slip plane as $Fcos\lambda$, the resolved shear stress in the slip plane is then [18],

$$\tau_R = \frac{Fcos\lambda}{A/cos\emptyset} = \frac{F}{A}cos\lambda cos\emptyset = \sigma cos\lambda cos\emptyset \qquad (5)$$

From Equation 5, maximum resolved shear stress is when λ=$\emptyset$=45º, hence when the angle between the tensile load and the slip plane is 45º. If the tensile load is either normal to the slip plane (λ=90º) or parallel to the slip plane ($\emptyset$=90º), slip will not occur because there will be no resolved shear stress in the slip plane[18].

The ratio of the resolved shear stress to the tensile load is called the Schmid factor, *M*, expressed as $M=cos\lambda cos\emptyset$. Hence, the resolved shear stress in the slip plane can be expressed as,

$$\tau_R = \sigma M \qquad (6)$$

The slip system with the highest Schimd factor will be the initial operative slip system [18]. Hence, for aluminium, if some of the {111} planes are at an angle of 45º to the tensile direction, slip will easily be initiated on these planes.

2.5 Heat treatment and hardening of the 6000- and the 7000 series

Both the extruded 6000 series and the extruded 7000 series are heat treatable [20, 21], and thus their strength and hardness will be increased by the right heat treatment [22]. When the alloy is heated to an intermediate temperature (e.g. 140-185ºC), small and uniformly dispersed precipitates of a second phase will form within the original phase matrix. These particles will differ in size and composition after which temperature the alloy was heated to, as illustrated as different areas in Figure 7. The right combination of size and composition will increase the hardness and the strength. This process is called precipitation heat treatment or artificial ageing [22].

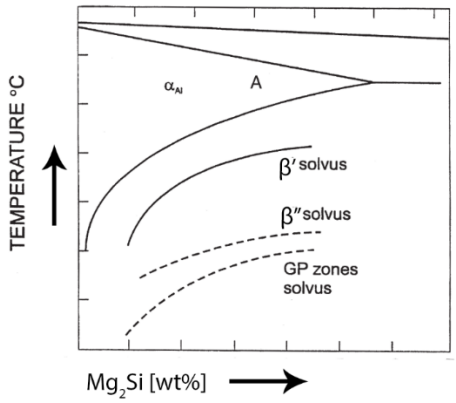

Figure 7: Schematic drawing of the different areas in the phase diagram where different particles in a 6000 alloy can be precipitated. Adapted from [4].

To increase the effect of artificial ageing, solution heat treatment can be done before ageing. The process of solution heat treatment is illustrated in Figure 8, where solution heat treatment is achieved at point 1. An alloy with a composition C_0, is heated to a temperature in the α-phase area, where it is held to get the alloying elements in solid solution before it is quenched. The quenching prevents atom diffusion of the alloying elements, and thus the super saturated solid solution microstructure (ssss) is relative soft and weak, and precipitation heat treatment must be done to strengthen the alloy. [22]

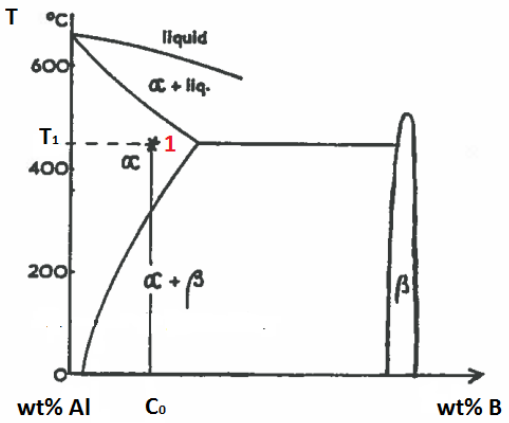

Figure 8: An imagined phase diagram of an Al-B alloy. Solution heat treatment is achieved at point 1 [4].

The temperature difference between artificial ageing and solution heat treatment is schematically illustrated in Figure 9. It should also be mentioned that if precipitation is done at room temperature, the process is called natural ageing.

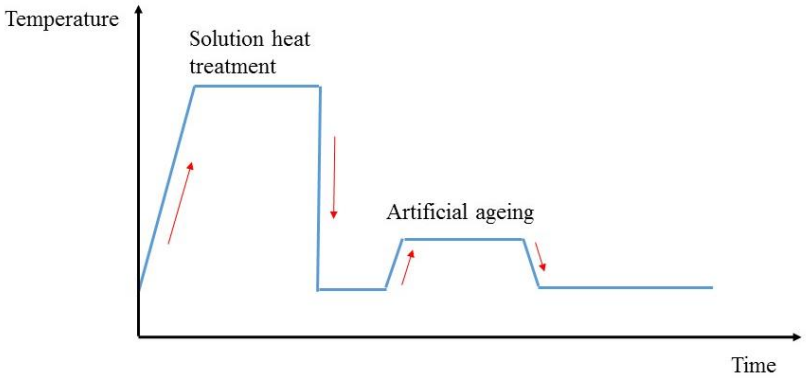

Figure 9: Schematic drawing of solution heat treatment and precipitation heat treatment. Adapted from [22].

The following sub chapters will first describe the general hardening effect from precipitated particles (2.5.1), then the ageing processes and pertaining particle precipitation of the specific alloys used in this study (2.5.2-2.5.3). At last, temper states and the effect of diffusion will be described.

2.5.1 The hardening effect from precipitated particles

The hardening effect in the 6000- and 7000 series is achieved when dislocations are prevented from moving in the atom lattice. The particles formed during artificial ageing may, due to different effects, act as dislocations barriers, and thus be the reason for the hardening effect.

The hardening effect from these precipitated particles is due to the combination of the particle density, particle coherency and particle strength, all of which, will make it harder for dislocations to move through matrix. The hardening of the 6000- and the 7000 series will give an increase in strength. The effect of the different dislocations barriers will be presented below.

The effect of particle density

As mentioned, interaction between dislocations and particles is the main reason for the increase in strength. The particle density indicates the amount of possible interactions, and it is therefore important for the increase in strength. A low particle density will give a large distance between the particles and thus, the material will be weaker due to the easy movement of dislocations and the decreased interaction between dislocations and particles [23]. The effect of particle density is illustrated in Figure 10. The linear mean free path expresses how the particle spacing, λ, is dependent on both volume fraction f and the particle radius r *[23]*,

$$\lambda = \frac{4(1-f)r}{3f} \qquad (7)$$

The importance of particle spacing and hence the volume fraction and particle radius will be described further in the next section.

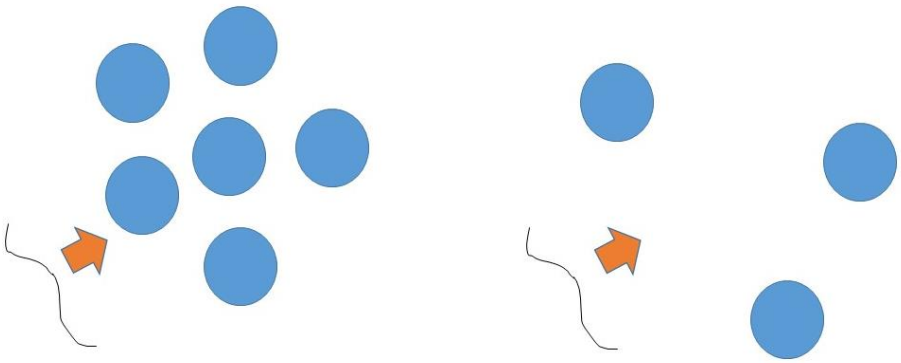

Figure 10: A dislocation line moving through matrix with different particle density [24].

The effect of particle strength

Particles can be divided into strong and weak particles, where both will give an increase in strength.

When the dislocation line move against two strong particles, separated by a distance λ, the dislocation line will bow out between the particles instead of cutting them, as in Figure 11 (2).

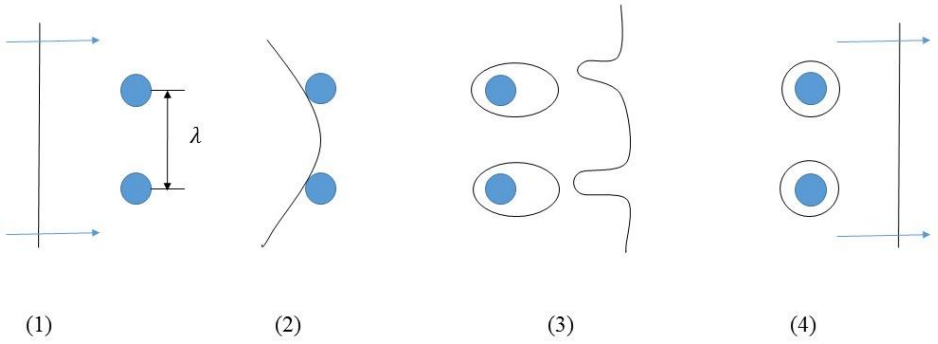

Figure 11: Drawing of a dislocation line passing strong particles. Adapted from [23].

When the dislocation line reaches a critical curvature it will bow around each particle and leave a dislocation loop, as in Figure 11 (3). These dislocation loops exerts a stress in the crystal lattice which makes it harder for the dislocations to move. The result is that the particles with the dislocations loops around them cause the matrix to strain harden rapidly. The strength contribution from the dislocation loops can be expressed mathematically as the shear stress required to bow out the dislocation around the obstacle [23],

$$\tau = \frac{Gb}{\lambda} \tag{8}$$

Where λ is the distance between the particles, G is the shear modulus and b is Burgers vector. Note that the strength contribution decreases when the distance between the particles increases.

Figure 12: Cutting of weak particles. The dislocation is indicated by⊥ [25].

When a dislocation meet a weak particle the dislocation will cut through it. This cutting process restrains the movement of the dislocation through matrix, and hence the cutting gives an increase in strength, as in Figure 12 [23]. During the cutting of particles, the energy

consumed, balances the work done by the external stress. The strength contribution can be expressed mathematically as the shear stress required to force the dislocation through the particle [25],

$$\tau = 1.5\frac{\gamma_s f}{r} \qquad (9)$$

Where f is the volume fraction of spherical particles of radius r, and γ_s is the particle-matrix surface energy. Note that the strength contribution increases when the particle radius decreases.

The effect of coherency tension

Coherency tension is caused by mismatch between the particle- and matrix lattice. This is illustrated in Figure 13. To the left, in Figure 13, it is possible to follow the lattice lines from an atom in the matrix to an atom in the particle. This is a coherent particle. To the right, it is not possible to follow the lattice lines from an atom in the matrix to an atom in the particle. This is an incoherent particle. Due to the internal tension in a coherent particle, a strain field will arise in the matrix around the particle. This strain field, called coherency tension, makes it harder for the dislocations to move, and hence there is a strengthening effect [23].

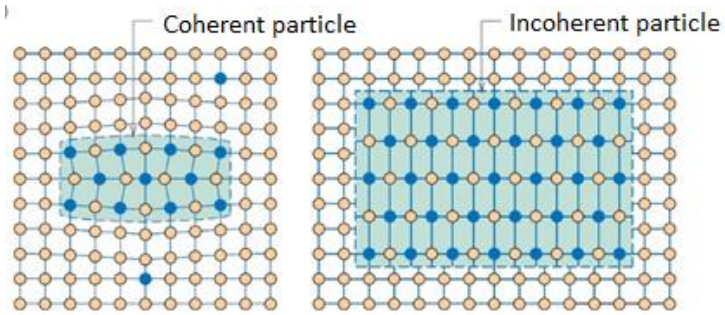

Figure 13: A coherent and an incoherent particle [22].

The effect of grain size

There is a relationship between yield strength and grain size given by Hall and Petch, indicating that the yield strength decreases, when the grain size increases. Assume a constant amount of dislocations in an area. When stress is applied, the dislocations will move against the grain boundaries. A coarse grained microstructure will contain more dislocations in one

grain than a fine grained microstructure, as illustrated in Figure 14. Therefore, a coarse grained microstructure will have more dislocations pushing on *one* grain boundary.

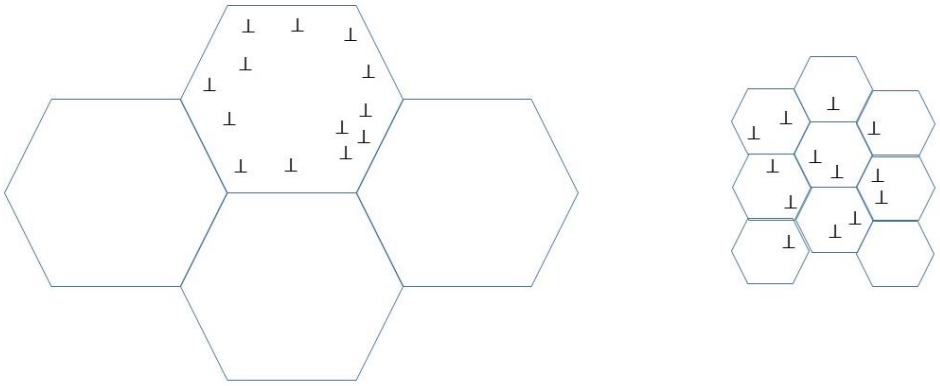

Figure 14: Grain size dependence. Drawn by the author.

Many dislocations pushing on a grain boundary can be a source of crack initiation because shear stress will build up in front of the dislocation pile up, squeeze the dislocations together and nucleate a micro crack. A micro crack can develop into a severe crack.

The Hall-Petch relationship is defined as,

$$\sigma_y = \sigma_i + kD^{-\frac{1}{2}} \qquad (10)$$

where σ_y is the yield strength, σ_i is the stress representing the overall resistance of the crystal lattice from dislocation movement. The *k* is the "locking parameter" which measures the relative hardening contribution of grain boundaries and *D* is the grain size [23].

2.5.2 Artificial ageing of the 6000 series

To achieve an increase in hardness and strength through artificial ageing of an Al-Mg-Si alloy, the alloy is heated to an intermediate temperature within the α-β- phase region either after or without solution heat treatment. At this temperature, the diffusion rates become high enough to precipitate particles. After the chosen ageing time, the alloy is cooled to room temperature.

Precipitation of particles starts with excess vacancies clustering together, and Mg and Si atoms diffusing towards them. These collections of Mg and Si atoms are called GP1-zones (Guinier Preston-zones) and precipitate as partly coherent needles along <110> directions in the aluminium crystal lattice [4]. When the GP1-zone has grown to a certain size, the β''-particle is created. This particle has a monocline crystal structure made by partly coherent needles of Mg_5Si_6 [4, 26], precipitated along <100>-directions in the aluminium crystal lattice.

The β''- particle will in turn become the larger β'-particle. This particle has a hexagonal crystal structure made by partly coherent needles (one type is Mg_5Si_3). At last, the equilibrium $\beta(Mg_2Si)$-particle is created. This is a particle with a cubic crystal structure made of incoherent, square sheets [4]. When the β-phase is created, the alloy is in an overaged state.

Thus, the precipitation sequence of the 6000 series is,

$ssss \rightarrow GP1 \rightarrow \beta''(Mg_5Si_6) \rightarrow \beta' \rightarrow \beta(Mg_2Si)$ [26-28]

As mentioned, the precipitated particles formed in this alloy are not fully coherent and therefore *not* surrounded by coherent-tension. In this alloy, the hardening effect will be given by the particle density and the strength of the particles [4, 5].

The GP-zones will increase the hardness, but β'' or a mix of β'' and β' are responsible for the peak hardness [4, 26]. The hardness decrease between formation of β''- and β'-particles, and thus the β''-particle is classified as the most significant hardening phase [5]. When $\beta(Mg_2Si)$ is present, the hardness is low. The β-particle is large due to long diffusion time. Then the particle density will be low and the dislocations can easily move between the particles. The hardness contribution of the different particles are illustrated in Figure 15.

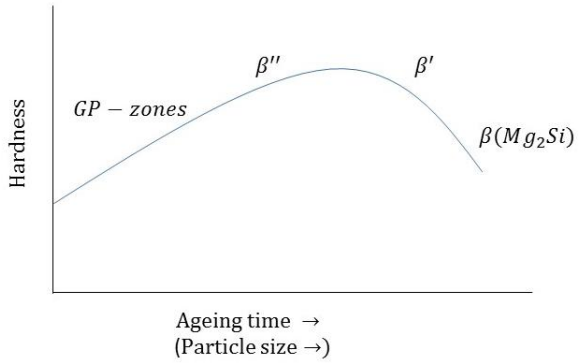

Figure 15: Hardness versus ageing time. Adopted from [23].

2.5.3 Artificial ageing of the 7000 series

To achieve artificially ageing of an Al-Mg-Zn alloy, the alloy is heated to an intermediate temperature within the α-β- phase region either after or without solution heat treatment. At this temperature, the diffusion rates become high enough to precipitate particles.

Precipitation of particles starts with excess vacancies clustering together and Mg and Zn atoms diffusing towards them. This collection of atoms is called GP-zones (Guinier Preston-zones) and exist both as GPI-zones and GPII-zones. GPI-zones are formed during storage at room temperature or artificial ageing at 140-150 ºC, independently of the quenching rate [6, 7]. GPII-zones are formed during quenching after solution treatment above 450 ºC followed by ageing at temperatures above 70 ºC [6]. The GP-zones are coherent spheres of magnesium and sink [4].

In turn, a GP-zone grows into a η'-particle. This particle has a hexagonal crystal structure [7], with partly coherent plates in the $\{111\}$ - aluminium planes [4]. At last, the equilibrium phase, the η-particle is created [7]. This phase is hexagonal and not coherent with the matrix. The η-particle have a composition of $MgZn_2$ [4, 7].
Thus, the precipitation sequence for the 7000 series is,

$ssss \rightarrow GP(I,II) \rightarrow \eta' \rightarrow \eta(MgZn_2)$ [6, 7, 29]

Both the GP-zones and the η'-phase contribute to give a hardening effect [4, 5]. The GP-zones are coherent and therefor they will give an increase in strength due to coherency tension in the crystal lattice [5], as described in chapter 2.5.1.

The η'-particle is a metastable phase and it is responsible for the peak hardening in this alloy [4, 6]. The hardening contribution from the η'-particle is due to its fine dispersion. This will give an increase in hardness because the dislocations will interact with the η'-particle by either cutting the particle or leaving a dislocation loop around it, as described in chapter 2.5.1

When $\eta(MgZn_2)$ is present, the hardness is low. The η-particle is large due to long diffusion time. Then the particle density will be low and the dislocations can easily move between the particles. The hardness contribution of the different particles are illustrated in Figure 16.

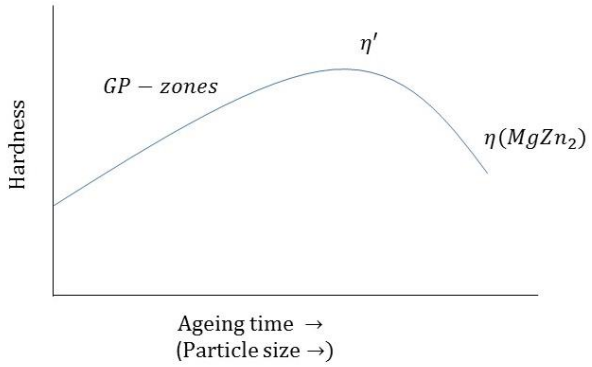

Figure 16: Hardness versus ageing time. Adopted from [23].

As a final note, artificial ageing can also be done as a two step process for both the 6000- and the 7000-series. In a two step ageing process the artificial ageing is done at two temperatures. At the first temperature the time is equal for all samples, and at the second the samples are taken out at different times depending on the precipitates desired. A two step ageing process can be done to narrow the so-called precipitate free zones (PFZ). The PZF normally lowers the mechanical properties of aluminium alloys [4].

2.5.4 Temper states

To designate the heat treatment done on aluminium, temper states are used. Some of the most used temper states are explained in Table 2. In this master thesis, these temper states designations will be used.

Table 2: Temper states [10].

Temper state	Description
T1	Cooled from elevated temperature shaping process and naturally aged
T4	Solution heat treated and naturally aged to a stable condition
T5	Cooled from elevated temperature shaping process and artificially aged to peak hardness
T6	Solution heat treated and artificially aged to peak hardness

2.5.5 Diffusion

Diffusion plays a crucial role during the formation of precipitated particles. Both time and temperature are important factors, where temperature has the most influence of the two. The diffusion coefficient D, is exponentially dependent on temperature and given as,

$$D = D_0 \, exp\left(-\frac{Q}{RT}\right) \tag{11}$$

where D_0 is a temperature independent constant, R is the gas constant, T is the temperature and Q is the activation energy. The diffusion rate J, will increase with increasing diffusion coefficient according to Ficks first law,

$$J = -D\left(\frac{dC}{dx}\right) = D_0 \, exp\left(-\frac{Q}{RT}\right)\left(\frac{dC}{dx}\right) \tag{12}$$

Where dC/dx, the change in concentration versus distance, x, is time dependent.

2.6 Fatigue

Fatigue is a failure mechanism recognized as a sudden collapse of metal subjected to a cyclic stress after a considerable amount of service time. When a metal is subjected to a cyclic stress, it can fail at lower stresses than if the load were static [1], even at stresses lower than the yield strength [30]. This makes fatigue failures difficult to anticipate [1].

The mechanism of fatigue failure can be illustrated with Figure 17. This figure illustrates a collection of grains. Grain "A" has slip planes parallel to the maximum shear stress in the glide plane. At a certain level of shear stress, the dislocations in "A" will slip (plastic deformation), even if all the other grains only experience elastic deformation.

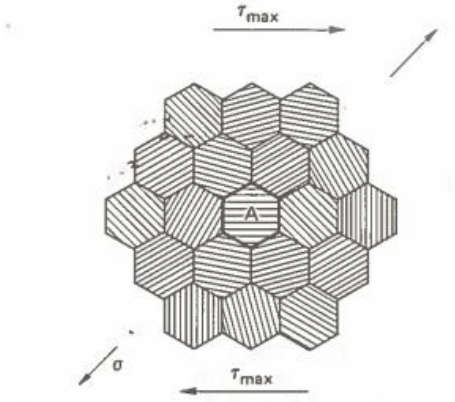

Figure 17: An aggregate of grains, the grain "A" is in the middle [30].

Therefore, grain "A" will yield before the collection of grains will yield. In Figure 18, the yield point of "A" is indicated as σ_2, while the yield point of the collection of grains is given as σ_1.

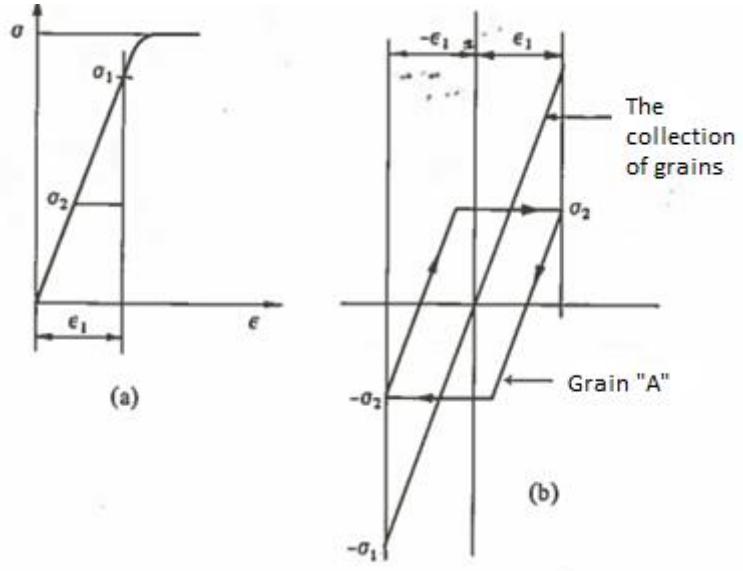

Figure 18: Stress cycles causing fatigue [30].

The plastic deformation on grain "A", is small compared to the total volume of grains, and therefore the slip in "A" alone would not make the material as such to deform plastically during tension. For every stress cycle, slip in grain "A" will cause a small amount of disorder in grains nearby. After many cycles, the dislocations in grain "A" will have slipped many times, and the total amount of disorder and stress concentration in the neighboring grains will increase. Slip may therefore also occur in the neighboring grains of "A", before the yield strength, due to the high stress concentrations induced by grain "A" [30].

Three factors are necessary for fatigue to happen,

i) Maximum tensile stress of sufficiently high value
ii) A large enough fluctuation of applied stress
iii) A large enough number of cycles of the applied stress

Several other factors may also influence fatigue like metallurgical structure and corrosion [1].

2.6.1 The SN-curve

Fatigue data can be presented as a SN curve, where S stands for stress and N for number of cycles until failure, displayed in Figure 19. The fatigue strength is the stress level where failure will occur for a specified number of cycles. The number of cycles at failure is called the fatigue life, N_f [31]. The fatigue strength and fatigue life is marked on Figure 19.

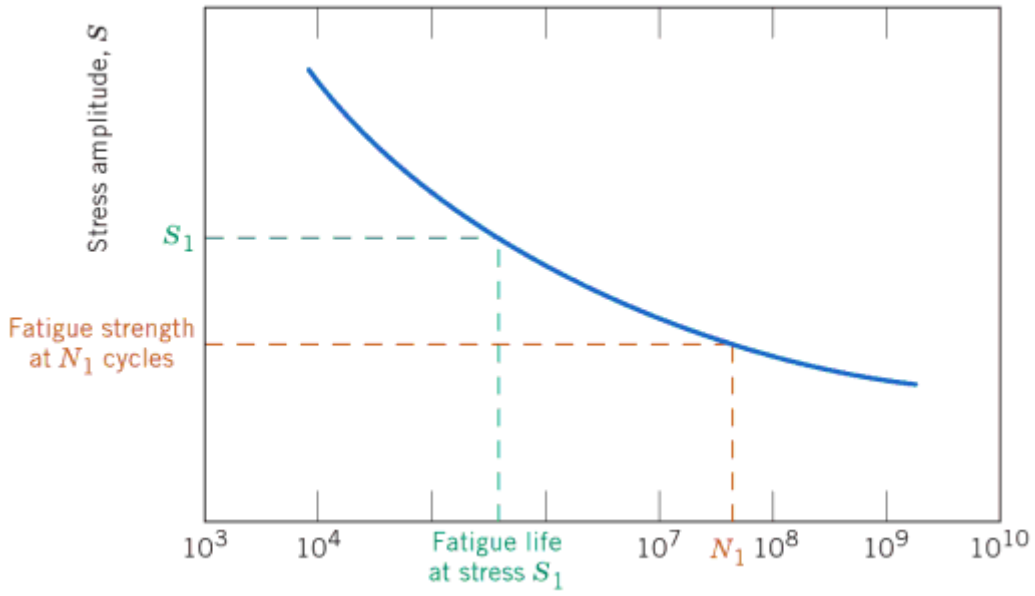

Figure 19: SN curve for a material without a fatigue limit [31].

Some metals, like titanium and steel, have a so-called fatigue limit, where the SN-curve becomes horizontal at a limiting stress, and the metal can endure an infinite number of cycles. Aluminium, on the other hand, does normally not experience a fatigue limit and therefor the SN-curve will gradually decrease until failure at low stresses. Usually for metals without a fatigue limit, the limit is chosen to be a sufficient number of cycles, often $5 \cdot 10^8$ cycles [1]. As a approximation, the fatigue limit of aluminium can be calculated as 1/3 of the yield strength [32].

The stress plotted in the S-N curve is usually the alternating stress (σ_a) from the fatigue stress cycle, described in Figure 20. The S-N curve is also plotted for one fixed value of stress ratio (R), amplitude ratio (A) or the mean stress (σ_m). The mean stress is one half the stress range (σ_r). These are all expressed mathematical in Equations 13-17.

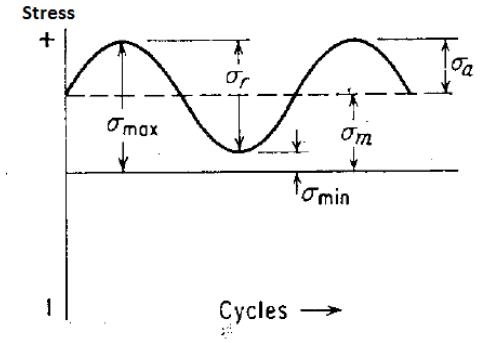

Figure 20: A fatigue stress cycle [1].

$$\sigma_r = \sigma_{max} - \sigma_{min} \quad (13)$$

$$\sigma_a = \frac{\sigma_r}{2} \quad (14)$$

$$\sigma_m = \frac{\sigma_{max} + \sigma_{min}}{2} \quad (15)$$

$$R = \frac{\sigma_{min}}{\sigma_{max}} \quad (16)$$

$$A = \frac{\sigma_a}{\sigma_m} \quad (17)$$

The stress ratio (R) indicates what type of fatigue test that has been done. When R=-1 the test is done with reversed stress, see point a on Figure 21. When R=0, the test is done with repeated stress, see point b on Figure 21. When R=0.1, the test is called a tension-tension test with repeated stress, as point c on Figure 21.

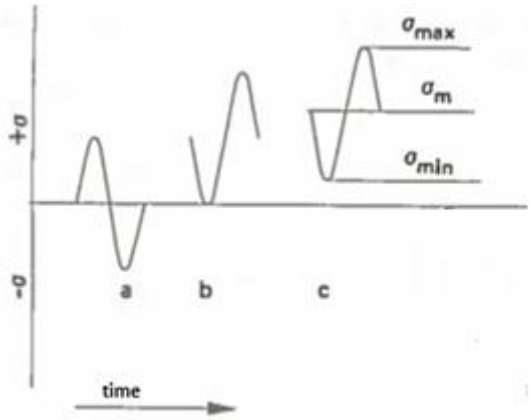

Figure 21: Stress variations during fatigue testing, a) indicates R=-1 and b) indicates R=0 and c) indicates. R>0, e.g. R=0.1 [30].

To determine a SN curve, 8-12 different loads are usually used. Every load will constitute one point on the SN curve. The first specimen is usually tested with a high stress, where failure is expected after a short number of cycles. For materials without a fatigue limit, like aluminium, the stress used is decreased for every specimen until the number of cycles to failure are at a given number (usually $5 \cdot 10^8$) [1]. This number is called redeemed run outs (RO), which is then the chosen fatigue limit.

When produced, machined or polished, no fatigue specimen will be exactly the same, with the exact same surface finish or composition. Both inclusions in the material and scrapes in the surfaces may induce a fatigue crack. Therefore, the fatigue life can be very different for two specimens tested under identical conditions. To make a SN-curve more exact, several specimens should be tested to determine the spread. The average of the spread will be more accurate than the value given by one specimen [1].

Fatigue is divided in to low cycle fatigue, where the number of cycles are less than 10^4, and high cycle fatigue, when number of cycles are more than 10^4. Low cycle fatigue is strain controlled, while high cycle fatigue is stress controlled. In this master thesis, fatigue properties during high cycle fatigue was investigated, and hence only high cycle fatigue will be described.

During high cycle fatigue the deformation is mainly elastic due to low stresses, but locally the metal deforms plastic, as described in the beginning of this chapter. The SN-curve during high cycle fatigue may be described by the Basquin equation,

$$N\sigma_a^p = C \tag{18}$$

Where N is number of cycles, σ_a is the stress amplitude, and p and C are empirical constants [1].

2.6.2 The Goodman diagram

The Goodman diagram illustrates the influence of changed mean stress (σ_m) on the stress range (σ_r), illustrated in Figure 22. There is a limiting stress range for every value of mean stress that can be withstood without failure. Therefore, the Goodman diagram illustrates the variation of the limiting stress range with mean stress. The stress range becomes zero when the mean stress equals the ultimate tensile strength. Note that when the mean stress increases, the fatigue test becomes more tensile. Every Goodman diagram is made for one fixed number of cycles [1].

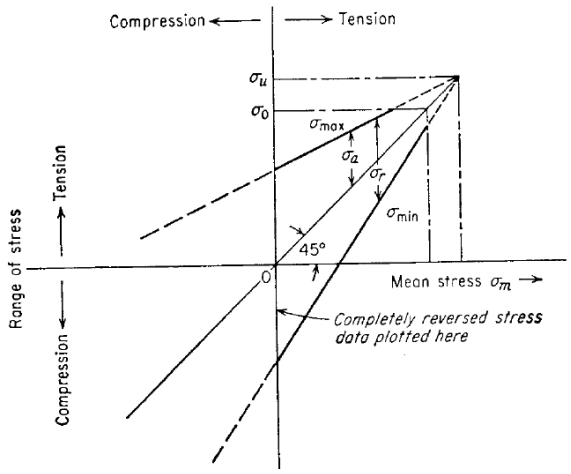

Figure 22: The Goodman diagram [1].

2.6.3 Cyclic softening and cyclic hardening

Cyclic straining of precipitation harden alloys (as the 6000- and the 7000 series) can change the geometry and distribution of the precipitates, and alter the dislocation-particle interaction. These changes can lead to softening or hardening of the alloy.

Hardening or *cyclic hardening* happens when the dislocation density increase or due to the interaction between dislocations and particles during the cyclic straining.

Softening or *cyclic softening* is promoted if the precipitated particles present are easily sheared by dislocations and closely spaced and coherent with the matrix. The formation of persistent slip bands (PBS) in precipitated alloys is a major cause of cyclic softening [33]. PBS are embryonic fatigue cracks that opens into wide cracks on the application of small tensile strains [1]. On a microscopic scale, PBS can be seen as extrusions or intrusions on the metal surface, this topic will be dealt with in chapter 2.7.3.

2.6.4 The influence of surface roughness

As mentioned before, a fatigue fracture often initiate at the surface, and hence the surface roughness plays a crucial role on the fatigue strength. Different surface finishes will affect the fatigue life, and a smooth surface will give the longest fatigue life. Scratches oriented normal to the tensile direction will affect the lifetime more than scratched oriented parallel to the tensile direction [1].

To measure the surface roughness a statistical description like *middle line average* can be used. Middle line average is also termed the average surface roughness, R_a [34]. To measure the R_a-value, a diamond tip moves over the surface and register the surfaces topography. This movement is registered by a computer which plots the hight above or below the middle level against the length the diamond has moved. The R_a-value expresses the area between the displacement curve and the middle level.

2.7 Fracture

The main types of fractures are brittle, ductile and fatigue fractures. The most accurate way of defining a fracture is to study the fracture surface and then decide the fracture type depending on features on the fractured surface [35]. The different types of fractures will be presented in this chapter.

2.7.1 Ductile fracture

Ductile fractures are associated with plastic deformation leading to a localized reduction in area called necking, followed by fracture called rupture. A ductile fracture in aluminium can be a cup-and-cone fracture (to the left in Figure 23) or a shear fracture (in the middle of Figure 23) [36]. On a macroscopic scale, the ductile fractured surface is grey with fibers and with a great amount of localized deformations, as necking [35]. Shear fracture will be further described as part of the fractures in this study were shear fractures.

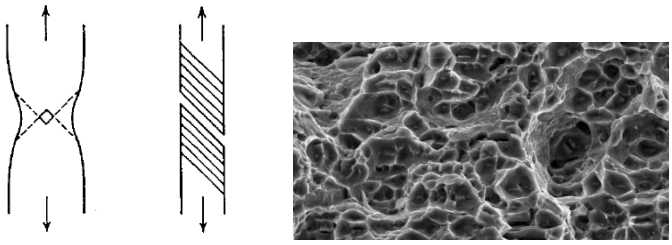

Figure 23: A cup-and-cone fracture to the left, a shear fracture in the middle [36] and dimples (micro voids) to the right adopted from [35] .

A shear fracture is due to extremely localized plastic deformation, e.g. shearing of atomic bonds. Shear fractures happens at atomic planes with low resistance against shear. The crack follows the path of maximum shear stress in the slip plane. Maximum shear stress in the slip plane is due to applied stress and voids created between inclusions and matrix. Usually, such fractures are initiated in the middle of the sample [37].

On a microscopic scale, a ductile fracture is transgranular [35], which means that the crack propagates through the grains instead of along the grain boundaries. On a microscopic scale, the surface of a ductile fracture consists of dimples (micro voids), as can be seen to the right in Figure 23, which form during creation and growth of the micro cavities. The geometrical form of the dimples depends on how the forces have worked, see Figure 24.

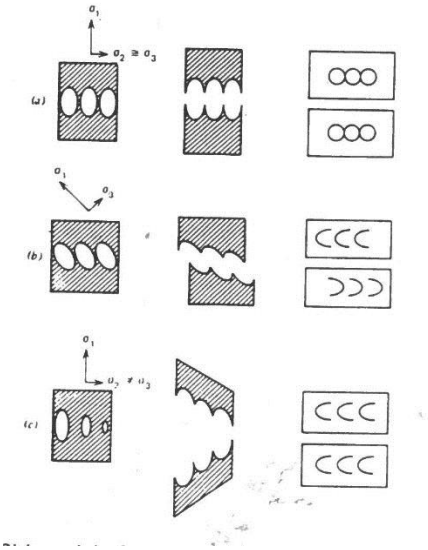

Figure 24: The effect of the different direction of the forces on dimples, a) tensile, b) shear and c) tearing[35].

2.7.2 Brittle fracture

A brittle fracture occurs rapidly, very often normal to the tensile stress, as in Figure 25. On a brittle fractured surface, there is no evidence of deformation, thus the surface is planar with close to zero plastic deformation [36].

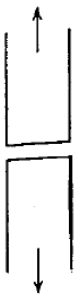

Figure 25: A brittle fracture [36].

The process of a brittle fracture can be divided into three parts. First, dislocations will pile up at an obstacle (e.g. a grain boundary) in the slip plane due to plastic deformation. Second, shear stress will build up in front of the pile up, squeeze the dislocations together and nucleate a micro crack. Third, it is a distinct growth stage, where an increased stress, called fracture stress, is required to propagate the crack.

On a macroscopic scale, a brittle fracture has a bright or shiny surface. Investigations on a microscopic scale will determine if the fracture is transgranular or intergranular. In an intergranular fracture, the crack will propagate along the grain boundaries and the grains will appear as facet surfaces (Figure 26a), while in a transgranular crack the crack propagated through the grains (Figure 26b)

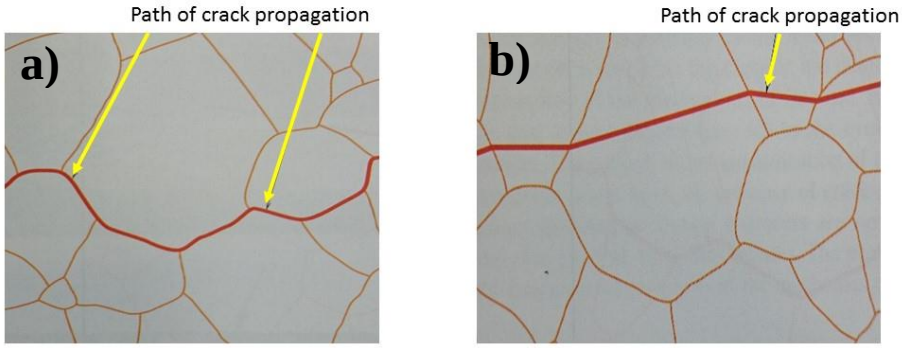

Figure 26: a) An intergranular crack, and b) a transgranular crack [22].

2.7.3 Fatigue fracture

The fluctuating stress conditions during a fatigue fracture causes strong, local stress concentrations, which may lead to cracking after a considerable amount of time [35]. Usually a fatigue fracture is initiated at the surface, most likely where the stress concentration is high, like a sharp corner or a scrape [35]. The stress concentration in the crystal lattice may also be high due to inclusions, and therefore, this is also a possible initiation site for fatigue [1].

A fatigue fracture has usually little visible deformation. The fracture surface is easy to recognize due to the appearance of a smooth section and a rough section. The smooth section is due to the fatigue crack propagation and the rough section is a result of rapid failure in a ductile or brittle manner when the load became too high for the cross section to carry. A typical fatigue fracture is illustrated in Figure 27.

Figure 27: A fatigue fracture[31].

The structural process of fatigue can actually be divided into four stages [1],

Stage 1: Crack initiation

Stage 2: Slip-band crack growth (stage I growth)

Stage 3: Crack growth on planes of high tensile stress (stage II growth)

Stage 4: Ultimate ductile failure

As described in chapter 2.6, grains with slip planes parallel to the shear stress will slip, and form slip lines, long before the entire material slips. Slip lines are formed after only a few thousand cycles, and many parallel slip lines constitutes a slip band. Slip bands can have different structural forms as slip-band intrusions or slip-band extrusions as illustrated in Figure 28. Slip-band intrusions or slip-band extrusions are structural features unique for fatigue and can act as places of **crack initiation**. Cracks are never the less mostly initiated at geometrical stress concentrations such as, scrapes or sharp corners, i.e. described above[1].

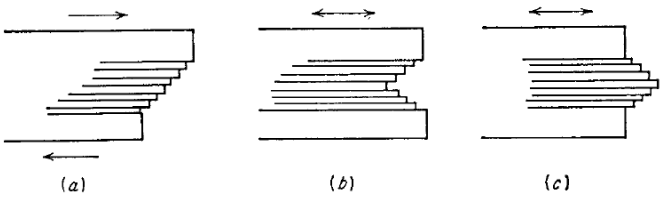

Figure 28: a) static deformation, b) slip-band intrusion and c) slip-band extrusion[1].

Slip band crack growth, also called **stage I growth**, is the first part of the crack growth. At this stage, cracks grow along slip bands. These slip bands are formed as a consequence of the highest resolved shear stress in slip planes at an angle of 45º to the applied load, and hence the slip bands are formed at this angle and the cracks propagates along these slip bands. The fractured surface of stage I cracking are more or less featureless.

Stage II growth, or crack growth on planes of high tensile stress, starts after crack propagation through a few grains, when well defined cracks propagates normal to the applied load [1]. Figure 29 illustrates the differences between stage I and stage II growth.

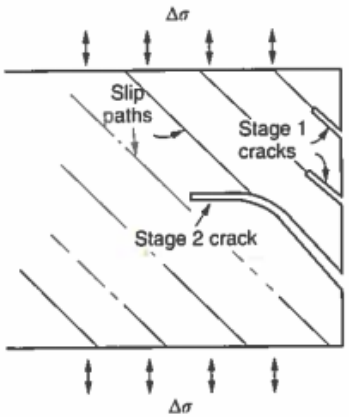

Figure 29: Schematic drawing of stage I and stage II growth [38].

The fractured surface of stage II growth shows striations. Striations are in microscopic size and may be seen with an electron microscope. One striation represents normally the increase in distance that a crack tip advance in one cycle. The width of the striations increase with an increase in stress range [31]. A collection of striations is called a *beachmark*, one beachmark can contain thousands of striations and beachmarks are visible to the unaided eye. Beachmarks are series of rings indicating the progress of fracture, progressing inward from the initiation point of the fracture [1]. Every beachmark represents a period of time where a crack has grown [31]. Beachmarks and striations represent the region of fatigue crack propagation. The absence of beachmarks or striations does not disprove that a fracture is a fatigue fracture [31].

When a crack reaches a certain length and the cross section no longer can support the load, failure will occur. Hence, the ultimate failure occurs rapidly [1]. The entire process of a fatigue failure is illustrated in Figure 30.

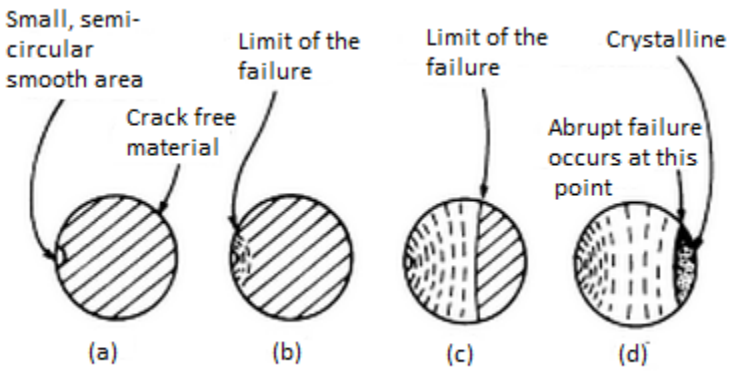

Figure 30: The process of fatigue failure [39].

2.8 Vickers hardness

Hardness is the measure of a materials resistance to localized plastic deformation. There are several hardness tests and one is the Vickers hardness (HV). In the Vickers hardness test, a diamond intender is forced into the sample and the size of the mark is measured. Vickers hardness, HV, is defined as [40],

$$HV = 1.854\frac{F}{d^2} \qquad (19)$$

Where F is force and d is the indenter diagonal in mm.

2.9 Texture

When a metal undergoes a large amount of deformation (e.g. extrusion) or recrystallization during heat treatment, the grains will develop a preferred orientation, called texture [23]. When large populations of grains have a tendency of the same orientation, this will have a major impact on the mechanical properties in the different testing directions.

To express the texture orientation, the orientation of one grain must be described relative to a reference system. For an extruded, flat plate this reference system usually consists of the extrusion direction (ED), the transverse direction (TD) and the normal direction (ND). To

express the grain orientation as (*hkl*)[*uvw*], the plane (*hkl*) is a plane parallel to the extrusion plane, and the direction [*uvw*] is parallel with ED.

To present texture data obtained by a scanning electron microscope (SEM), pole figures can be used. The (100)-pole figure is constructed in Figure 31. In Figure 31a) a cubic crystal is located inside the Ewald sphere and the stereographic projections of three {111} planes are illustrated. In Figure 31b) the ED plane with the projection of the (100) poles is shown, and Figure 31c) shows a contour map of the (100) pole density distribution [41].

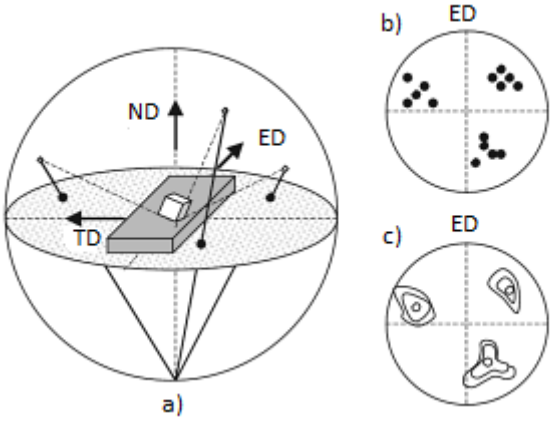

Figure 31: Construction of the (100)-pole figure[41].

Pole figures can be made for an area of the sample and then contain information about the orientation *density*, in other words, the texture of the sample.

2.10 Scanning electron microscopy (SEM)

A scanning electron microscope (SEM), is a microscope where an electron beam is transmitted towards a metal and electrons are emitted from the metal. These emitted electrons are captured by a detector, which converts the signal into an image. The advantage of using an electron microscope is the possibility of a much higher resolution and depth of field, than by using an ordinary light optical microscope. A high depth of field is important for fracture investigations. A SEM is also useful when investigating texture by using the electron backscatter diffraction (EBSD).

When an electron beam is transmitted towards a metal surface it will produce two kinds of emitted electrons, backscattered electrons (BE) and secondary electrons (SE). The

backscattered electrons are a fraction of the electrons from the electron beam, which are released from the metal.

There are two sources that can produce secondary electrons, the backscattered electrons or the electron beam. The secondary electrons, are electrons emitted from the metal as the electron beam or backscattered electrons travels throughout the metal and releases them. Only electrons in the upper part of the metal can be emitted as secondary electrons. Any deeper than 5λ, and the secondary electrons will not be able to escape from the metal. The difference between backscattered- and secondary electrons are illustrated in Figure 32 below.

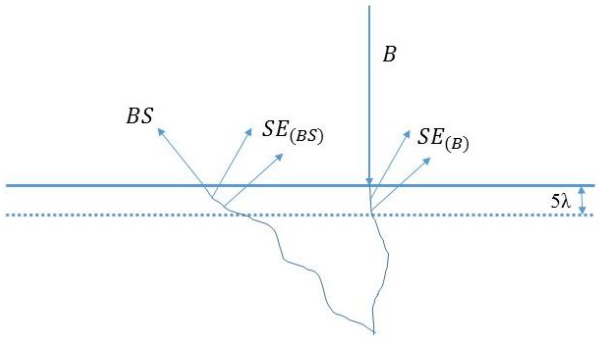

Figure 32: The difference between backscattered- and secondary electrons, adapted from [35].

2.10.1 Fractography

When investigating the fracture on a specimen, only backscattered or both backscattered- and secondary electrons are used to give information about the topography. The usage of both will provide a clearer image. The amount of electrons that strikes the detector will provide information about the topography. If few electrons strike the detector, there is most likely a groove, where the electrons got stuck. A shallow surface will provide more electrons to the detector.

A good depth of field is important when investigating the fractured surface of a specimen. Depth of field is defined as the maximal difference in height where the image of the specimen surface is in focus. Depth of field depends on the working distance, the distance from the aperture to the sample. When the working distance increases the depth of field increases[35].

2.10.2 Energy dispersive spectroscopy

Energy dispersive spectroscopy (EDS) is a technique used to do element analysis. EDS analysis is done with a SEM. When an electron beam impacts the sample, a x-ray beam will be emitted from the sample. X-rays from different elements, will have different wave lengths called characteristic x-rays. Characteristic x-rays are produced when a primary electron from the electron beam interacts with an electron in the sample. The primary electron can ionize the electrons in the sample on impact, by making them move from one electron shell to another, hence the atom is excited. The x-rays that are emitted when the electron move from one shell to another are characteristic for each element, and hence the elements can be detected.

2.10.3 Texture analysis

Electron backscatter diffraction (EBSD) is a technique used to examine the crystallographic orientation, hence the texture of a material. EBSD analysis is done with a SEM. An electron beam is transmitted towards the sample, and backscattered electrons are diffracted towards the EBSD sensor with a phosphor screen. The sample is tilted 70º to increase the amount of backscattered electrons[35, 42]. When the backscattered electrons impacts the phosphor screen, Kikuchi bands are formed [43]. Kikuchi bands are illustrated to the left in Figure 33.

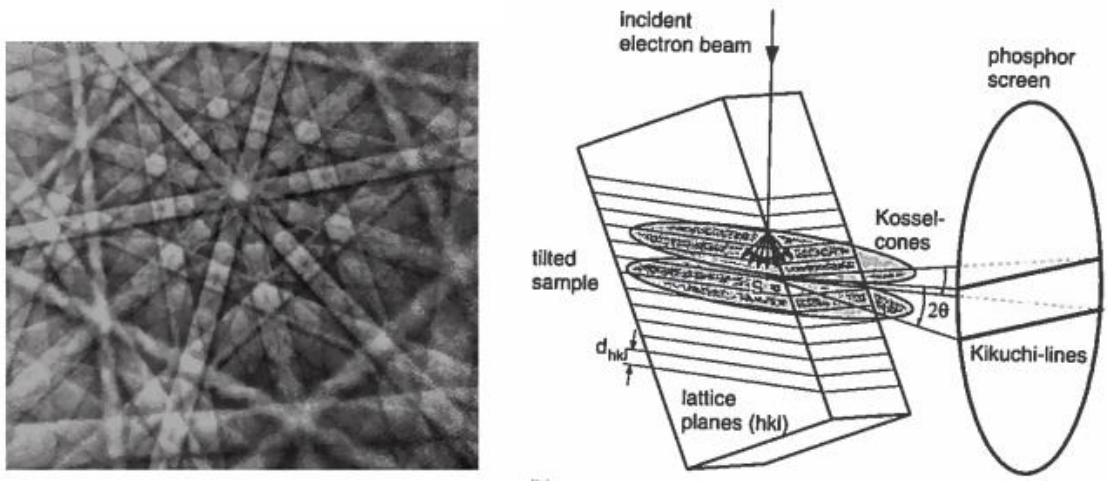

Figure 33: Kikuchi bands to the left, and formations of them to the right [43].

Each Kikuchi band is a the result of a diffracting plane in the crystal lattice, where the middle line of the band is a projection of the diffracting plane. The intersection between the middle lines represents the direction of a crystal axis [35]. Hence, the Kikuchi patterns are a projection of the angular relationships in the crystal [42]. The Kikuchi bands are related to Braggs law of diffraction, $2d_{hkl}\sin(\theta_{hkl}) = n\lambda$, because the angular width of the Kikuchi bands are twice the Bragg angle θ_{hkl}. The formation of a Kikuchi band is illustrated to the

right in Figure 33. By interpreting the Kikuchi bands, the crystal orientation can be obtained [43].

After the backscattered electrons have impacted the phosphor screen the signal is led through a TV-camera into a processor and interpreted by a computer. The relationship between the Kikuchi bands and pole figures is illustrated in Figure 34 [42].

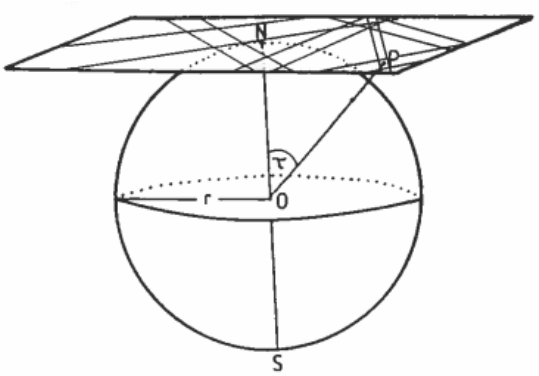

Figure 34: The relationship between the Kikuchi bands and pole figures [42].

3 Materials and experimental procedure

In this study, examinations of AA6082 and AA7108 extruded aluminium profiles have been conducted. The delivered materials and the production parameters will be presented first (chapter 3.1), followed by the material properties revealed during the previous specialization project (chapter 3.2), and at last the experimental procedures of the master work (chapter 3.3).

3.1 Delivered material

The examined materials were delivered from Hydro Aluminium Profiles AS at Raufoss, and arrived as two extruded aluminium profiles. The cross section of the profiles are seen in Figure 35. The delivered profiles were an Al-Mg-Si alloy (AA6082) and an Al-Zn-Mg alloy (AA7108) with thickness, 3 mm and 10 mm, respectively. The exact composition of the two profiles are displayed in Table 3.

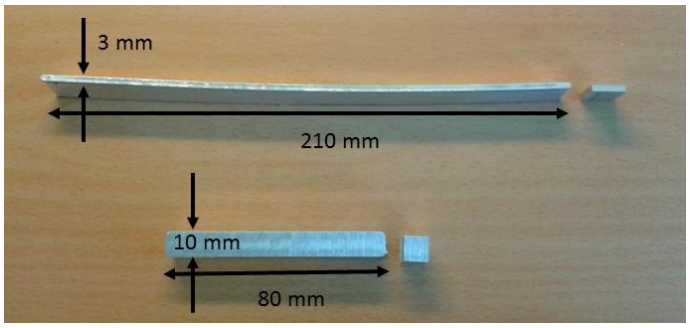

Figure 35: Cross section of delivered material. The profile at the top is AA6082 (3 mm) and the profile below is AA7108 (10 mm).

Table 3: Exact composition of AA7108 and AA6082 in wt%.

The main alloying elements of each alloy are highlighted in blue.

	Al	Zn	Si	Mg	Cu	Mn	Fe	Ti	Cr	Ni	Sn
AA6082	97.55	0.007	1.03	0.65	0.002	0.53	0.19	0.01	0.00	0.002	0.000
AA7108	93.63	5.49	0.07	0.60	0.03	0.003	0.16	0.01	0.001	0.003	0.001

3.1.1 Production and extrusion of delivered material

Both profiles were extruded at Hydro Aluminium Profiles AS at Raufoss. Homogenization parameters and extrusion data are displayed in Table 4 and Table 5, respectively [44, 45]. Note the extrusion years, i.e. storage periods of 14 years (AA6082) and 10 years (AA7108).

Table 4: Homogenization parameters [44, 45].

Alloy	Heating rate to homogenization Temperature	Homogenization temperature/holding time	Cooling method
AA6082	200 ºC/hour	580 ºC/ 2 hours	Air cooled
AA7108	100 ºC/hour	500 ºC/ 3.5 hours	Air cooled

Table 5: Extrusion data [44, 45].

Alloy	Charge	Billet temperature	Ram speed	Extrusion year
AA6082	7609	515 ºC	900 mm/min	2001
AA7108	2662	494 ºC	4.2 mm/min	2005

3.2 Material properties

In the specialization project previous of this master thesis, several material properties needed for this thesis were collected. These material properties will be presented in this sub chapter. The details of the experimental procedure to abduct these results will also be presented.

3.2.1 Ageing curves

In order to age the fatigue specimens to the different temper states, ageing curves were made. The aim of these curves was to establish the T1, T5, T6 and T4 temper states. The definitions of these temper states are repeated in Table 6.

Table 6: Definition of the temper states.

T1	T5	T6	T4
As delivered material, (extruded and stored)	Directly artificially aged to peak hardness	Solution heat treated and artificially aged to peak hardness	Solution heat treated and naturally aged to a stable hardness

The directly artificial ageing of AA6082 was done in an oil bath at 185ºC. The samples were taken out of the oil bath at different times and the hardness (HV1) was measured. The samples which were solution heat treated before artificially aged, was solution heat treated at 540ºC for 20 minutes, quenched in water, held at room temperature for 10 minutes and then artificially aged the same way as samples directly artificially aged. The naturally aged sample was solution heat treated at 540ºC, quenched in water and stored at room temperature. The hardness was measured until it was stable.

The artificial ageing curve of AA6082 is presented in Figure 36, where the temper states T1, T5 and T6 are marked with red arrows. The natural ageing curve of AA6082 is presented in Figure 37, where the T4 temper state is marked with a red arrow. The details of the AA6082 temper states are summed up in Table 7.

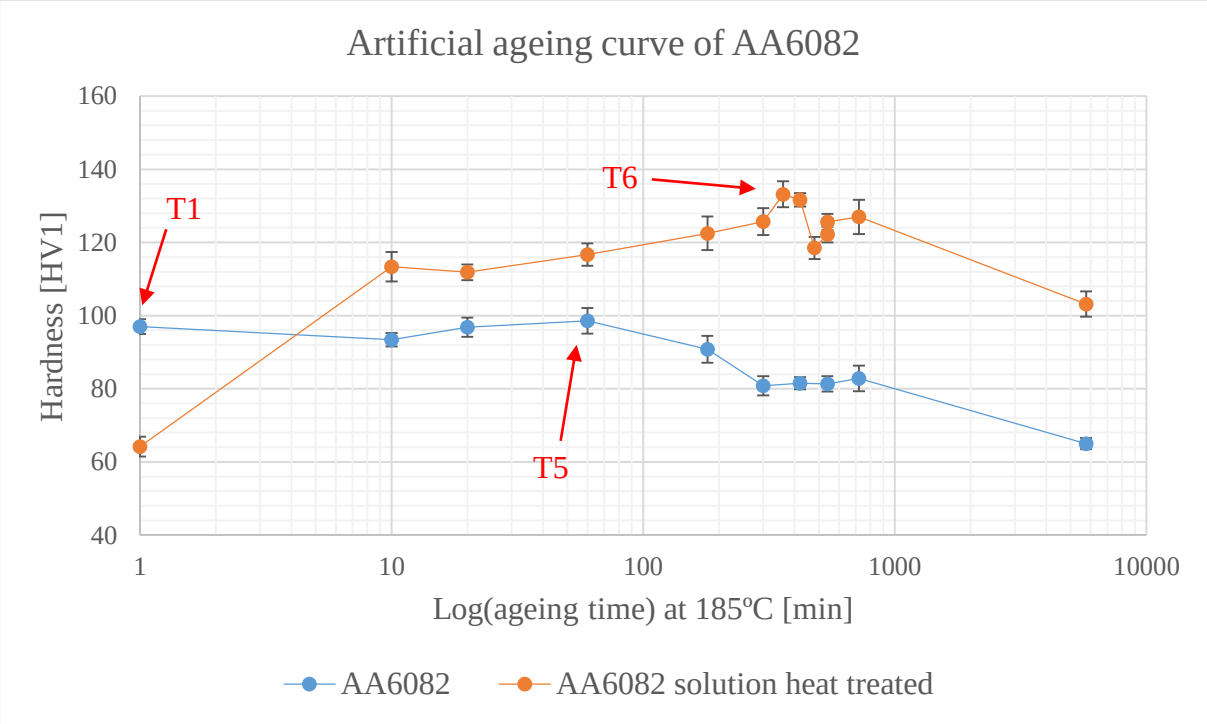

Figure 36: Artificial ageing curves of AA6082. The first point of the blue curve is the hardness of the T1 sample (long storage time) and the first point on the orange curve is the hardness just after heat treatment.

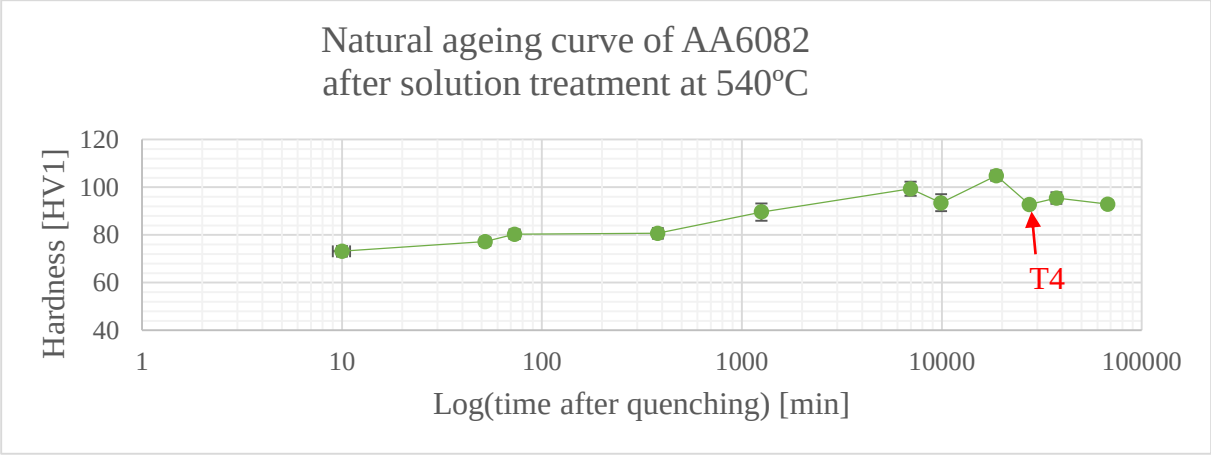

Figure 37: Natural ageing curve of AA6082.

Table 7: The different heat treatment states for AA6082

State	T1	T4	T5	T6
Ageing time	0 minutes	3 weeks	60 minutes	6 hours
Hardness [HV1]	97	92.8	98.6	133.2
Standard deviation	2	1.2	3.5	3.5

The directly artificial ageing of AA7108 was done as a two step ageing process. In the first step, all samples were held in a muffle furnace while it heated from room temperature to 100ºC in 30 minutes, and then held at 100 ºC for 7 hours. The samples were directly moved from the muffle furnace to an oil bath with a temperature of 140ºC, i.e. step two of the artificial ageing process. Samples were taken out at different times and the hardness (HV1) was measured. The samples were air cooled after step two. The samples which were solution heat treated before artificially aged, was solution heat treated at 480ºC for 15 minutes, water quenched, held at room temperature for 10 minutes and then artificially aged the same way as samples directly artificially aged samples. The naturally aged sample was solution heat treated at 480ºC, water quenched and stored. The hardness was measured until it was stable.

The artificial ageing curve of AA7108 is presented in Figure 38, where the temper states T1, T5 and T6 are marked with red arrows. The natural ageing curve of AA7108 is presented in Figure 39, where the T4 temper state is marked with a red arrow. The details of the AA7108 temper states are summed up in Table 8.

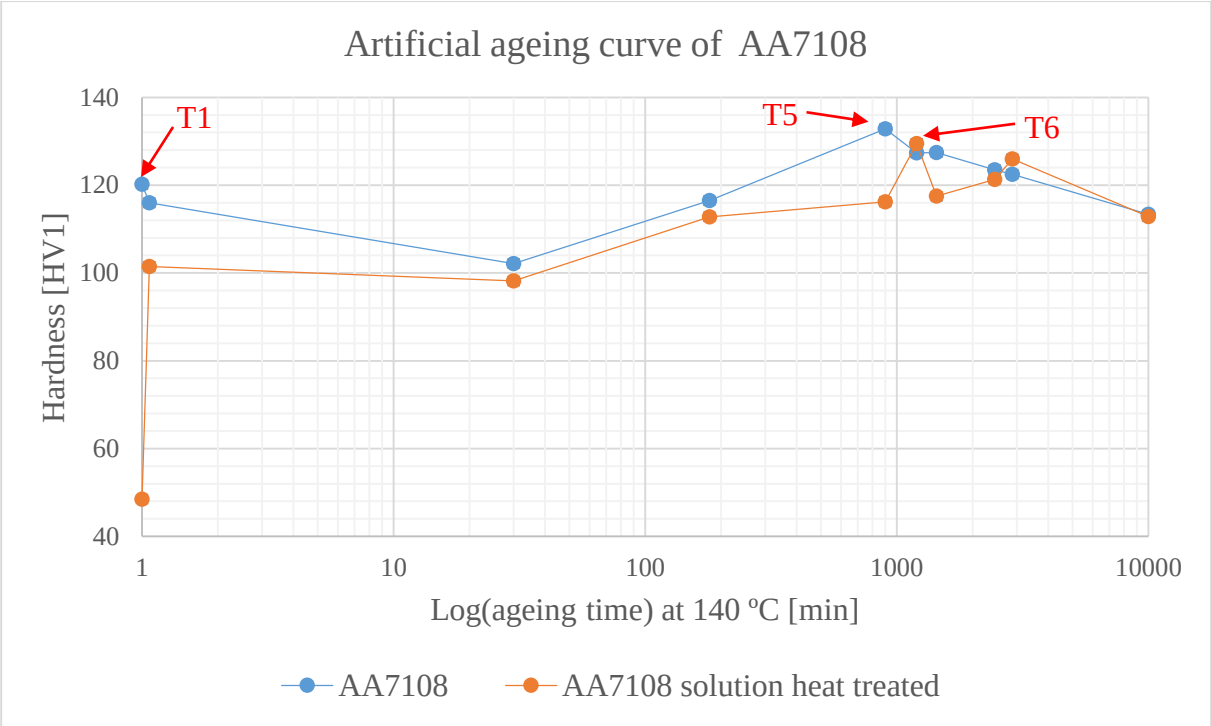

Figure 38: Artificial ageing curves of AA7108. The first point of the blue curve is the hardness of the T1 sample (long storage time) and the first point on the orange curve is the hardness just after heat treatment.

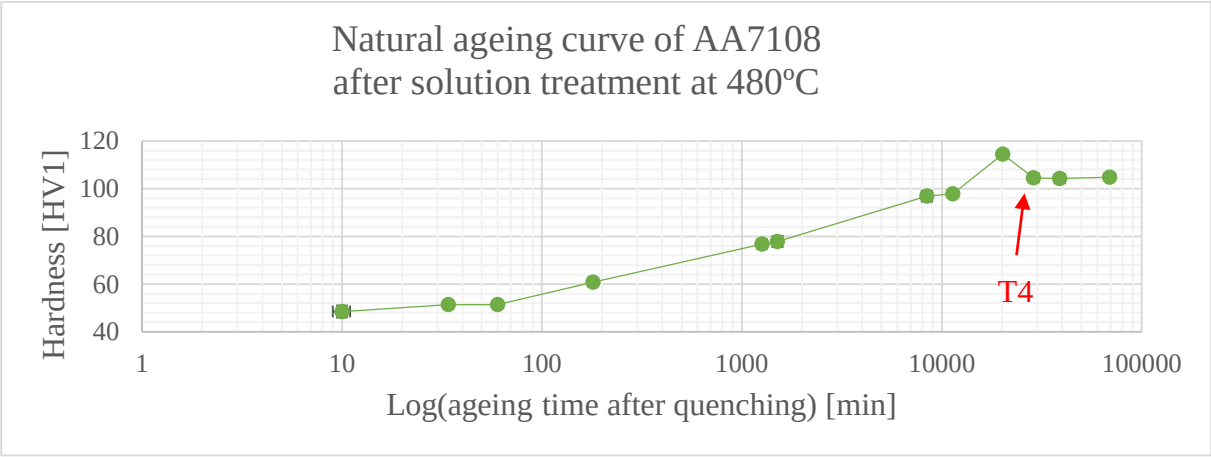

Figure 39: Natural ageing curve of AA7108

Table 8: The different heat treatment states for AA7108

State	T1	T4	T5	T6
Ageing time	0 minutes	3 weeks	15 hours	20 hours
Hardness [HV1]	120.2	104.5	132.8	129.5
Standard deviation	2.3	1.9	3.7	1.8

3.2.2 Light optical micrographs

The light optical micrographs of AA6082 and AA7108 are displayed below. The widths of the recrystallized zones are presented in Table 9 and Table 10. In order to know if there were any recrystallization or grain growth due to heat treatment in the fatigue specimens, these micrographs were needed. The micrographs were taken in the plane normal to TD (the plane parallel to ED) after polishing and anodizing. All samples had a recrystallized layer, and a fibrous microstructure in between.

The recrystallized layer was found on both sides of all AA6082 specimens (3mm thickness), seen in Figure 40 and Figure 41. Note that the T6 has grain growth inside the fibrous microstructure (Figure 41). The size of the recrystallized zones is given in Table 9.

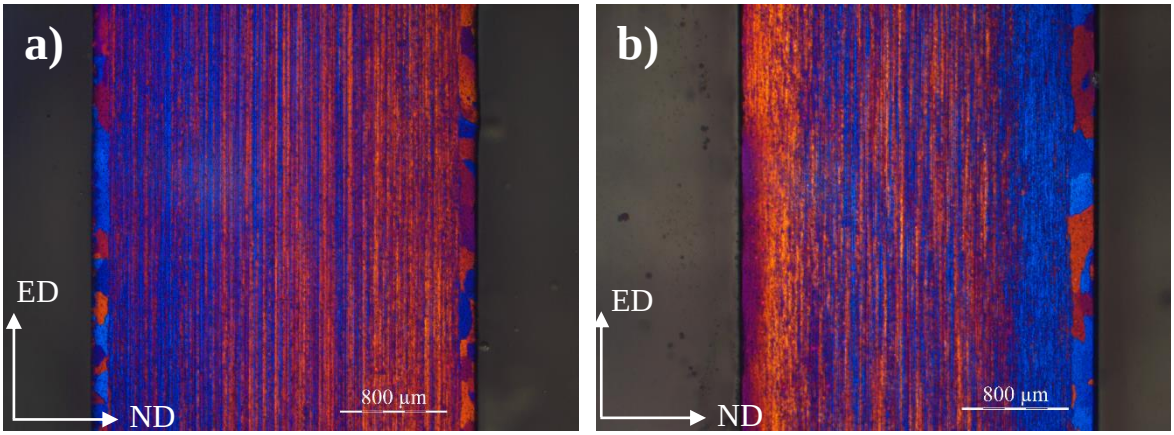

Figure 40: a) AA6082 T1 with a recrystallized layer on both sides. b) AA6082 T5 (the recrystallized layer was also found on the left side of the directly artificially aged sample, even though it is not possible to see).

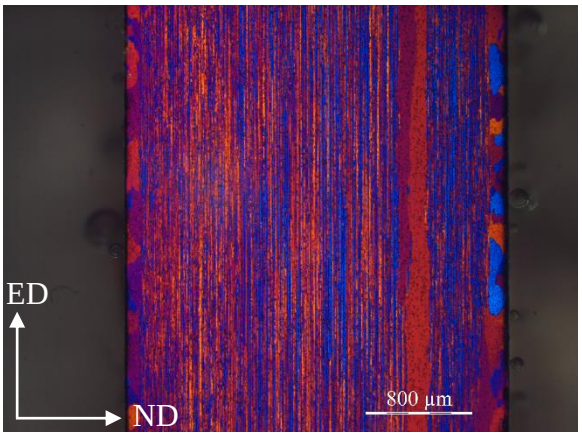

Figure 41: AA6082 T6 with a recrystallized layer on both sides.

Table 9: Width of recrystallized zone in AA6082.

Temper state	T1	T5	T6
Size of recrystallized zone	116-150µm	175-237µm	100-189µm (edge) 181-212µm (in between fibrous structure)

A recrystallized layer was also found on both sides of all AA7108 specimens (10 mm thickness), i.e. Figure 42 and Figure 43. The size of the recrystallized zones is given in Table 10.

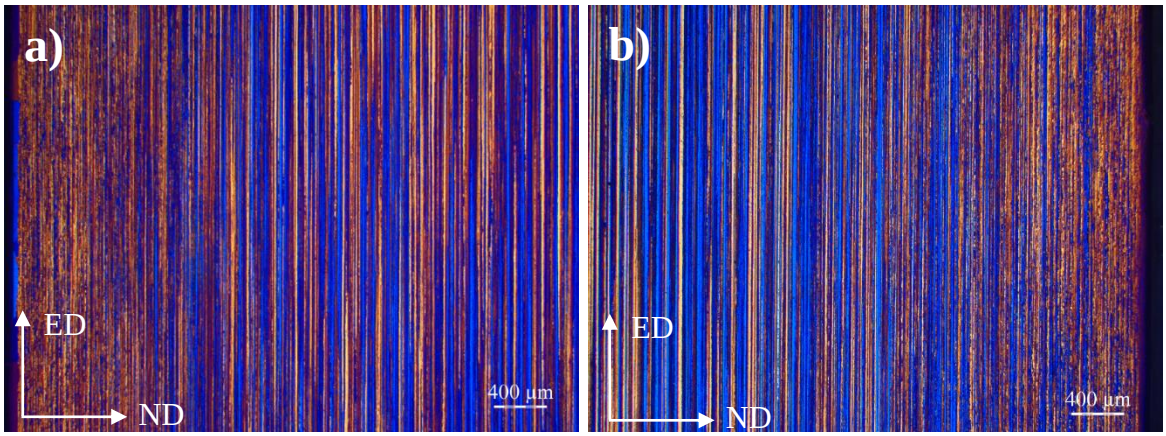

Figure 42: a) AA7108 T1 with a recrystallized layer on the left side, b) AA7108 T5 with a recrystallized layer on the right side.

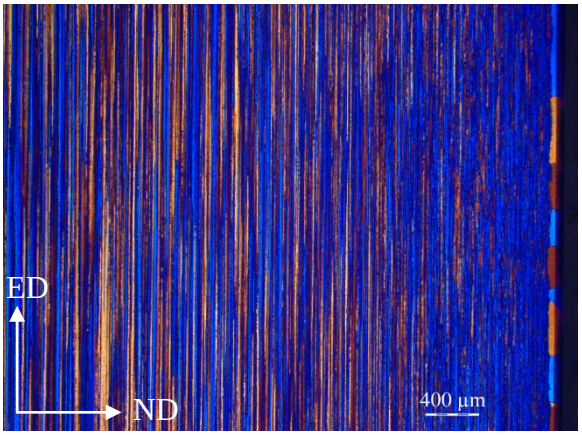

Figure 43: AA7108 T6 with a recrystallized layer on the right side.

Table 10: Width of recrystallized zone in AA7108.

Sample	T1	T5	T6
Size of recrystallized zone	19-72µm	44-63µm	27-56µm (edge)

3.2.3 Tensile properties

In order to do fatigue testing, tensile properties such as yield strength and ultimate tensile strength were needed. These properties are presented in Table 11. The tensile properties were established using the specimens geometry shown in Figure 44, and conducted with MTS810 100kN and a 25 mm extensometer. Tensile specimens were tested in the transverse direction (TD) (as in Figure 47) and in the temper states, T1, T4, T5 and T6.

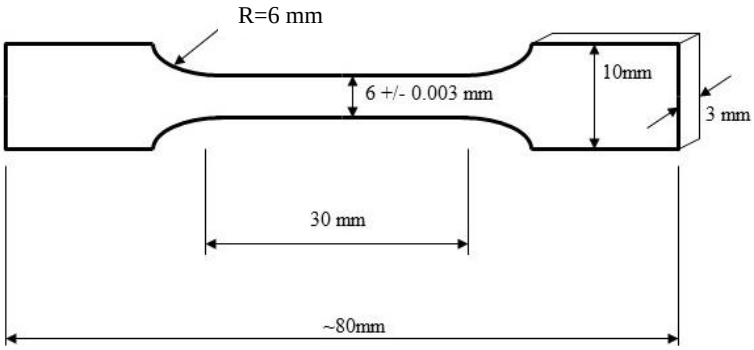

Figure 44: The tensile specimen geometry.

Note the difference in work hardening (the difference between the yield strength and ultimate tensile strength) of the different temper states. The T6 temper state of AA6082 has the highest yield strength and ultimate tensile strength, while the T1 temper state of AA7108 has the highest ultimate tensile strength and the T5 temper state the highest yield strength. The obtained strength of heat treated alloys corresponds to theoretical values [4].

Table 11: Tensile properties of AA6082 and AA7108 as a function of temper state.

Temper state and direction	**Yield strength, σ_y [MPa]**	**Ultimate tensile strength, σ_{UTS} [MPa]**
AA6082		
T1 TD	169	278
T4 TD	240	321
T5 TD	219	292
T6 TD	363	378
AA7108		
T1 TD	293	420
T4 TD	219	350
T5 TD	330	372
T6 TD	319	358

3.3 The experimental procedure

The experimental procedure performed in this thesis will be described in this sub-chapter. Figure 45 illustrates a summary of the entire experimental process.

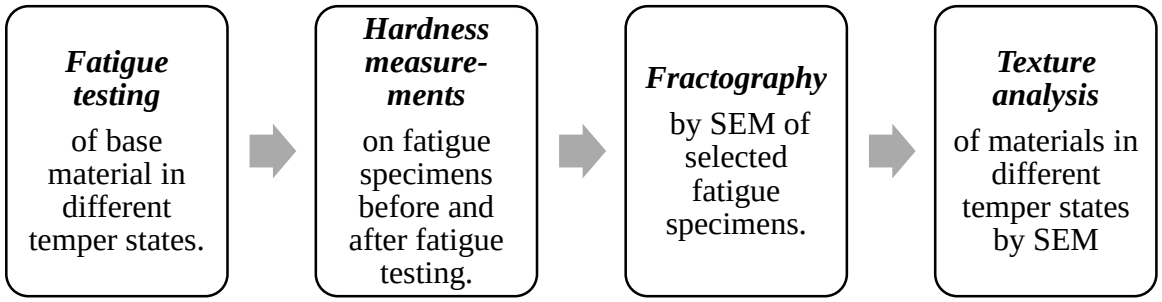

Figure 45: The experimental process.

3.3.1 Heat treatment of fatigue specimens

The fatigue specimens were heat treated to the temper states T4, T5 and T6 which were defined in the proceeding project work and described in chapter 3.2.1.

The T5 fatigue specimens were directly artificially aged, while the T6 and T4 fatigue specimens were solution heat treated before they were artificially or naturally aged. An oil bath was used for the artificial ageing, while the solution heat treatment was done in a salt bath. All AA6082 specimens were water quenched both, after solution heat treatment and after artificially ageing. A summary of the heat treatment performed is shown in Table 12.

Table 12: The details of the heat treatments done on the AA6082 fatigue specimens.

Temper state	T5	T4	T6
Solution heat treatment temperature	-	540 ºC	540 ºC
Solution heat treatment time	-	20 minutes	20 minutes
Ageing temperature	185 ºC	RT	185 ºC
Ageing time	1 hour	3 weeks	6 hours

The AA7108 specimens were artificially aged in a two step ageing process where they first were heated from room temperature to 100 ºC in 30 minutes, and then held at 100 ºC for 7 hours in a muffle furnace. The second step is displayed in Table 13. The AA7108 specimens were water quenched after solution heat treatment and air cooled after artificially ageing.

Table 13 AA7108: The details of the heat treatment for AA7108 fatigue specimens.

Temper state	T5	T4	T6
Solution heat treatment temperature	-	480 ºC	480 ºC
Solution heat treatment time	-	15 minutes	15 minutes
Ageing temperature	140 ºC	RT	140 ºC
Ageing time	15 hours	3 weeks	20 hours

3.3.2 Surface roughness measurements

The surface roughness value (R_a) was measured in between polishing after heat treatment and fatigue testing. It was measured on two arbitrary specimens in all temper states. The measurements were taken with Mitutoyo SJ-301, at the corrosion laboratory at The Department of Engineering Design and Materials. Six measurements were taken on each specimen.

3.3.3 Fatigue testing

The fatigue specimens were made by “Finmekanisk verksted” at NTNU after the drawing in Figure 46. The specimens followed the guidelines given by the American Society for Testing and Materials (ASTM) standard E466 [46].

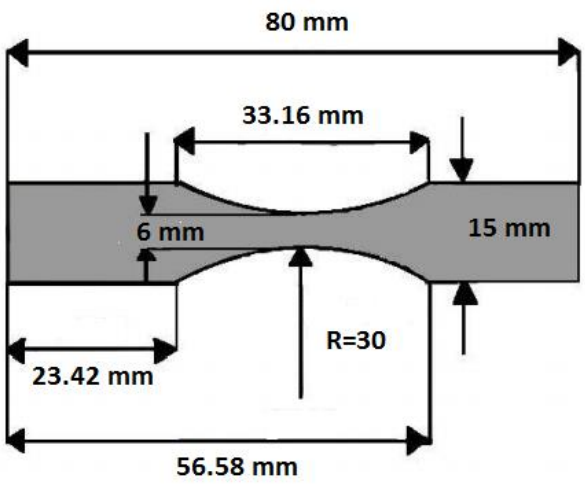

Figure 46: Fatigue specimen geometry (3 mm thickness) in accordance to ASTM E466. The specimens have a rectangular cross section and a continuous radius between the ends.

All fatigue specimens were machined in the transverse direction (TD), i.e. normal to the extrusion direction (ED) as illustrated in Figure 47. Note that the AA7108 specimens were machined from a plate with 10 mm thickness, to 3 mm thickness, and therefore the recrystallization layer is no longer present on these specimens. The thickness of the recrystallized layer was presented in chapter 3.2.2.

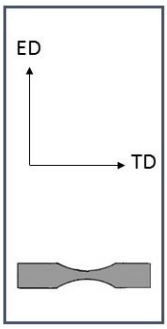

Figure 47: How fatigue specimens where machined out from the extruded profile.

The fatigue testing was done in a MTS810 100kN servo-hydraulic universal test machine. The fatigue specimens were tested in temper states T1, T5, T6 and T4. The AA7108 specimens were all grinded with 1200 SiC paper and the AA6082 specimens were grinded with both 320 and 1200 SiC papers. This was done to decrease the surface roughness and reduce residual stresses from machining. The sharp edges of all fatigue specimens were rounded off by hand with a 1000 SiC paper.

Fatigue testing was carried out as high cycle fatigue with a frequency of 20 Hz and with a stress ratio (R) of 0.1, i.e. a tension-tension-test to avoid buckling. During fatigue testing the axial displacement had a upper limit of 1.8 mm and a lower limit of -0.5 mm (for security reasons).

The aim was to study the fatigue properties of specimens with a fatigue life between 10^5 and 10^6 cycles. The test was manually stopped at $2 \cdot 10^6$, so-called redeemed run outs (RO). To make one SN-curve, 8-10 specimens were tested for each temper state, depending on the appearance of the SN-curve.

In order to make the specimens fail between 10^5 and 10^6 cycles a load bound was established empirically. The first specimen was tested with a maximum stress approximately 20 MPa below the yield strength, where the specimen was anticipated to endure a low number of cycles. The second specimen was tested with maximum stress well below the yield strength (60-100 MPa below), where the specimen was anticipated to endure a high number of cycles. The next 6-8 specimens were tested with maximum stresses in between the maximum stresses used for the first two specimens. The yield strengths used for determining fatigue load parameters were given in chapter 3.2.3.

3.3.4 Hardness measurements

In order to indicate whether cyclic hardening or cyclic softening has occurred during testing, hardness (HV1) was measured with a Matzuzawa DVK-1S before and after testing. The measurements were taken as close to the middle of the specimen as possible, hence inside the red circle showed in Figure 48. Inside this circle it is assumed a one-axial stress state where only the tensile stress will affect the hardness. Six measurements were taken on each specimen. The hardness was measured on two arbitrary specimens before fatigue testing, and then on every fatigue tested specimen. The samples where the hardness measurements were taken before fatigue testing, were slightly grinded before and after hardness measurements with a 1200 SiC paper.

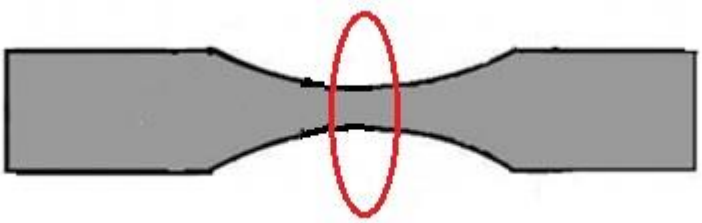

Figure 48: Area where hardness measurements were taken on fatigue specimens.

3.3.5 Construction of Goodman diagrams

The Goodman diagrams were constructed in Excel by the derived equations for straight lines below. The approach described below was lectured in TMT4222 at NTNU during the fall of 2013 [25]. Equation 20, is the equation for the line representing the variation of maximum stress by mean stress, while Equation 22 is the equation for the line representing the variation of minimum stress by mean stress. Both equations are constructed on the base of the equation of a straight line, $y = ax+b$, where a is the slope and b is the interception point of the line and the y-axis.

$$\sigma_{max}^{R=0.1}(\sigma_m) = a\sigma_m^{R=0.1} + b \tag{20}$$

$$a = \frac{\sigma_{UTS} - \sigma_{max}^{R=0.1}}{\sigma_{UTS} - \sigma_m^{R=0.1}} \tag{21}$$

$$\sigma_{min}^{R=0.1}(\sigma_m) = a\sigma_m^{R=0.1} + b \tag{22}$$

$$a = \frac{\sigma_{UTS} - \sigma_{min}^{R=0.1}}{\sigma_{UTS} - \sigma_m^{R=0.1}} \tag{23}$$

The equations were derived by using known points of each line, hence the points representing fatigue testing at R=0.1. Ultimate tensile strength and yield strength were taken from the tensile testing results (chapter 3.2.3), while the maximum, minimum and mean stress were taken from the fatigue test data (Appendix A – Fatigue test data).

First the ultimate tensile strength and the yield strength were marked on both axis and as $(\sigma_{UTS}, \sigma_{UTS})$ and (σ_y, σ_y), and lines were drawn between the points. Then the points $(\sigma_{max}^{R=0.1}, \sigma_m^{R=0.1})$ and $(\sigma_{min}^{R=0.1}, \sigma_m^{R=0.1})$, where marked on the diagram, this is illustrated with Figure 49.

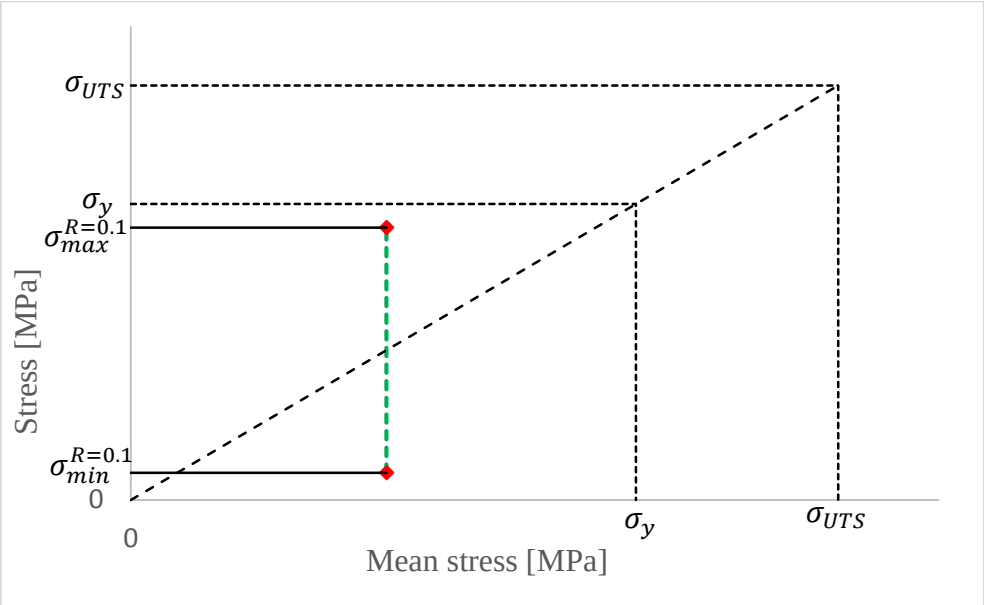

Figure 49: Construction of a Goodman diagram when R=0.1, part 1.

A straight line was then drawn from the ultimate tensile strength to each of the points, $(\sigma_{max}^{R=0.1}, \sigma_m^{R=0.1})$ and $(\sigma_{min}^{R=0.1}, \sigma_m^{R=0.1})$, as seen in Figure 50.

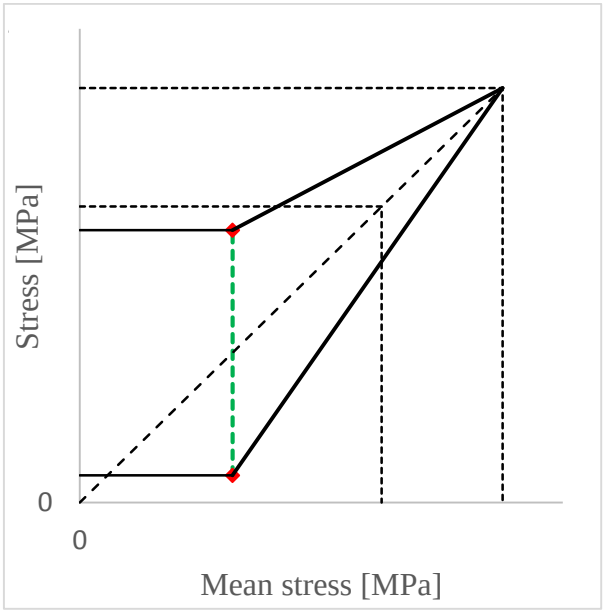

Figure 50: Construction of a Goodman diagram when R=0.1, part 2.

The stress range at R=-1 and R=0 can then be found in two ways, graphical and mathematical. To derive the stress range at R=-1 graphically, the lines were elongated until they crossed the y-axis, and the intersection points were read. To derive the stress range at R=0 graphically,

the lower line was elongated until it crossed the x-axis, and the intersection point was red. An illustration can be seen in Figure 51.

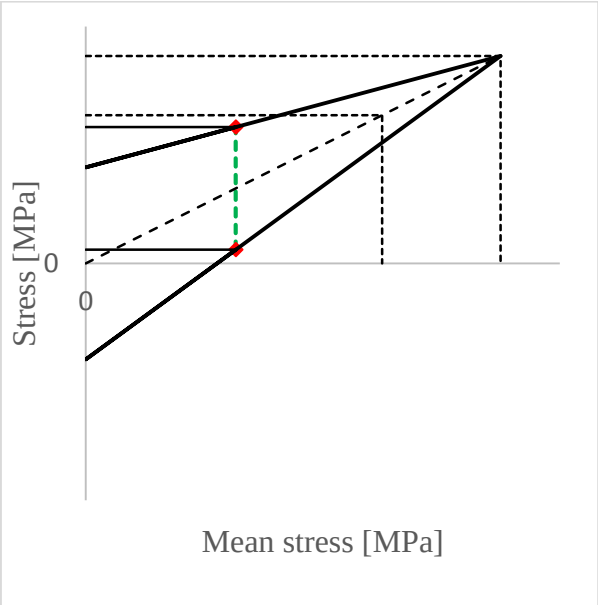

Figure 51: Construction of a Goodman diagram when R=0.1, part 3.

To derive the stress range at R=-1 mathematically Equations 20 and 22 was solved for *b*. To derive the stress range at R=0 mathematically, Equation 22 was solved for *x* when *y=0* with the *b* found for R=-1. The slope, *a*, was calculated according to Equations 21 and 23.

3.3.6 Scanning electron microscopy (SEM) analysis

To underline the fatigue properties, SEM was used to do fractography investigations, EDS-, grain structure- and crystallographic texture analysis. Fractography analysis was performed with the FESEM Zeiss Ultra 55 Limited Edition, and the EDS and EBSD analysis with the LVFESEM Zeiss Supra 55 VP, both at the EM-laboratory, at the Department of Materials Science and Engineering.

Fractography

For every temper state, the fractured surface with the shortest and longest fatigue life (before RO) was investigated with SEM. The fractured surfaces of the most deviating specimens (if any) were also investigated. Secondary electrons were used, the acceleration voltage was 20 kV and the aperture was 30µm. The working distance was optimized for each specimen to get the most advantages depth of field, and therefore it was not the same for all specimens. To remove any organic material, all specimens were held in an ultrasound bath for 2 minutes before inserted in the SEM.

The fractographs of each investigated specimen was taken with the following approach,

1. An overview of the fractured surface was taken with a magnification of 15X. The fatigue fractured area, and the final fracture are were decided.
2. Possible fracture initiation points were investigated with both 2000X and 7000X magnifications. To find possible initiation points, the edges around the fatigue fractured area was investigated. The initiation point and stage I crack growth is at the same site, but as stage I crack growth is feature less other signs of an initiation point were search for, as surface imperfections (grooves or notches and oxidation products).
3. The area of crack propagation (stage II crack growth) was investigated with 500X and 2000X magnification. In this area, features like transgranular growth, striations and slip localized growth were recognized.
4. The final fracture was investigated with a magnification of 500X. All final fractures were expected to be ductile and therefore dimples and shearing were searched for.

Energy dispersive X-ray spectroscopy (EDS)

After a suspicion of corrosion, EDS analysis was performed on one fatigue specimen that deviated from the others. The working distance was approximately 13 mm, the acceleration voltage was 20 kV and the aperture was 120μm. The specimen was held in an ultrasound bath for 2 minutes before inserted in the SEM to remove any organic material.

Electron backscatter analysis (EBSD)

The grain structure and crystallographic texture analysis were done by using EBSD. For both alloys, the analysis was carried out in the plane normal to ED, i.e. the red shaded area on Figure 52.

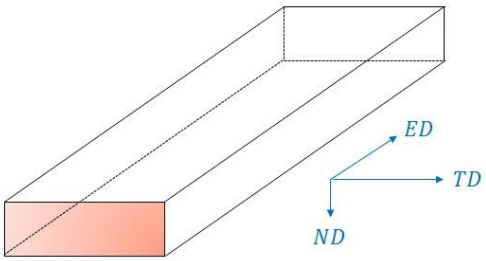

Figure 52: The plane where texture analysis was performed.

Before analysis, the samples were immerged in Epofix Cold-setting Resin and grinded with Struers RotoPol-31 (SiC papers 1-3 in Table 14) before polishing with Struers TergaPol-31 (polishing paper 4-6 in Table 14). At last the samples were electro polished by StruersLectropol-5 in a Struers A2 electrolyte at -30ºC, with a voltage of 20V for 20 seconds.

Table 14: The 6-step grinding and polishing sequence.

1	2	3	4	5	6
800 SiC	1200 SiC	2000 SiC	6µm	3µm	1µm

The texture was investigated on as delivered material (T1) and on both solid solution heat treated and artificially aged material (T6). All specimens were tilted 70º, the acceleration voltage was 20 kV, the aperture was 300µm and the working distance approximately 25mm. Texture analysis was executed by scanning two areas of the sample, each of 0.6mm x 1.5 mm, see Figure 53. A step size of 3µm was chosen to make the scans.

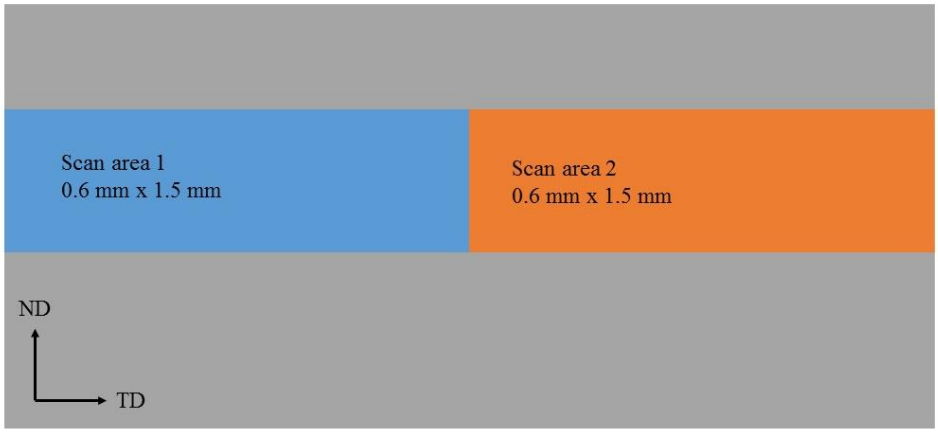

Figure 53: An illustration of where the scans were taken (the blue and orange areas). The grey area illustrates the entire sample surface in the TD-ND plane.

The raw texture data was collected by an EDAX's OIM Data Collection Software, and analyzed by the EDAX's OIM Data Analysis program. Here the two scans were put together to make an orientation grain map over an area of 0.6 mm x 3 mm of the TD-ND-plane. Pole figures were made from the orientation maps, and the pole figures therefore represents the texture of the whole scanned area. Note that 3 mm is the entire width of the samples.

4 Results

In this chapter, the results will be presented in the following order, surface roughness measurements, SN-curves, Goodman Diagram, Hardness measurements, fractography and at last crystallographic texture.

4.1 Surface roughness measurements

The surface roughness values (R_a) of the fatigue specimens after polishing, but before fatigue testing are presented in Table 15 (AA6082) and Table 16 (AA7108). The surfaces have relative low roughness values (R_a<0.5µm), and hence the surfaces are smooth.

Table 15: Ra measurements of AA6082 fatigue specimens.

Temper state	**R_a average [µm]**	**Standard deviation**
T1	0.37	0.07
T5	0.27	0.03
T4	0.38	0.04
T6	0.26	0.05

Table 16: Ra measurements of AA7108 fatigue specimens.

Temper state	**R_a average [µm]**	**Standard deviation**
T1	0.25	0.03
T5	0.26	0.03
T4	0.41	0.06
T6	0.27	0.06

4.2 Fatigue testing

The fatigue tests resulted in SN-curves. The SN-curve of each temper state and alloy is a logarithmic trend line of the points plotted as maximum stress versus number of cycles to failure. The room temperature during each fatigue test was stable and varied by ±1 degree. As stated above, the aim was to investigate the fatigue properties between 10^5 and 10^6 cycles and therefore, if the specimen had not fractured, all fatigue tests were stopped at $2 \cdot 10^6$ cycles, so called redeemed run outs (RO). The RO's are marked with arrows in the same color as the corresponding SN-curve. The yield strengths of each temper state are also included as horizontal lines with colors corresponding to the color of the SN-curve of that temper state. The SN-curve of each temper state will also be presented in the chapter regarding fractography.

4.2.1 SN-curves of AA6082

The SN-curves of AA6082 in different temper states are displayed in Figure 54. As can be seen, the T4 temper (green curve) has the highest fatigue strength at $5 \cdot 10^5$ cycles, while the T6 temper (black curve) has the lowest. Also at $5 \cdot 10^5$ cycles, note how close the T1 temper state (red curve) is to its yield strength, in comparison to the other temper states. Some important features of the SN-curves are summed up in Table 17. All fatigue test data can be found in Appendix A – Fatigue test data.

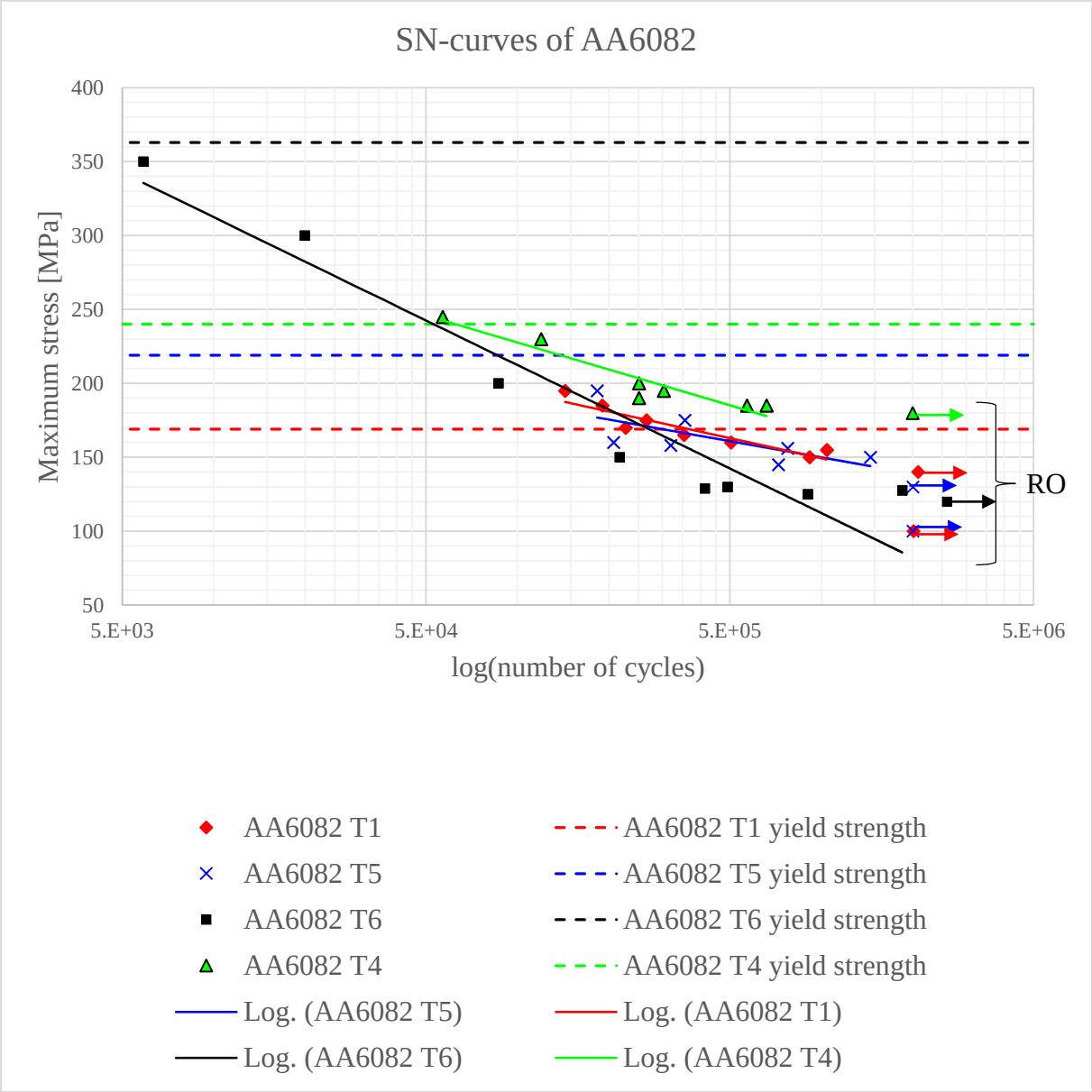

Figure 54: SN-curves of AA6082 (the RO's are not included in the logarithmic trend lines).

Table 17: Important features of the AA6082 SN-curves.

Temper state	**Fatigue strength at $5 \cdot 10^5$ cycles [MPa]**	**Maximum stress at RO [MPa]**	**Yield strength [MPa]**
T1	162	140	169
T4	185	180	240
T5	161	130	219
T6	140	120	363

4.2.2 SN-curves of AA7108

The SN-curves of AA7108 in different temper states are displayed in Figure 55. As can be seen from the figure, the T5 temper state (blue curve) has the highest fatigue strength at $5 \cdot 10^5$ cycles, while the T4 temper state (green curve) has RO closest to its yield strength. Note that only T4 endures a large number of cycles above the yield strength, and that the slope of the T1 curve (red) is the least steep. Some important features of the SN-curves are summed up in Table 18. All fatigue test data can be found in Appendix A – Fatigue test data.

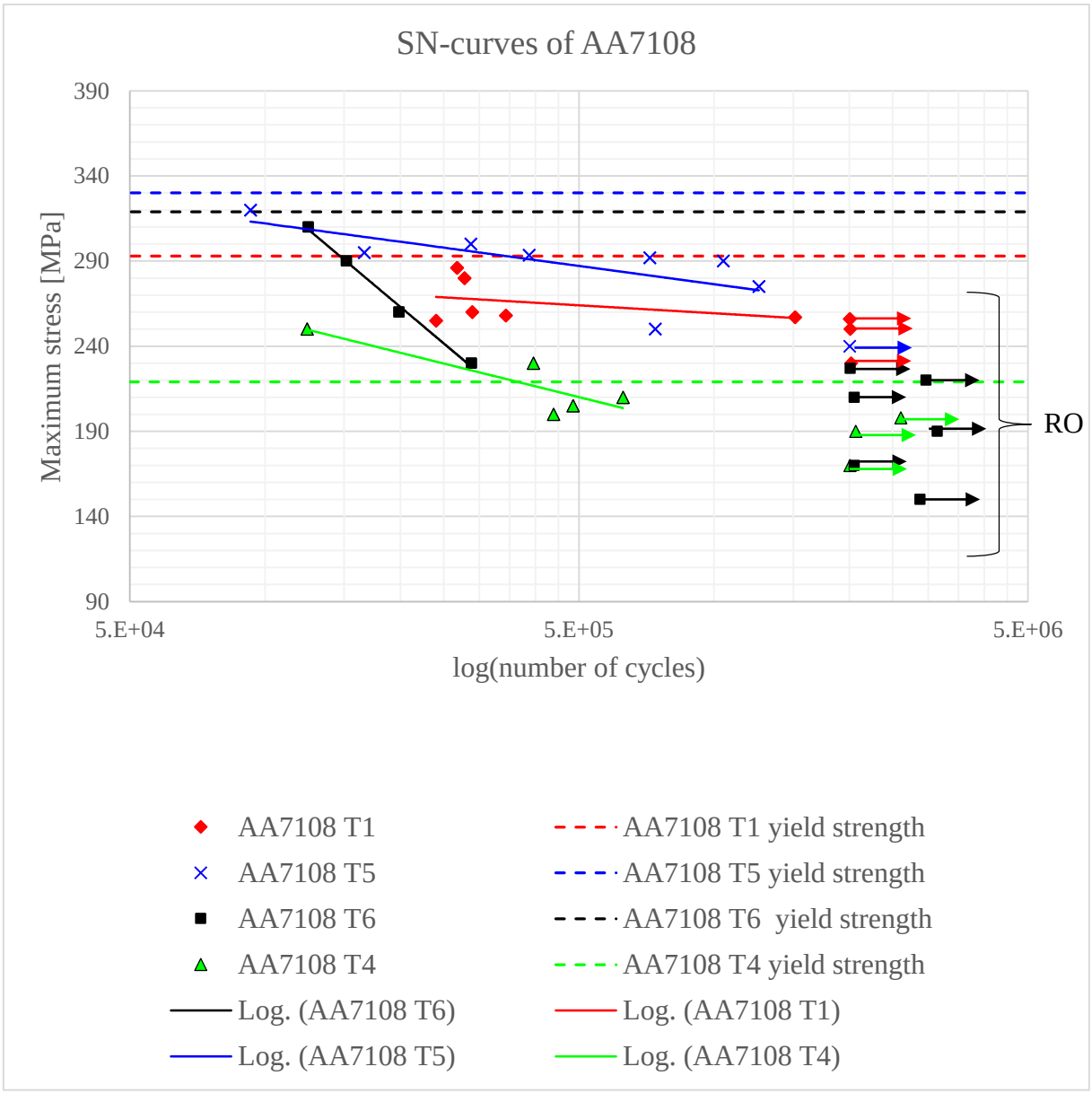

Figure 55: SN-curves of AA7108 (the RO's are not included in the logarithmic trend lines). Note that one of T1's RO is at the same point as another and therefore not visible.

Table 18: Important features of the AA7108 SN-curves.

Temper state	**Fatigue strength at $5 \cdot 10^5$ cycles [MPa]**	**Maximum stress at RO [MPa]**	**Yield strength [MPa]**
T1	265	256	293
T4	210	198	219
T5	288	240	330
T6	175*	220	319

* By elongating the SN-curve.

4.3 Goodman diagrams

To illustrate the effect of mean stress, Goodman diagrams were constructed. All Goodman diagrams will be displayed as the one in Figure 56, but with less information due to better readability. Please use Figure 56, if some lines are unclear on the following Goodman diagrams.

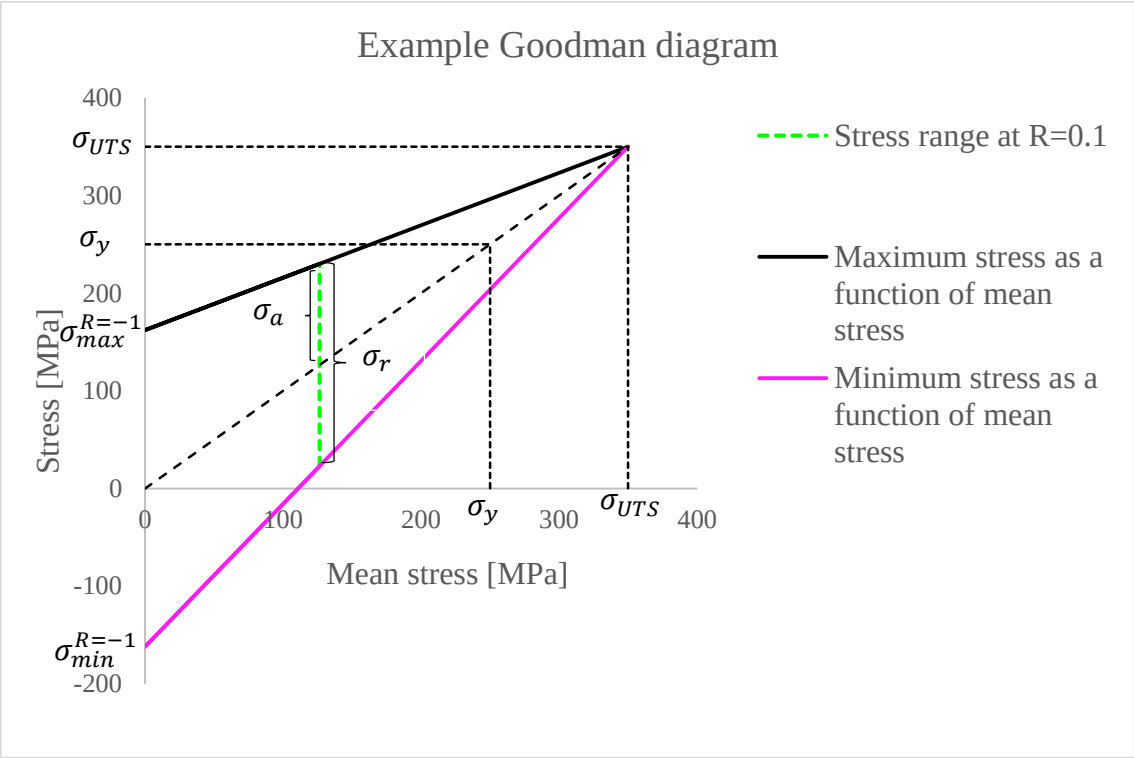

Figure 56: An example Goodman diagram, where σ_R is the stress range, σ_A is the stress amplitude, σ_{UTS} is the ultimate tensile strength and σ_y is the yield strength.

On the following Goodman diagrams, the stress range at R=0 and R= -1 will also be marked. Note that every Goodman diagram is made for one fixed number of cycles, the RO. If a temper state have several RO's, the RO at the largest maximum stress was chosen. As can be seen on all Goodman diagrams, the stress range increases as the mean stress decreases, hence as the stress ratio (R) decreases. The increase in stress range happens on the expense of a decrease in maximum stress. The Goodman diagrams also illustrates the difference between ultimate tensile strength and yield strength (the amount of work hardening).

4.3.1 Goodman diagrams of AA6082

The Goodman diagram for AA8082 T1 at RO is displayed in Figure 57. The maximum stress where fatigue is avoided is the lowest of the AA6082 temper states, but the stress range is the second larges at any given mean stress. Note the large amount of work hardening, the largest of the AA6082 temper states.

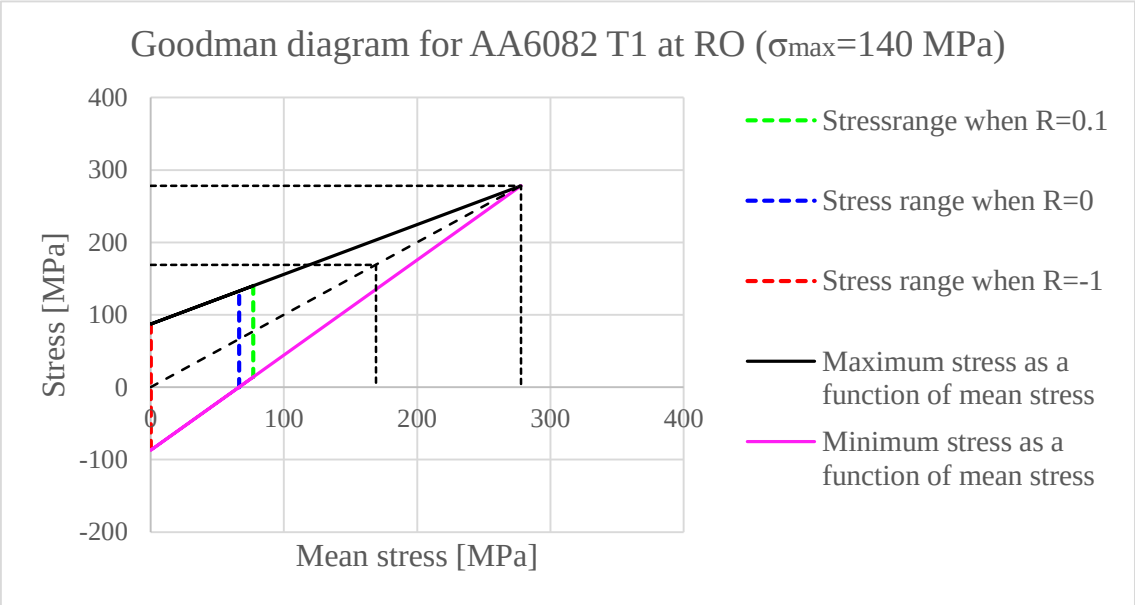

Figure 57: Goodman diagram for AA6082 T1 at RO.

Figure 58 is the Goodman diagram for AA6082 T4. This temper state has the largest stress range of the AA6082 temper states at any given mean stress. In the range where fatigue is avoided, the stress range is larger than for the other temper states.

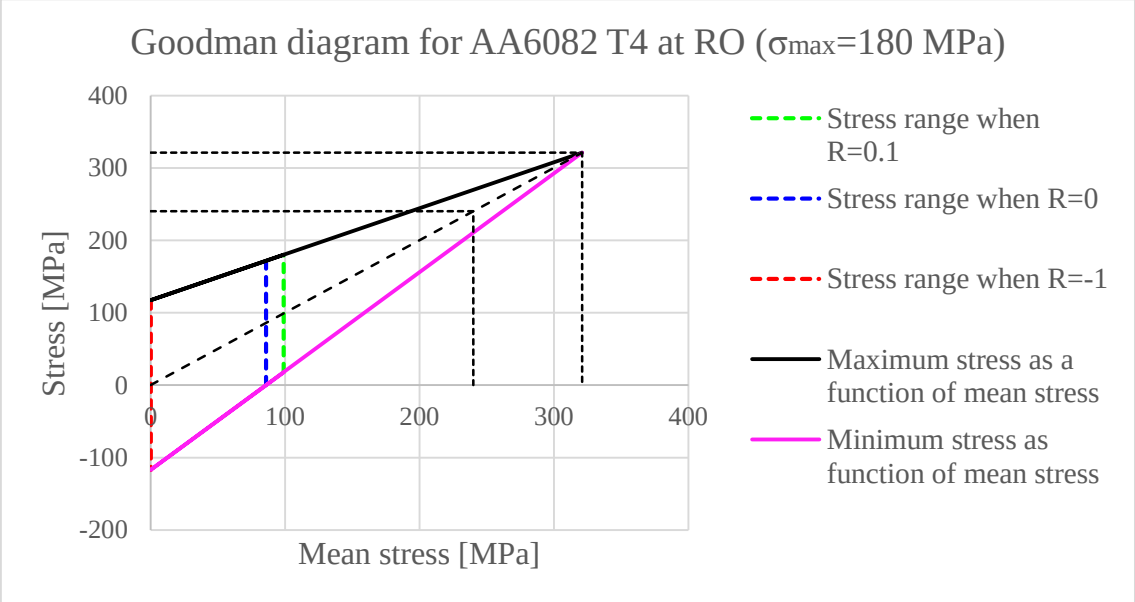

Figure 58: Goodman diagram for AA6082 T4 at RO.

Figure 59 displays the Goodman diagram for AA6082 T5 at RO. Fatigue can be avoided at higher maximum stresses than for T1, but the stress range is more narrow for any given mean stress.

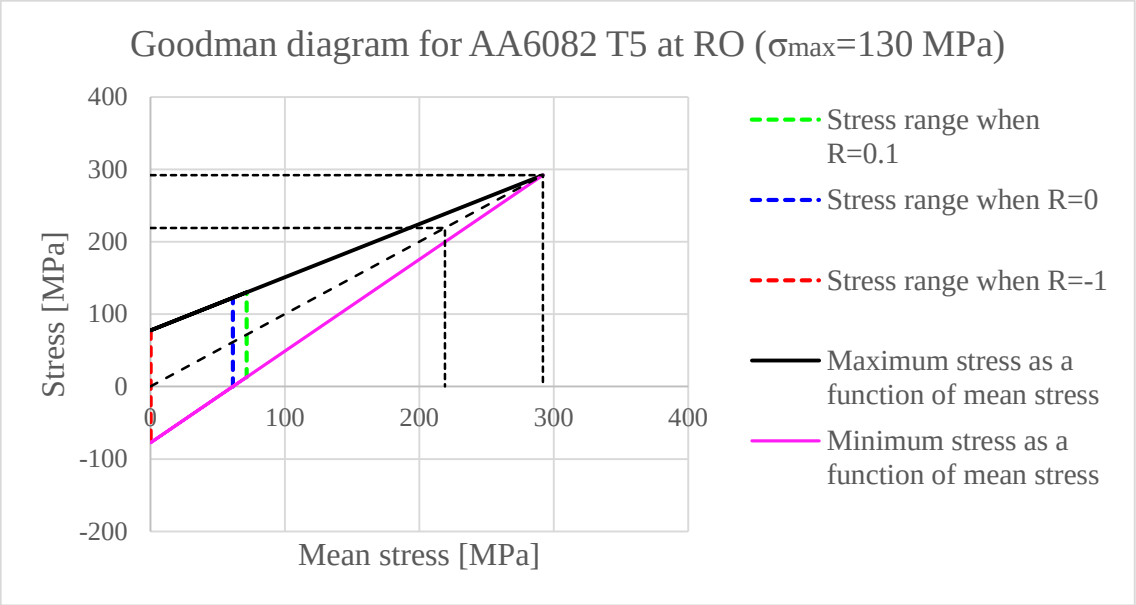

Figure 59: Goodman diagram for AA6082 T5 at RO.

Figure 60 is the Goodman diagram for AA6082 T6. Fatigue can be avoided at high maximum stresses, but then at narrow stress ranges. In comparison of the other AA6082 temper states, this temper state has the most narrow stress range at any given mean stress. Note the small difference between the yield strength and the ultimate tensile strength.

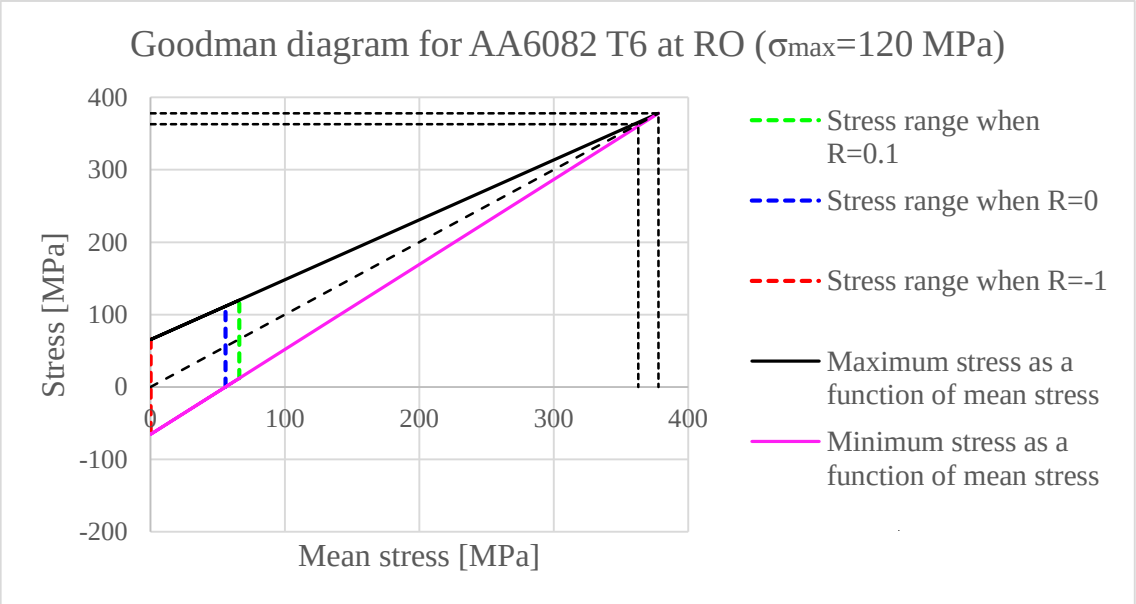

Figure 60: Goodman diagram for AA6082 T6 at RO.

4.3.2 Goodman diagrams of AA7108

The Goodman diagram of AA7108 T1 at RO is displayed in Figure 61. This temper state has the largest stress range at any given mean stress, in addition to the largest maximum stress where fatigue can be avoided. The amount of work hardening is the second largest.

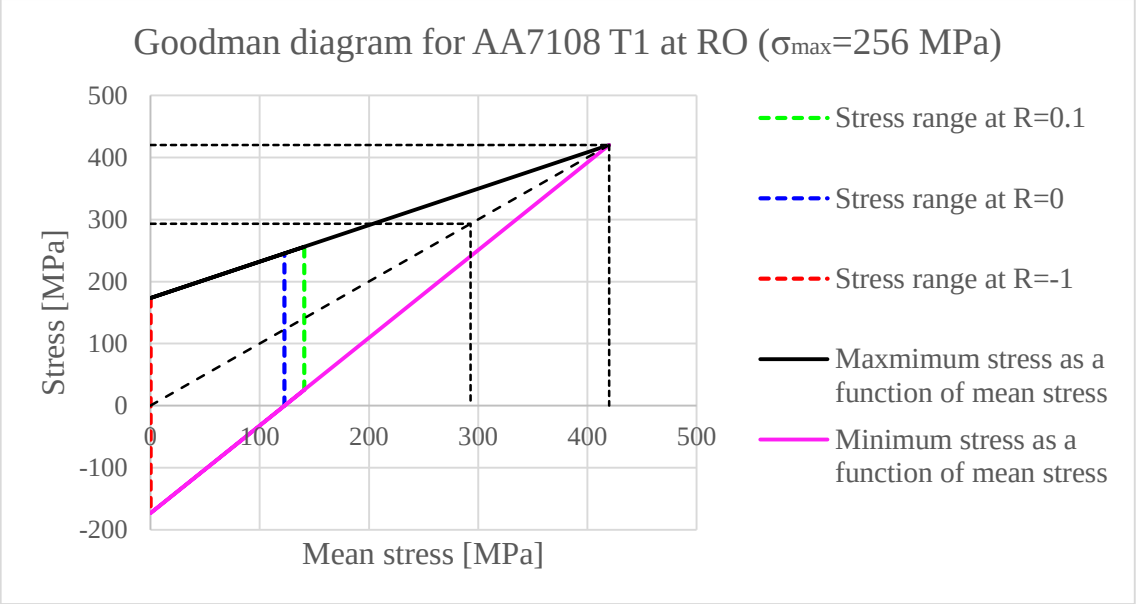

Figure 61: Goodman diagram for AA7108 T1 at RO.

The Goodman diagram of AA7108 T4 is displayed in Figure 62. This temper state has the largest amount of work hardening, but only the third largest stress range at any given mean stress.

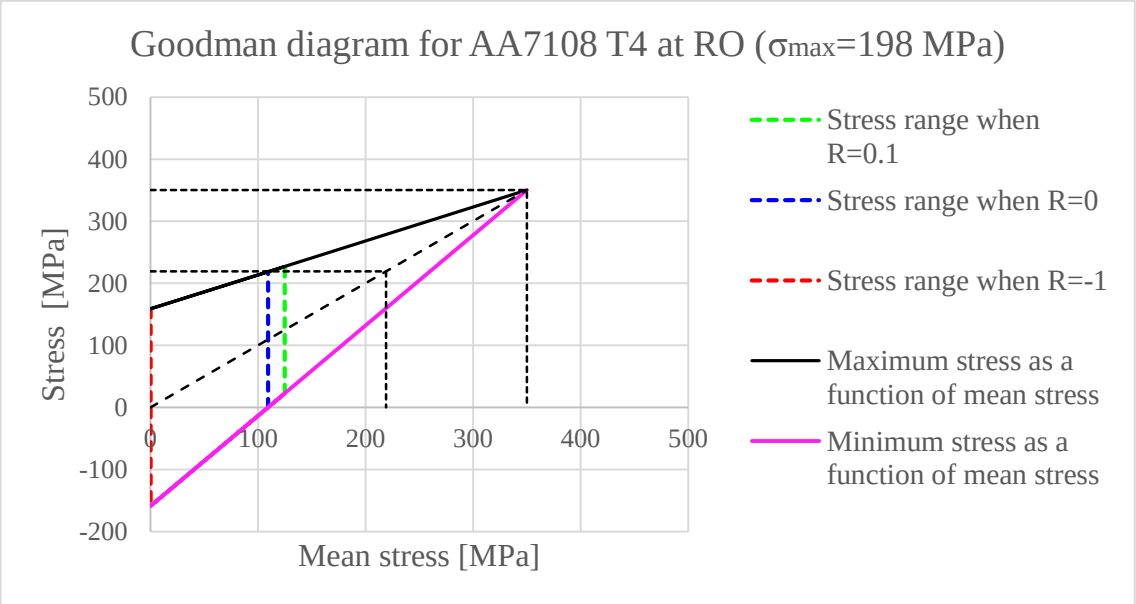

Figure 62: Goodman diagram for AA7108 T4 at RO.

Figure 63 displays the Goodman diagram for AA7108 T5 at RO. The stress range at any given mean stress is the second largest of the AA7108 temper states.

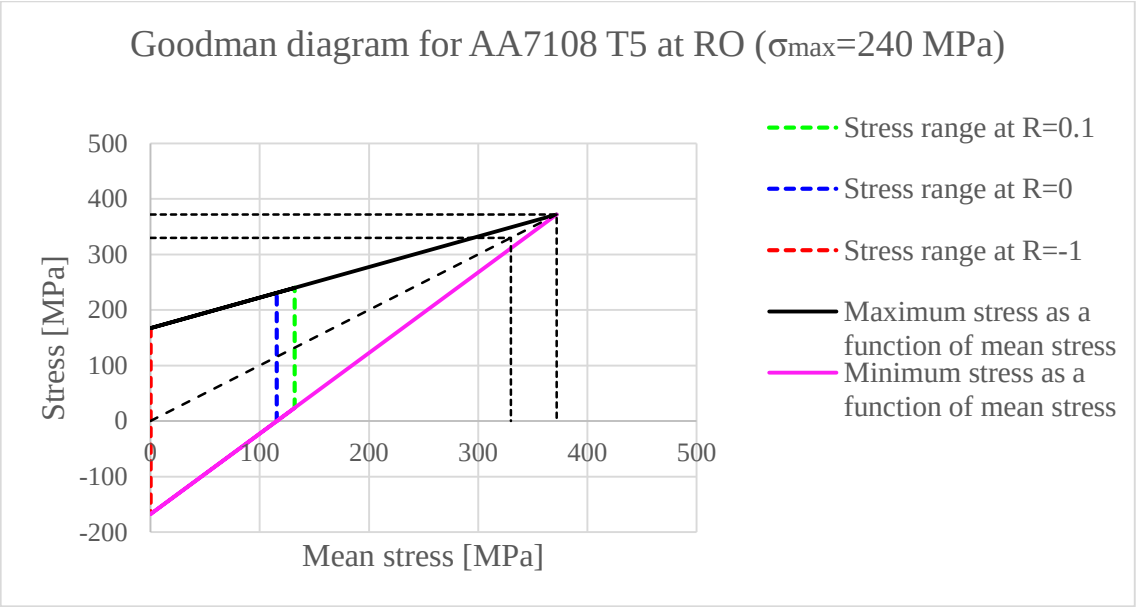

Figure 63: Goodman diagram for AA7108 T5 at RO.

The stress range of AA7108 T6 at any given mean stress is the most narrow of the AA7108 temper states, as can be seen in Figure 64.

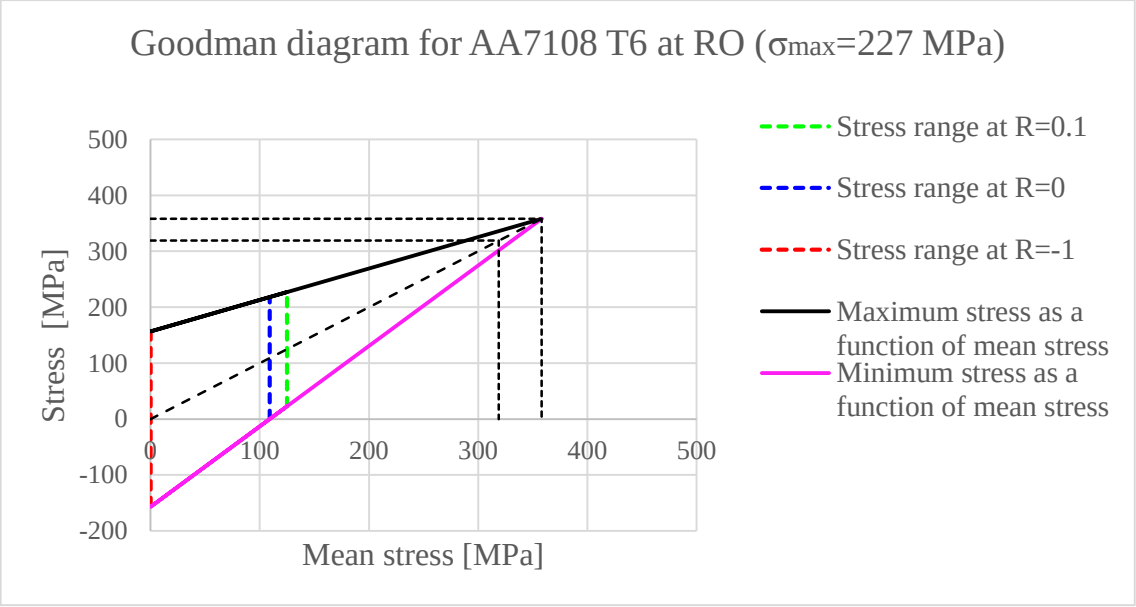

Figure 64: Goodman diagram for AA7108 T6 at RO.

4.4 Hardness measurements

The hardness (HV1) was measured on each specimen after fatigue testing, and on two arbitrary specimens of each alloy and temper state before fatigue testing. This was done to investigate whether cyclic softening or cyclic hardening had occurred during testing. In the following, the hardness evolvement will be presented in figures where the hardness before fatigue testing is illustrated as two red lines (each line representing one specimen), and the hardness after fatigue testing as black dots (each dot representing one specimen). The hardness evolvement is illustrated as hardness versus maximum stress. All hardness values before and after fatigue testing with standard deviation can be found in Appendix B – Hardness of fatigue specimens.

4.4.1 Hardness of AA6082

The hardness of the T1 specimens before fatigue testing compared to the hardness after fatigue testing is illustrated in Figure 65. Most of the hardness values after fatigue testing is above the red lines indicating that cyclic hardening has occurred. Contrary, softening occurs for the lower peak stresses. From this figure, it is also possible to see that the increase in hardness happens as the maximum stress increases.

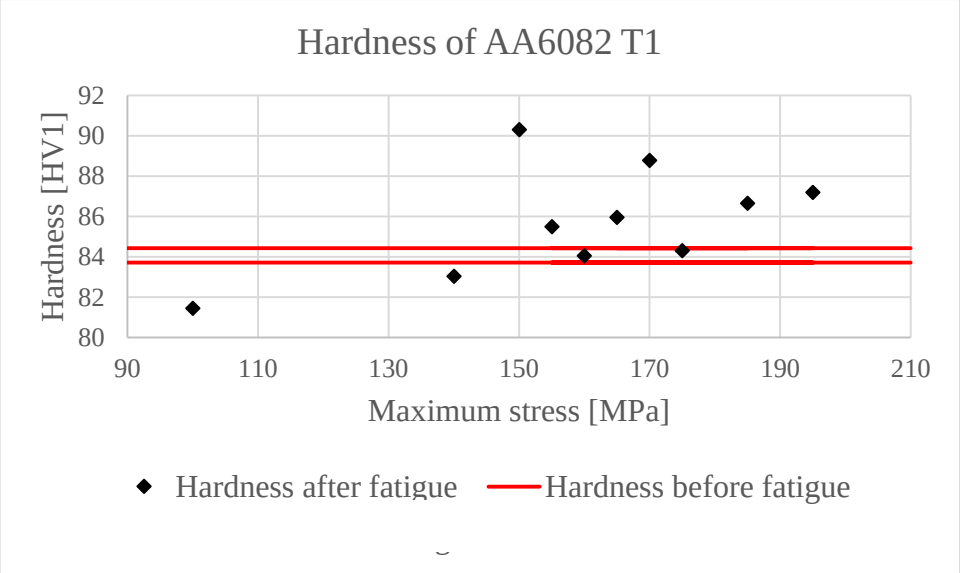

Figure 65: T1 specimens, the hardness before fatigue testing compared to the hardness after.

The hardness of the T4 specimens before fatigue testing compared to the hardness after fatigue testing is illustrated in Figure 66. At stress values close to and above the yield strength, the hardness is higher after fatigue and hence cyclic hardening has occurred. At the other stress values it is difficult to decide whether cyclic hardening has occurred or if the hardness is unaffected by fatigue.

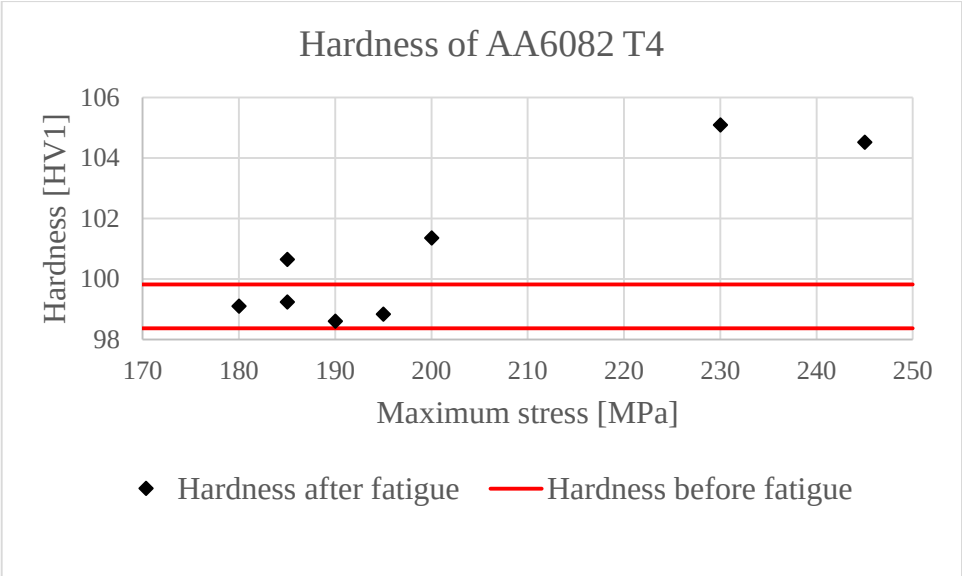

Figure 66: T4 specimens, the hardness before fatigue testing compared to the hardness after

The hardness of the T5 specimens before fatigue testing compared to the hardness after fatigue testing is illustrated in Figure 67. A large amount of the hardness values after fatigue testing is below the red lines indicating that cyclic softening has occurred. In this figure, it is possible to see that the hardness is decreasing as the maximum stress is increasing.

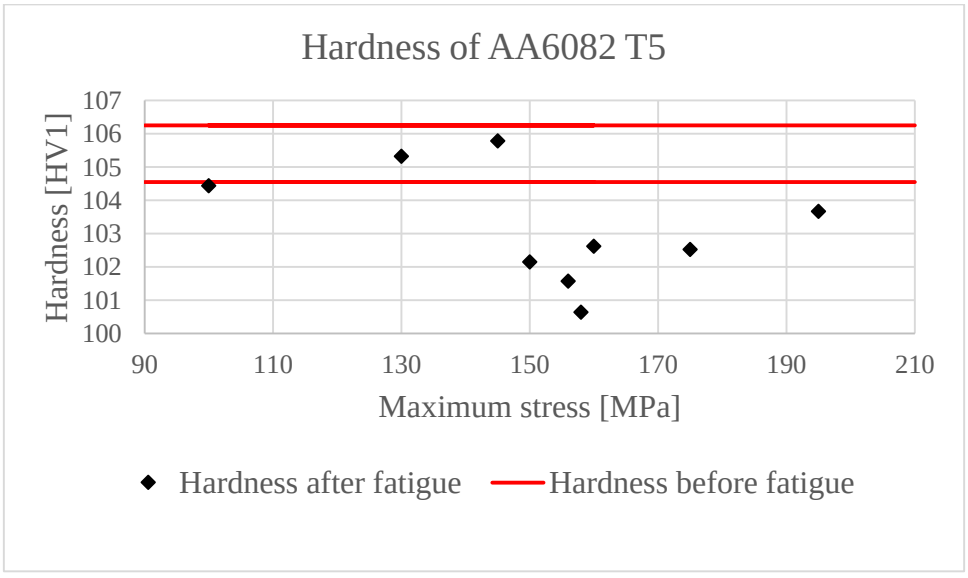

Figure 67: T5 specimens, the hardness before fatigue testing compared to the hardness after.

The hardness of the T6 specimens before fatigue testing compared to the hardness after fatigue testing is illustrated in Figure 68. As for T5, most of the T6 hardness values after fatigue testing is below the red lines indicating that cyclic softening has occurred. This figure does not indicate a relationship between the hardness and the maximum stress.

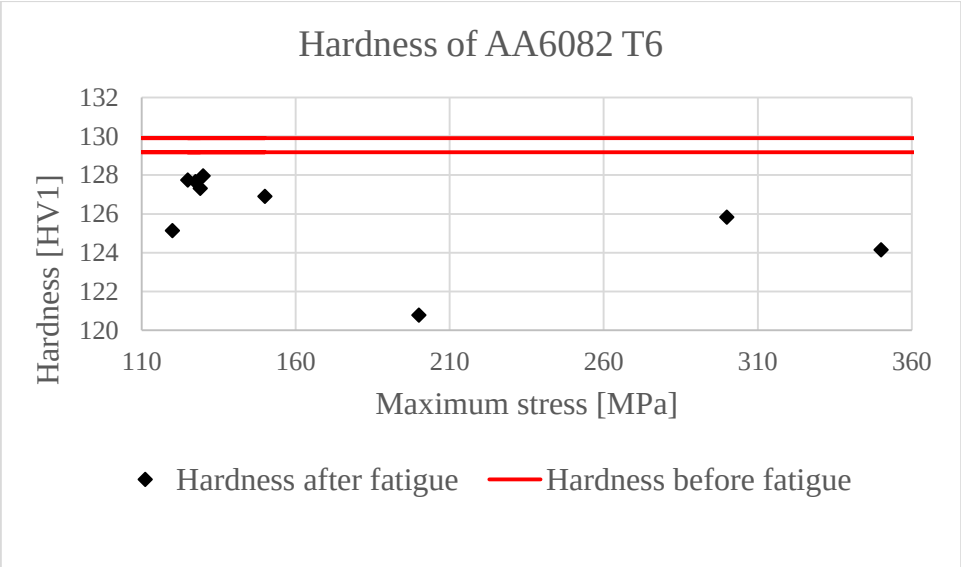

Figure 68: T6 specimens, the hardness before fatigue testing compared to the hardness after.

4.4.2 Hardness of AA7108

The hardness of the T1 specimens before fatigue testing compared to the hardness after fatigue testing is illustrated in Figure 69. It seems as cyclic softening has occurred as most of the hardness values after fatigue testing are below the red lines. This figure does not indicate a relationship between the hardness and the maximum stress.

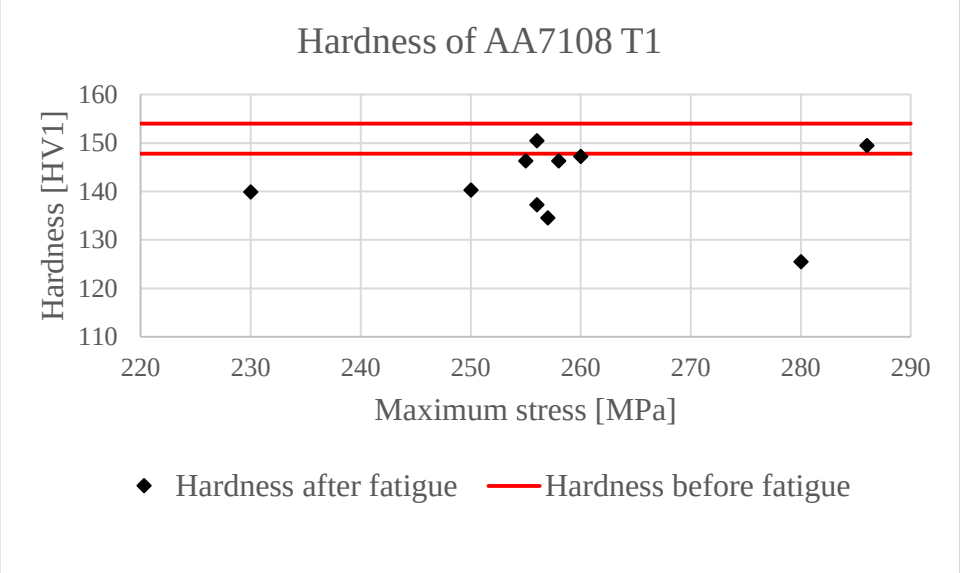

Figure 69: T1 specimens, the hardness before fatigue testing compared to the hardness after.

The hardness of the T4 specimens before fatigue testing compared to the hardness after fatigue testing is illustrated in Figure 70. The hardness has increased during fatigue, and hence cyclic hardening has occurred.

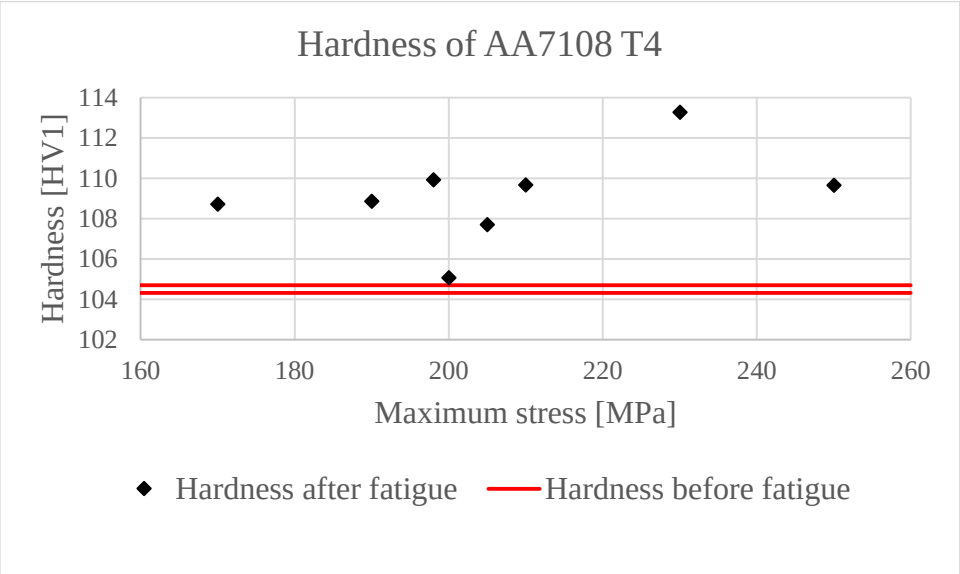

Figure 70: T4 specimens, the hardness before fatigue testing compared to the hardness after.

The hardness of the T5 before fatigue testing compared to the hardness after fatigue testing is illustrated in Figure 71. Most of the T5 specimens have a slightly lower hardness after fatigue testing, and therefore it seems as cyclic softening has occurred. This figure does not indicate a relationship between the hardness and the maximum stress.

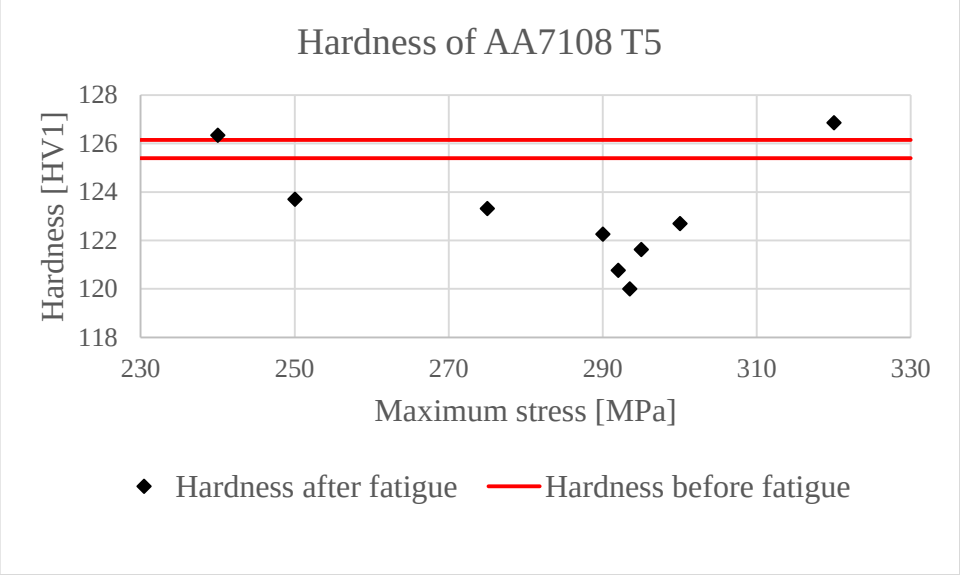

Figure 71: T5 specimens, the hardness before fatigue testing compared to the hardness after.

The hardness of the T6 specimens before fatigue testing compared to the hardness after fatigue testing is illustrated in Figure 72. It is difficult to decide whether cyclic hardening or cyclic softening has occurred, but it seems as the hardness decreases as the stress increases, and that hardening occurs at the low peak stress values.

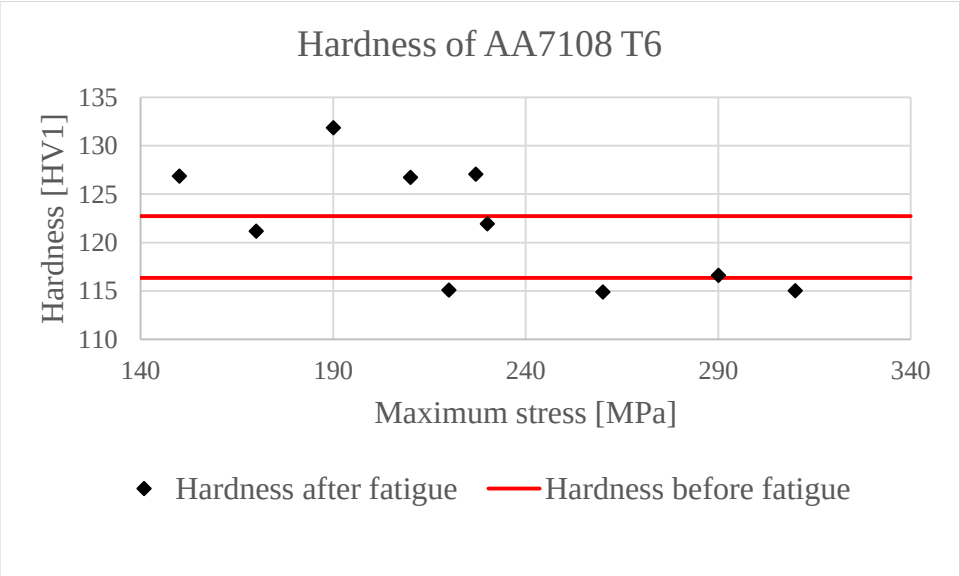

Figure 72: T6 specimens, the hardness before fatigue testing compared to the hardness after.

4.5 Fractography

Fractographs were taken on selected specimens from each SN-curve, hence from each temper state and alloy. For each curve, fractographs were taken from the specimen with the longest fatigue life before RO, the specimen with the shortest fatigue life and, if any, the most deviating specimen.

The fractographs were taken to underline the fatigue properties, and not to establish the entire fracture surface of all specimens. Therefore, the most representative fractographs with the most important features will be presented in this chapter. The additional fractographs are attached in Appendix C - Fractography. The details of each fractograph will be included in the figure caption.

In the following text, the features on the fractured surfaces of AA6082 will first be presented, followed by AA7108. The red square in many of the fractographs indicates that an area will be enlarged in the image next to or below the image with the red square.

4.5.1 Fractography of AA6082

For AA6082, either of the temper states had deviating SN-curve specimens, hence the fractographs are taken on specimens with a long or short fatigue life. There are two main differences between these two. First, the size of the fatigue fractured area was always larger for the specimens with the longest fatigue life (tested with a lower maximum stress). Second, for some of the specimens with a short fatigue life (tested with maximum stresses above or close to the yield strength), there are several fatigue fractured areas.

In the following sub-chapter, representative fractographs will be presented in terms of crack initiation, stage II crack propagation and final fracture. Please keep in mind that all fatigue specimens were parallel to TD.

The fatigue fractured surface

The fractured surface of AA6082 T5 with the longest fatigue life before RO is displayed in Figure 73. This fractured surface represents roughly all of the AA6082 specimens with the longest fatigue life, in addition to T5 with the shortest fatigue life. It contains all the important features of a fatigue fractured surface.

The fatigue fractured area is to the right, enclosed by the red line, while the final fracture is to the left. The numbers 1-3 are the fracture initiation point, the area of stage II crack growth and the final fracture, respectively. On a macroscopic level, the fatigue fractured area was plane and normal to TD, while the final fracture was a shear fracture with a ~ 45º angle to TD.

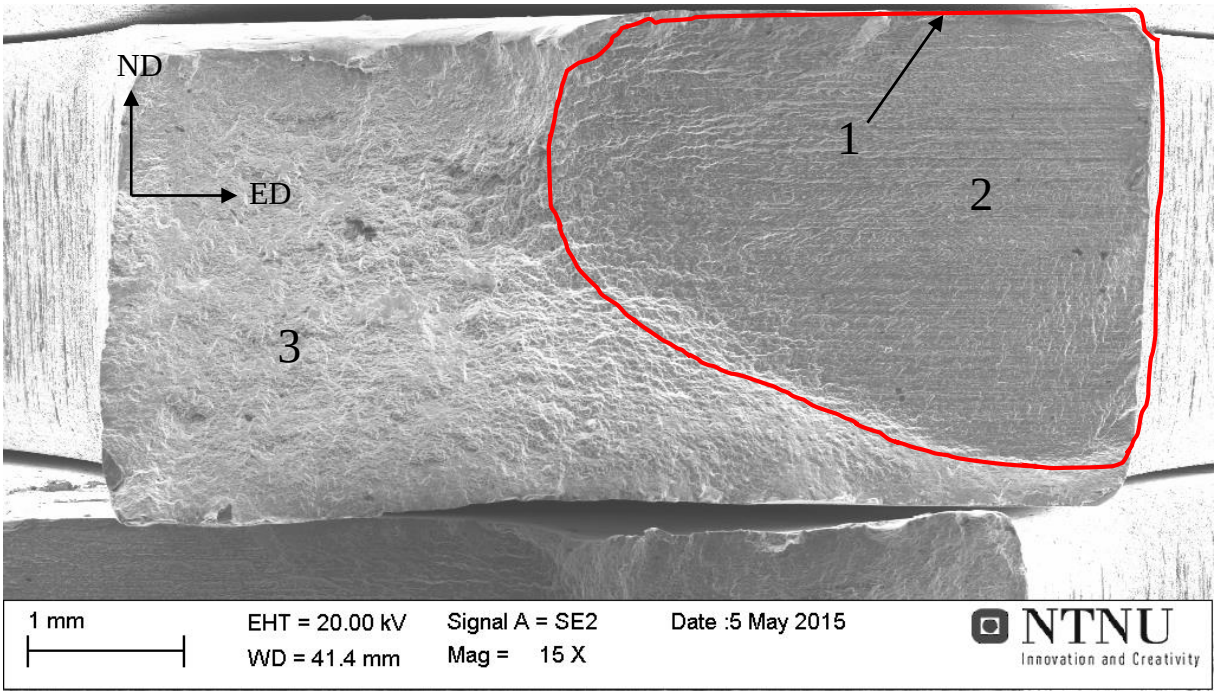

*Figure 73: An overview of the fractured surface of **AA6082 T5 with the longest fatigue life**, 15X magnification.*

Figure 74 shows the fractured surface of AA6082 T4 with the shortest fatigue life, and this fractograph is also representative for T1-and T6 with the shortest fatigue life. There are three fatigue fractured areas on this specimen, all enclosed by a red line. Mutual for these specimens is the high maximum stress (close to or above the yield strength) during testing. The largest fatigue fractured area was likely the one leading to failure.

The numbers 1-3 are the fracture initiation point, the area of stage II growth and the final fracture, respectively. The final fracture was ductile with dimples at 3a) and ductile with micro shear at 3b). On a macroscopic level, the fatigue fractured areas were plane and normal to TD, while the final fracture had a shear character with a ~ 45º angle to TD on each side of the green middle line.

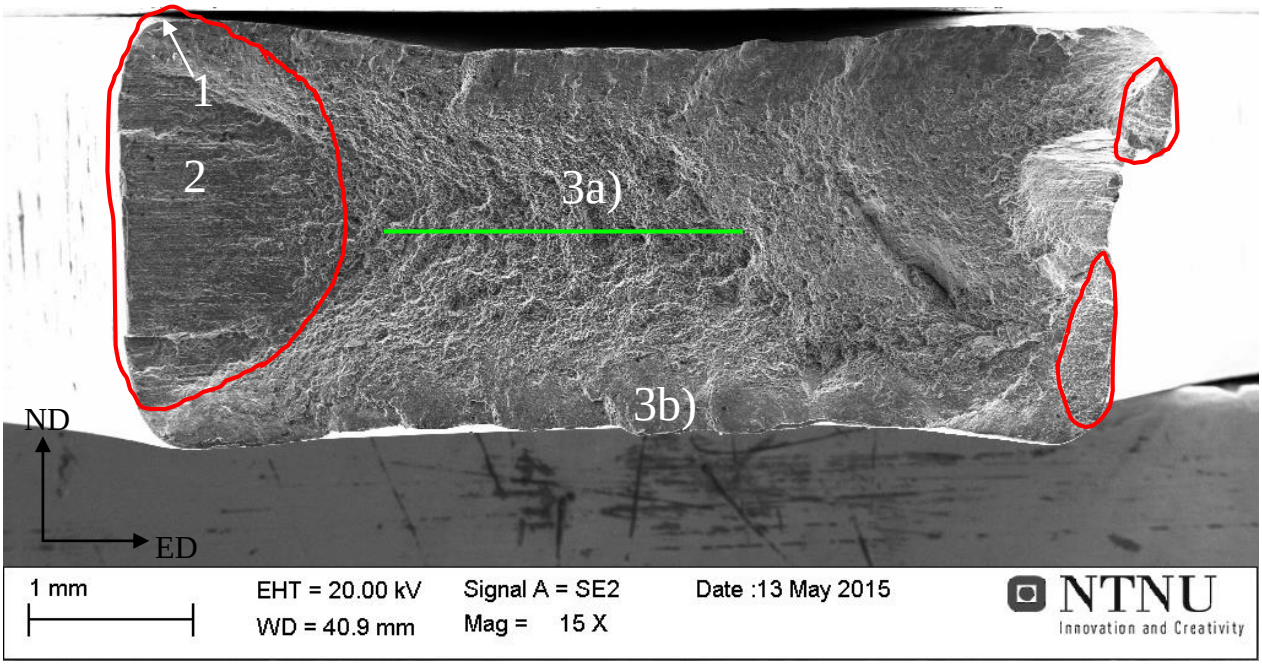

*Figure 74: An overview of the fractured surface of **AA6082 T4 with the shortest fatigue life**, 15X magnification.*

Crack initiation

The initiation points of AA6082 never looked exactly the same and therefore two different cases will be presented. A possible initiation point at the specimens edge on AA6082 T1 with the longest fatigue life is presented in Figure 75. Figure 75a) shows slip bands and "shelf's" produced by intersecting slip bands, which can have acted as an initiation point. A large secondary crack is also visible on Figure 75. Figure 75b) shows the slip bands at higher magnifications.

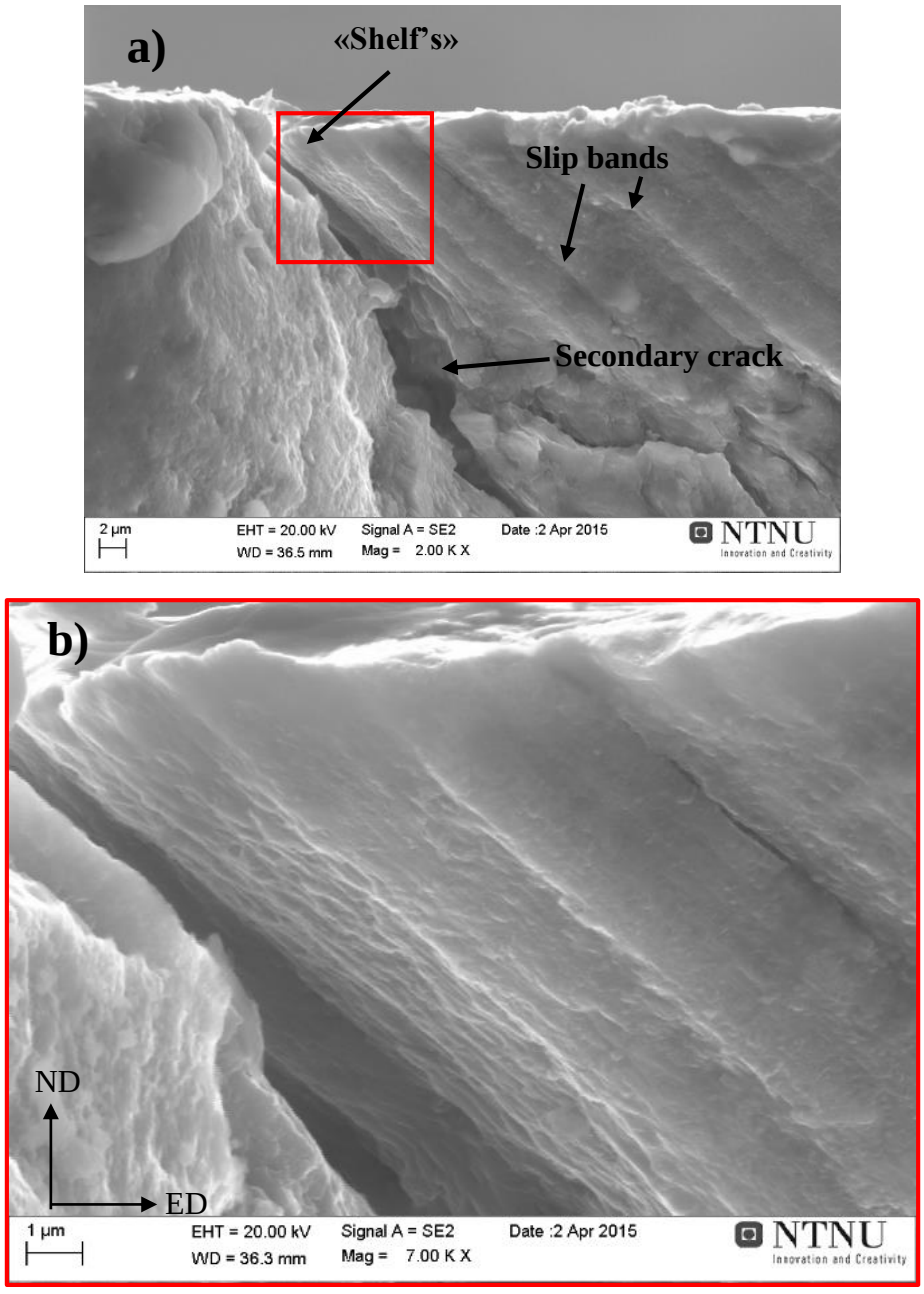

Figure 75: ***AA6082 T1 with the longest fatigue life****: a) A possible initiation point, at 2000X magnification and b) slip bands close to the initiation point, at 7000X magnification.*

Another possible initiation point is displayed in Figure 76, taken from the AA6082 T4 specimen with the longest fatigue life. Figure 76b) shows an enlargement of a large notch along the edge of the specimen where the crack can have initiated, i.e. the initiation originated from surface roughness. Slip bands inside the notch can be seen, they are approximately 0.2-0.4µm wide. Slip bands are also possible to see with super imposed striations crossing in Figure 76a). Here, the outer surface roughness is larger than 2µm, hence the surface roughness has increased during fatigue testing and probably produced some crack initiation sites. The increase in surface roughness applied to all AA6082 specimens.

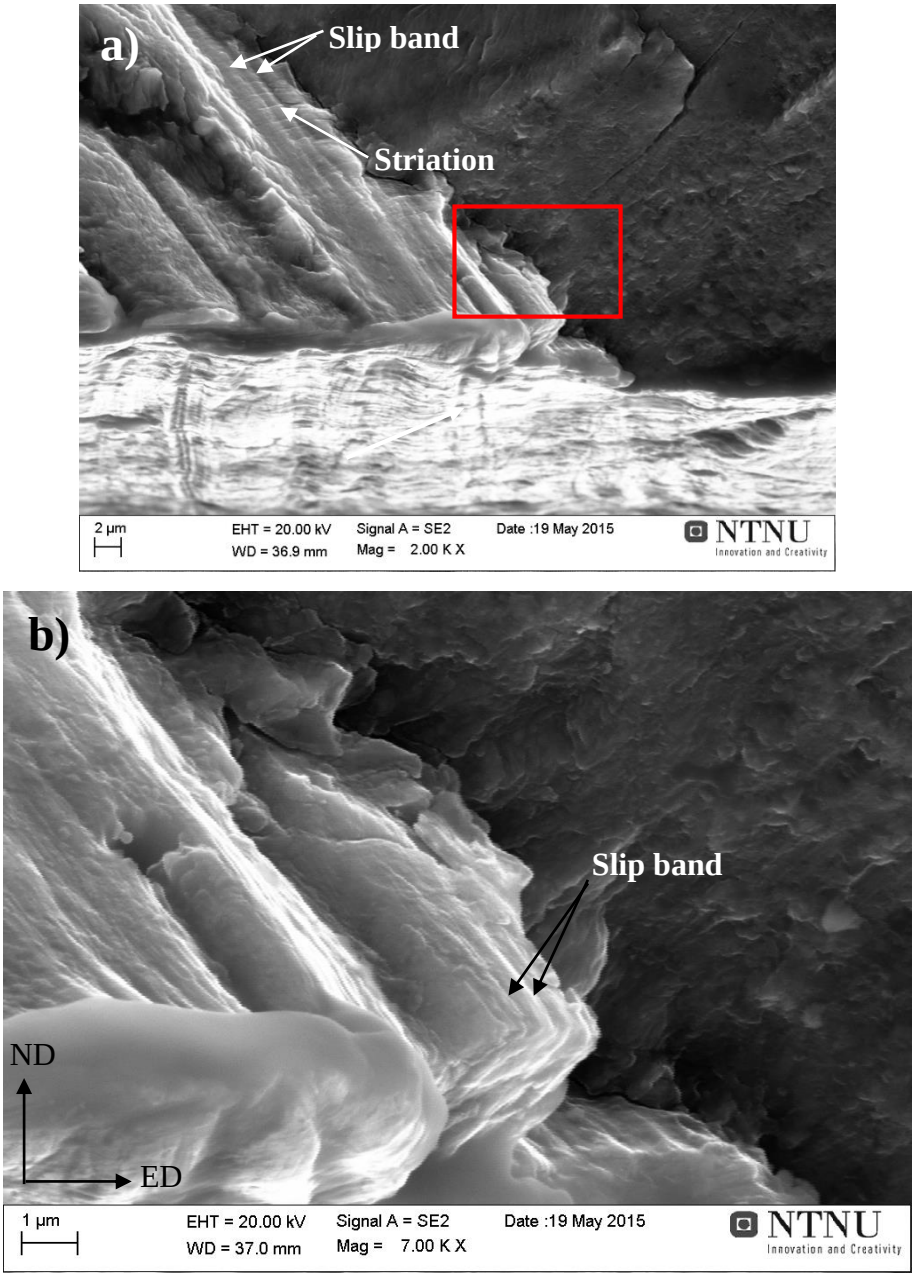

Figure 76: ***AA6082 T4 with the longest fatigue life*****:** *a) A possible initiation point, at 2000X magnification and b) the initiation point with slip bands, at 7000X magnification.*

Crack propagation

Stage II crack propagation for all AA6082 specimens is transgranular, as can be seen in Figure 77. In addition to transgranular growth, several secondary cracks and pores are possible to see in Figure 77b) together with short striations, created by slip. The secondary cracks could be along grain boundaries in ED. Figure 77 is taken from AA6082 T5 with the longest fatigue life.

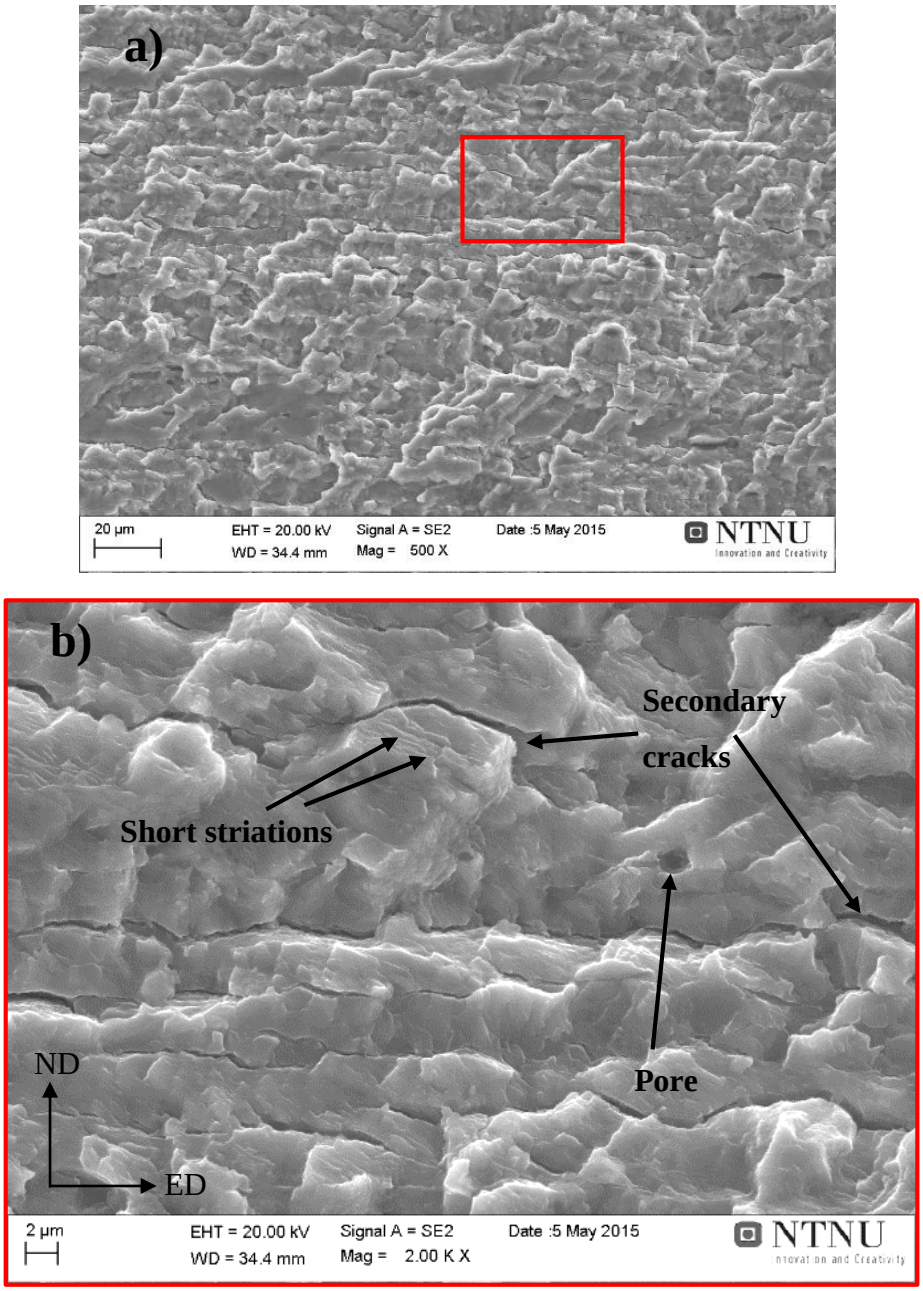

Figure 77: ***AA6082 T5 with the longest fatigue life****: a) Transgranular growth, at 500X magnification, and b) short striations, secondary cracks and a pore, at 2000X magnification.*

Crack propagation near the transition of stage II crack growth, to final fracture, is shown in Figure 78. The figure reveals long striations and dimples (micro voids), i.e. the crack propagation is now partly driven by the creation of dimples. In Figure 78b) long, classical striations are clearly visible. Figure 78 is taken of AA6082 T1 with the longest fatigue life and represents generally all AA6082 specimens.

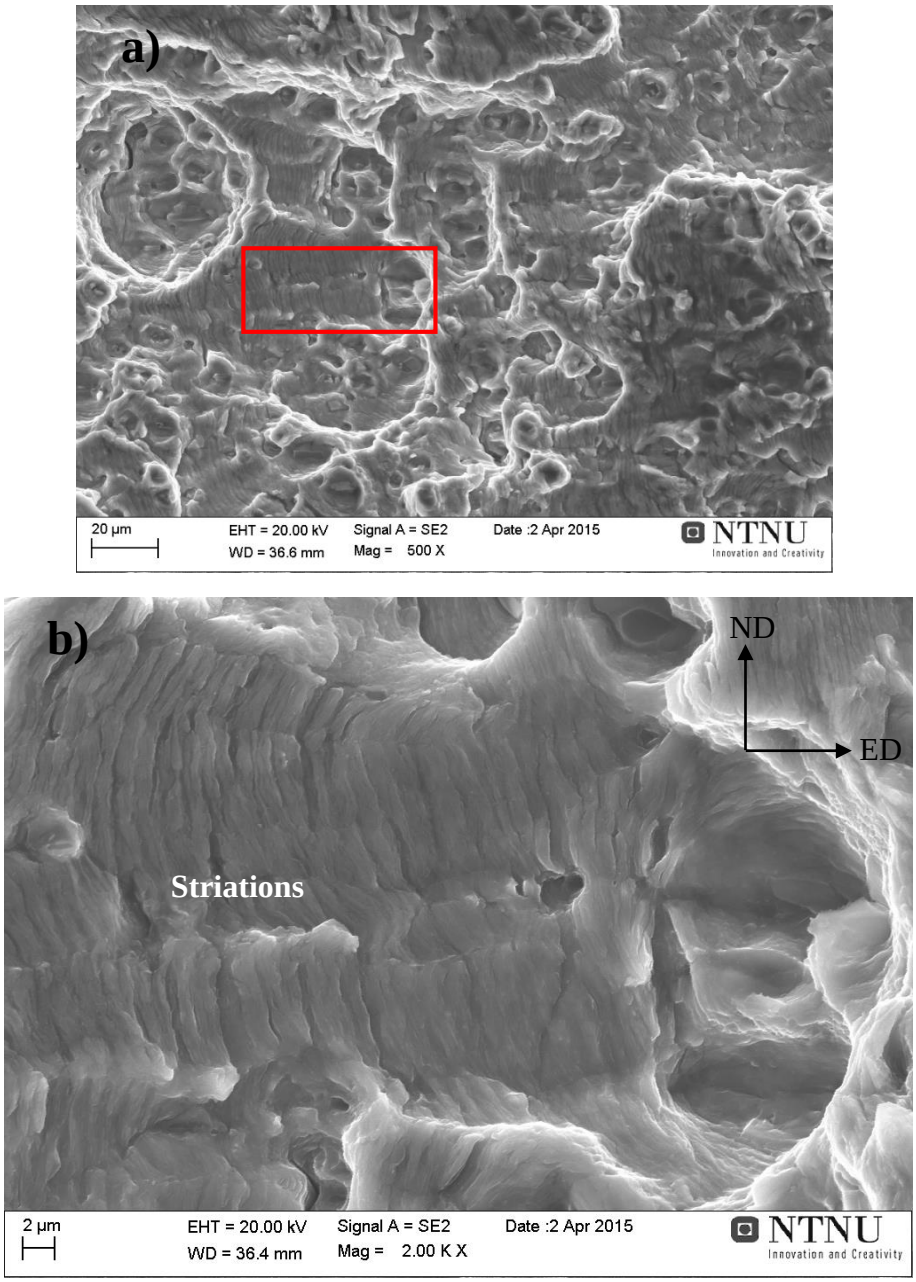

Figure 78: ***AA6082 T1 with the longest fatigue life****: a) Dimples and striations, at 500X magnification, and b) classical striations, at 2000X magnification.*

Slip localized growth in between the transgranular growth was observed for AA6082 T1- and T4 with the shortest fatigue life. Slip localized growth is shown in Figure 79a), and enlarged in Figure 79b). Mutual for T1 and T4 with the shortest fatigue life is the high maximum stress. Also, note the clearly visible grain boundary stretching out in ED, i.e. secondary GB-cracking seems to appear. Figure 79 is taken of T1 with the shortest fatigue life.

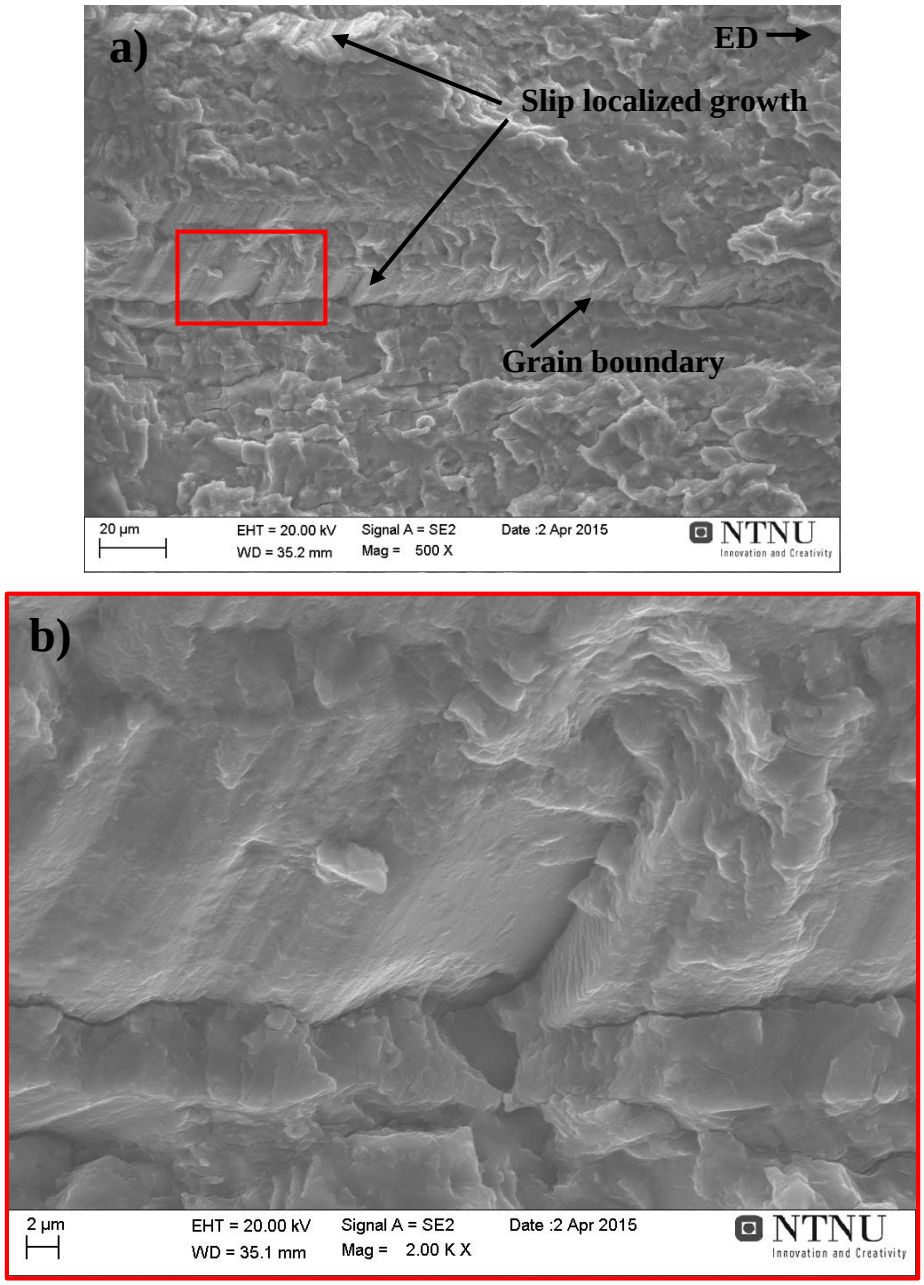

Figure 79: ***AA6082 T1 with the shortest fatigue life****: a) Slip localized growth in between transgranular growth, at 500X magnification, and b) enlarged slip localized growth, at 2000X magnification.*

Final fracture

The features of the final fractures of AA6082 specimens were all more or less the same. The final fractures were ductile, with both micro shear and dimples as seen in Figure 80. This type of final fracture applies for T1, T5 and T6, and Figure 80 is of AA6082 T5 with the longest fatigue life.

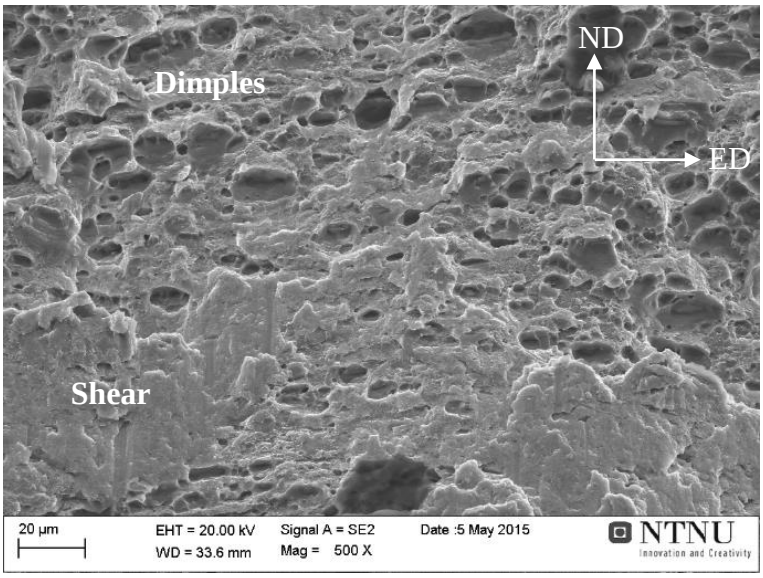

*Figure 80: **AA6082 T5 with the longest fatigue life**: Final fracture at 500X magnification, having a mixed mode with both dimples and micro shear.*

The final fracture shown in Figure 81 also reveals shear and dimples, but in contrast to the fracture in Figure 80, these two features were found at different places on the fractured surface. The dimples were seen in the middle of the specimen and the micro shear was found at the edges. This type of final fracture applies for the T4, and Figure 81 is of AA6082 T4 with the shortest fatigue life.

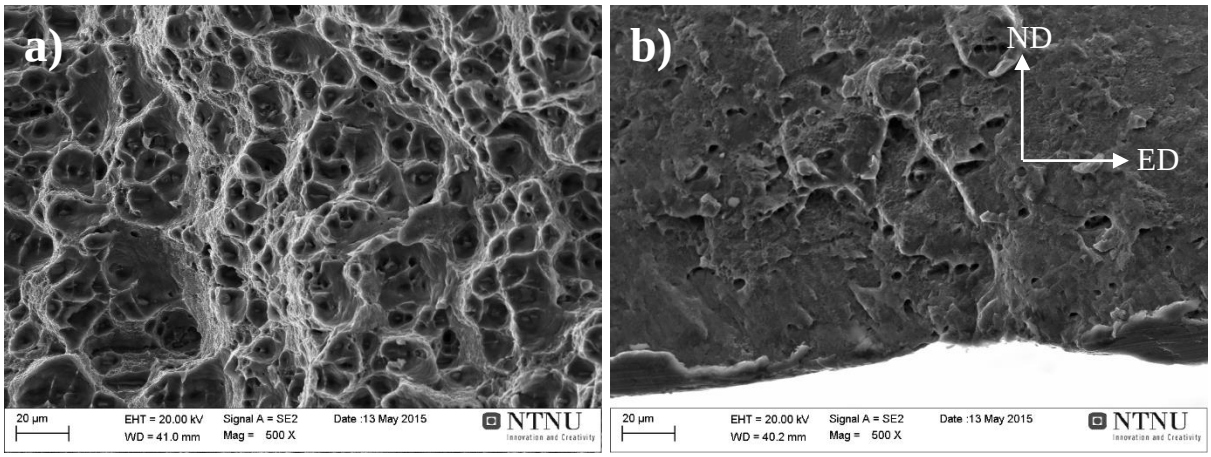

*Figure 81: **AA6082 T4 with the shortest fatigue life**: The final fracture, at 500X magnifications a) dimples, b) micro shear. The coordinate system is valid for both a) and b).*

A summary of the different stage II crack and final fracture mechanisms of AA6082 is displayed in Table 19. All correspondingly fractographs can be found in Appendix C – Fractography.

Table 19: A summary of the stage II crack propagation and final fracture mechanisms for the AA6082 tempers.

Specimen	**Stage II crack propagation mechanism**	**Final fracture**
T1 longest fatigue life	Transgranular Some degree of slip localization	Dimples Micro shear
T1 shortest fatigue life	Slip localized Transgranular Secondary GB-cracking	Dimples Micro shear
T4 longest fatigue life	Transgranular Some degree of slip localization	Dimples (middle) Micro shear (edge)
T4 shortest fatigue life	Slip localized Transgranular	Dimples (middle) Micro shear (edge)
T5 longest fatigue life	Transgranular Some degree of slip localization	Dimples Micro shear
T5 shortest fatigue life	Transgranular Some degree of slip localization	Dimples Micro shear
T6 longest fatigue life	Transgranular	Dimples Micro shear
T6 shortest fatigue life	Transgranular	Dimples Micro shear

4.5.2 Fractography of AA7108

The following fractographs are taken of selected specimens with the longest or shortest fatigue life of each temper. As for the previous alloys , the main difference between the specimens with long and short fatigue life, i.e. the size of the fatigue fractured area was always larger for the specimens with the longest fatigue life.

The following representative fractographs will be presented in the following order, fatigue crack initiation, stage II crack propagation, final fracture and finally deviating behaviors.

The fatigue fractured surface

The fractured surface of AA7108 T6 with the longest fatigue life before RO is displayed in Figure 82. This fractured surface represents qualitatively both AA7108 T6 and T5 tempers.

The fatigue fractured area is displayed to the left, enclosed by the red line, while the final fracture is to the right. The numbers 1-3 are the fracture initiation point, the area of stage II crack growth and the final fracture, respectively. On a macroscopic level, the fatigue fractured area was plane and normal to TD, while final fracture showed shear with a ~ 45º angle to TD.

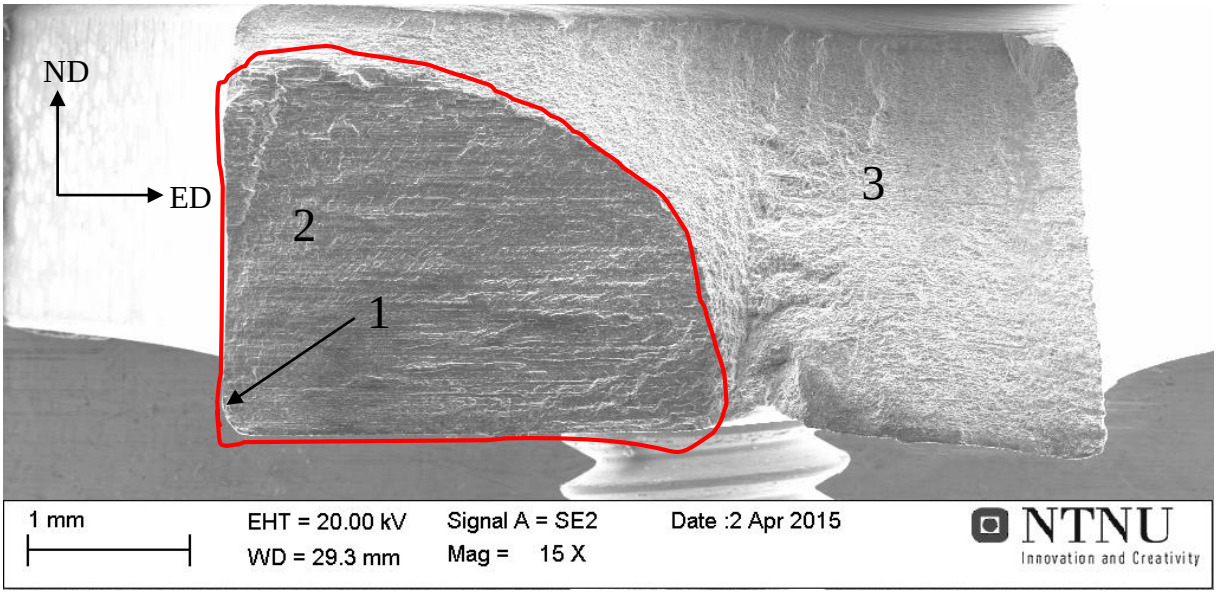

Figure 82: ***AA7108 T6 with the longest fatigue life:*** *An overview of the fractured surface, 15X magnification.*

The fractured surface of AA7108 T4 with the longest fatigue life before RO is shown in Figure 83. This is also representative for condition T1 and T4, both with the shortest fatigue life.

The fatigue crack area is to the right, encircled by the red line, while final fracture is to the left. Note that the fatigue fractured has large cracks, in contrast to the same area for T5 and T6 above. The numbers 1-3 are the fracture initiation point, the area of stage II crack growth and final fracture, respectively. Also here, the fatigue crack was normal to TD, while final fracture was a shear fracture having a 45º angle to TD.

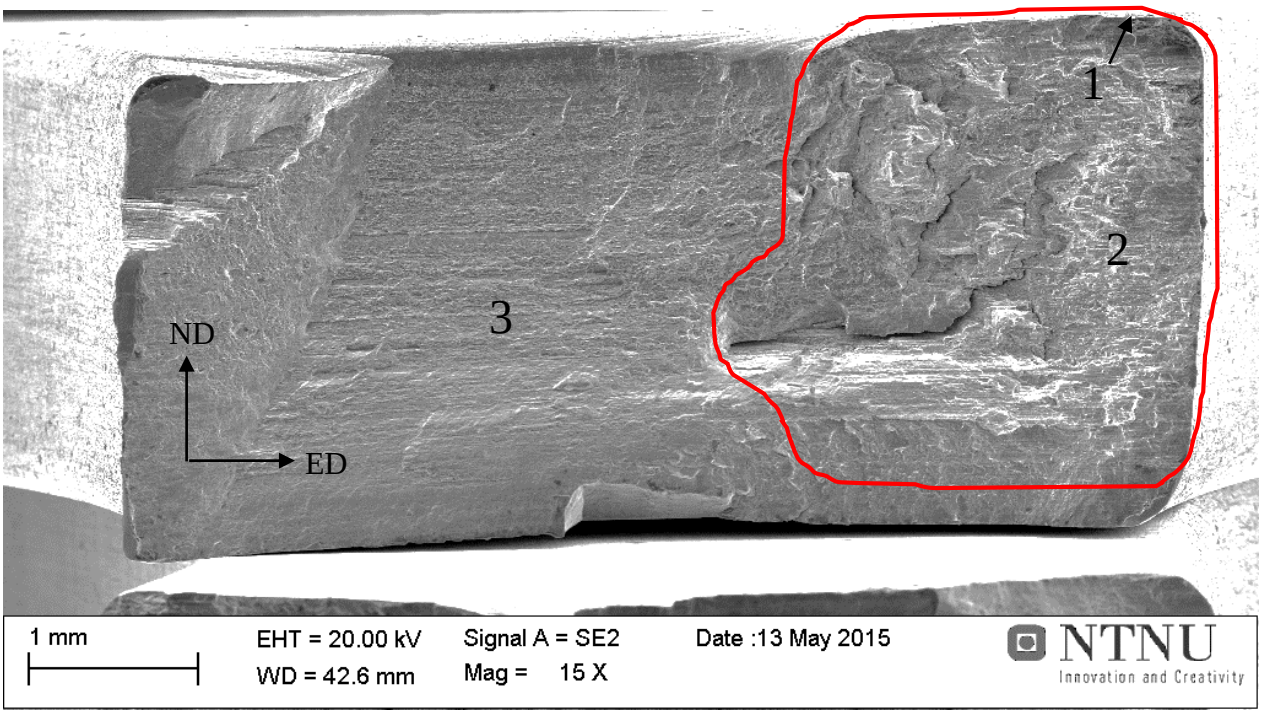

Figure 83: ***AA7108 T4 with the longest fatigue life:*** *An overview of the fractured surface, 15X magnification.*

Crack initiation

As for AA6082, non of the observed initiation points looked exactly the same, but as they have similar features, the initiation point of two specimens will be displayed. Figure 84 shows the initiation point in of AA7108 T5 with the longest fatigue life. A notch along the specimen edge where initiation might have occurred can be seen. In Figure 84b) oxidation is possible present, indicating a slow initiation process. Note that the outer surface is visible and that the surface roughness is larger than 2µm, indicating that the surface roughness has increased during testing, e.g. applies for all AA7108 specimens.

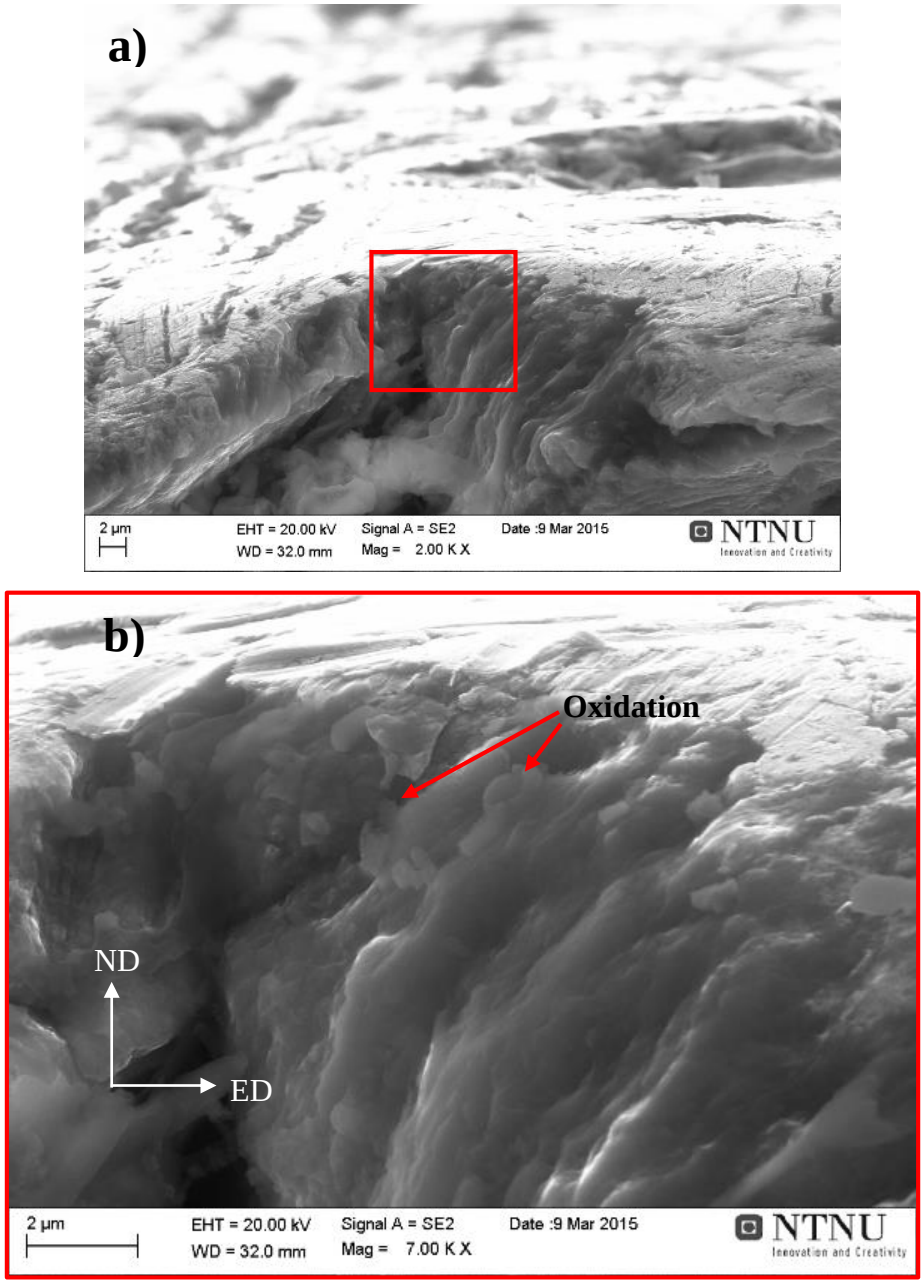

Figure 84: ***AA7108 T5 with the longest fatigue life*** *a) A possible initiation point at 2000X magnification and b) a close-up on the initiation point with oxidation, at 7000X magnification.*

Figure 85 displays a possible initiation point inside the groove along the surface edge on AA7108 T1 with the longest fatigue life. Figure 85a) shows slip lines emerging from inside the groove with striations crossing. Figure 85b) is an enlargement of the striations.

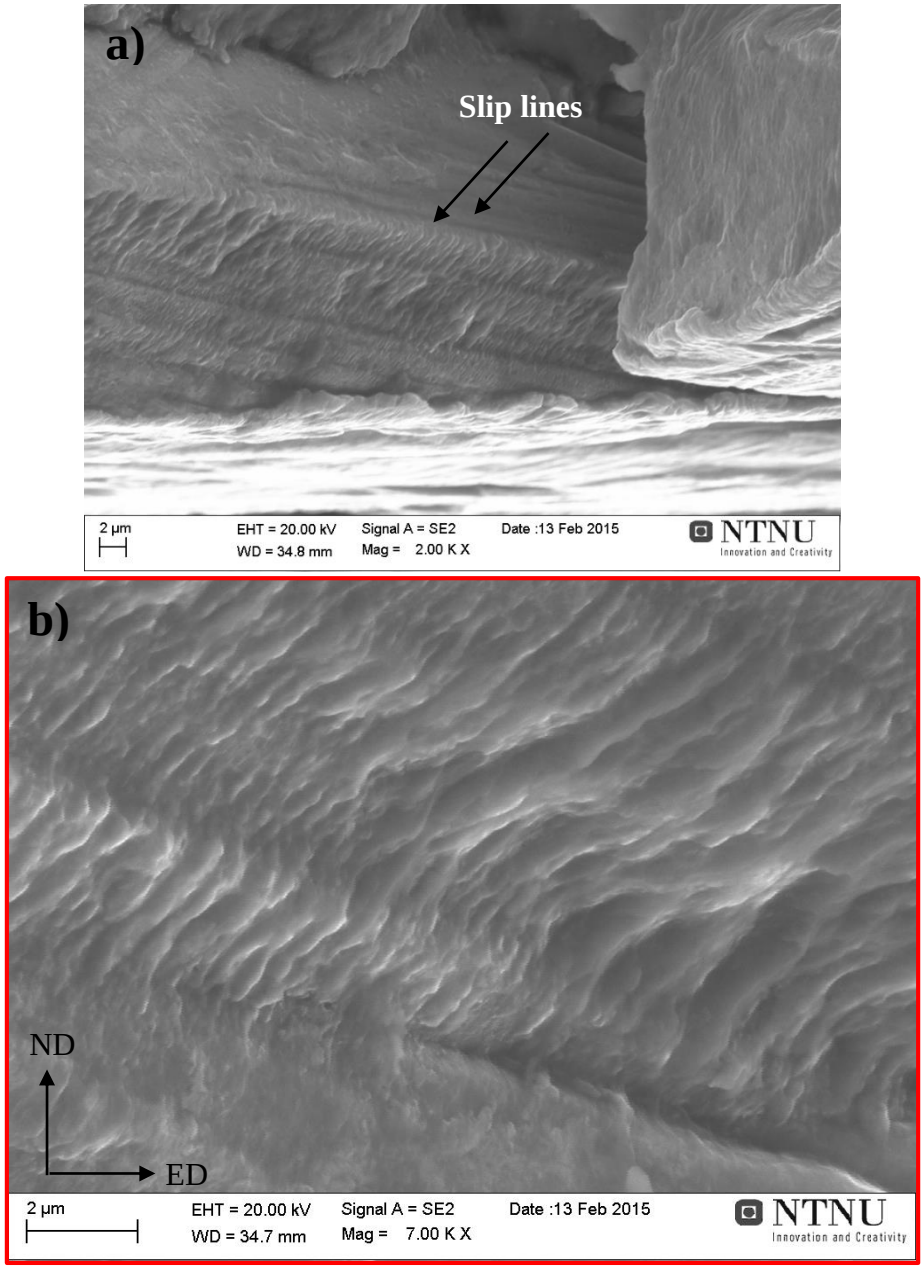

Figure 85: ***AA7108 T1 with the longest fatigue life:*** *a) A possible initiation point inside the groove, at 2000X magnification, b) striations at 7000X magnification.*

Crack propagation

Stage II crack propagation in the AA7108 T1 temper is shown in Figure 86, e.g. a highly slip localized growth with a large amount of intersecting slip bands. In Figure 86b), both long and short striations are visible. Figure 86 is taken of T1 with the shortest fatigue life.

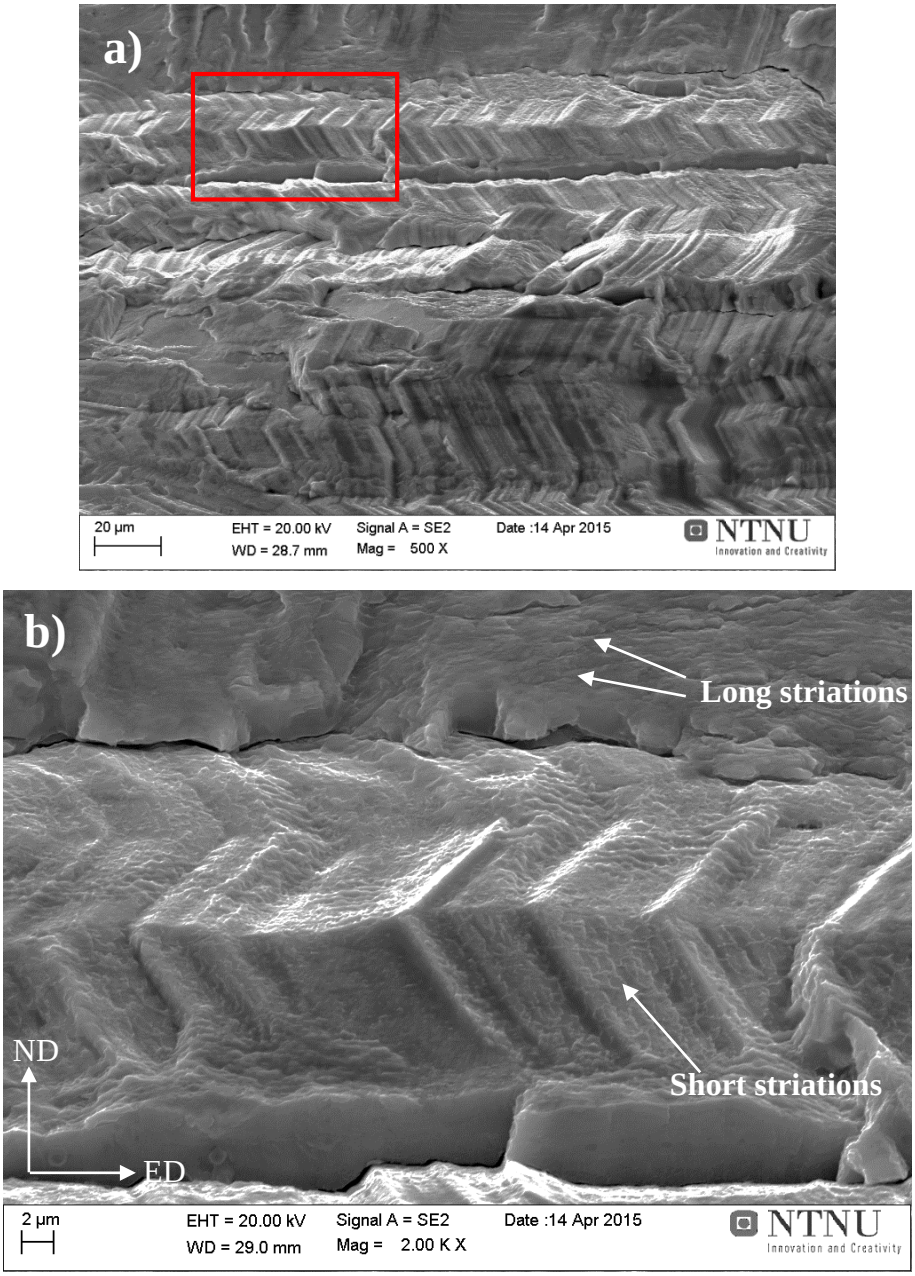

Figure 86: ***AA7108 T1 with the shortest fatigue life****: Stage II crack propagation at a) at 500X magnification, and b) slip steps and short striations at 2000X magnification.*

Figure 87 shows a mixed mode growth with both transgranular and slip elements. This mixed mode was dominating for the T4 and T5 temper in addition to the T6 temper with the shortest fatigue life. Striations are recognizable in Figure 87b). Note the growth direction and the clearly visible grain boundaries stretching out in ED in Figure 87b), i.e. secondary GB-cracking seems to appear. Please note that, GB-cracking in different degrees was found for all AA7108 tempers. Figure 87 is taken of T5 with the shortest fatigue life.

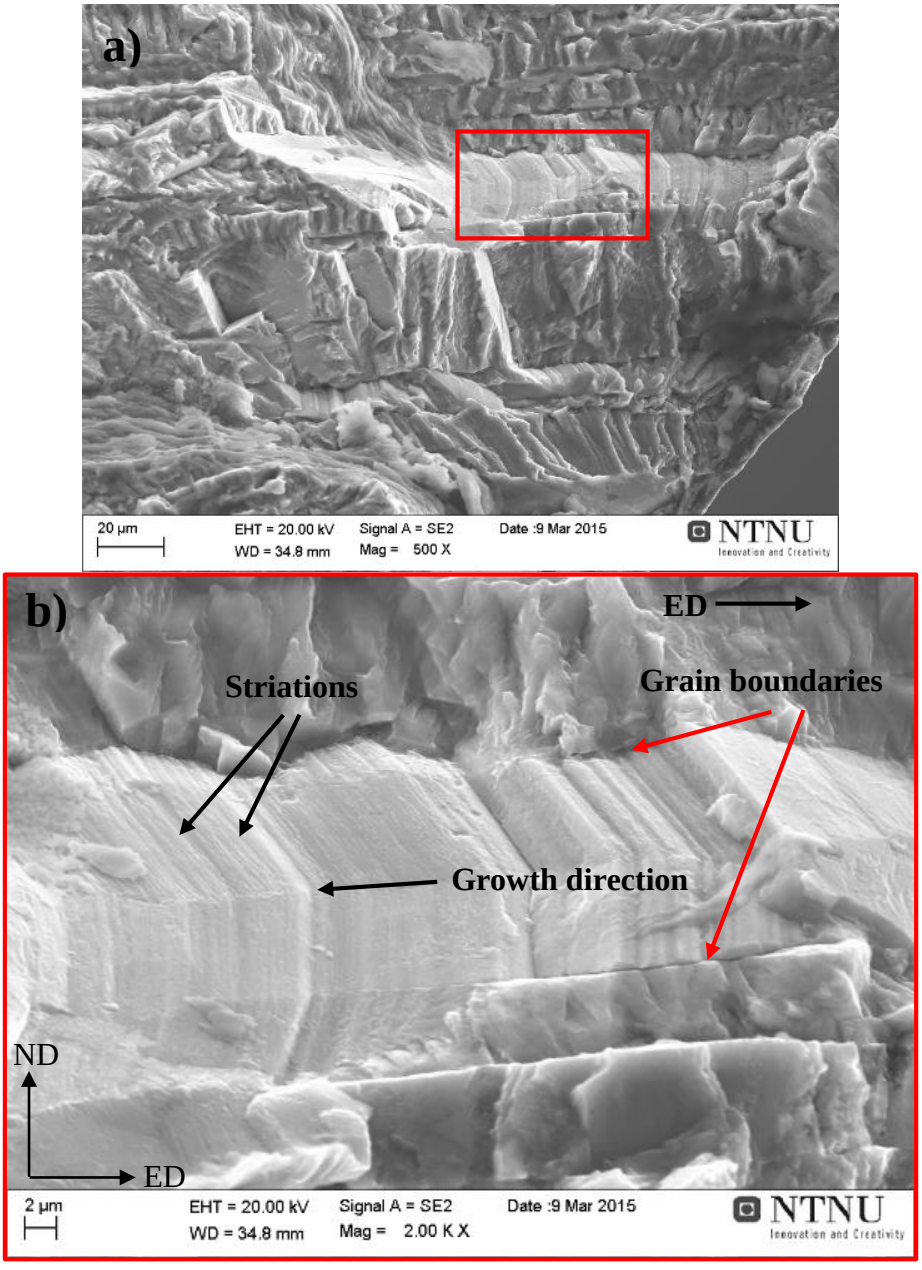

Figure 87: ***AA7108 T5 with the shortest fatigue life:*** *The crack propagation area a) at 500X magnification, and b) a grain with striations, at 2000X magnification.*

The transgranular crack propagation in Figure 88 was dominating for AA7108 T6 with the longest fatigue life. Figure 88b) shows secondary cracks, short striations formed by slip and possible cracks along the grain boundaries from secondary GB-cracking.

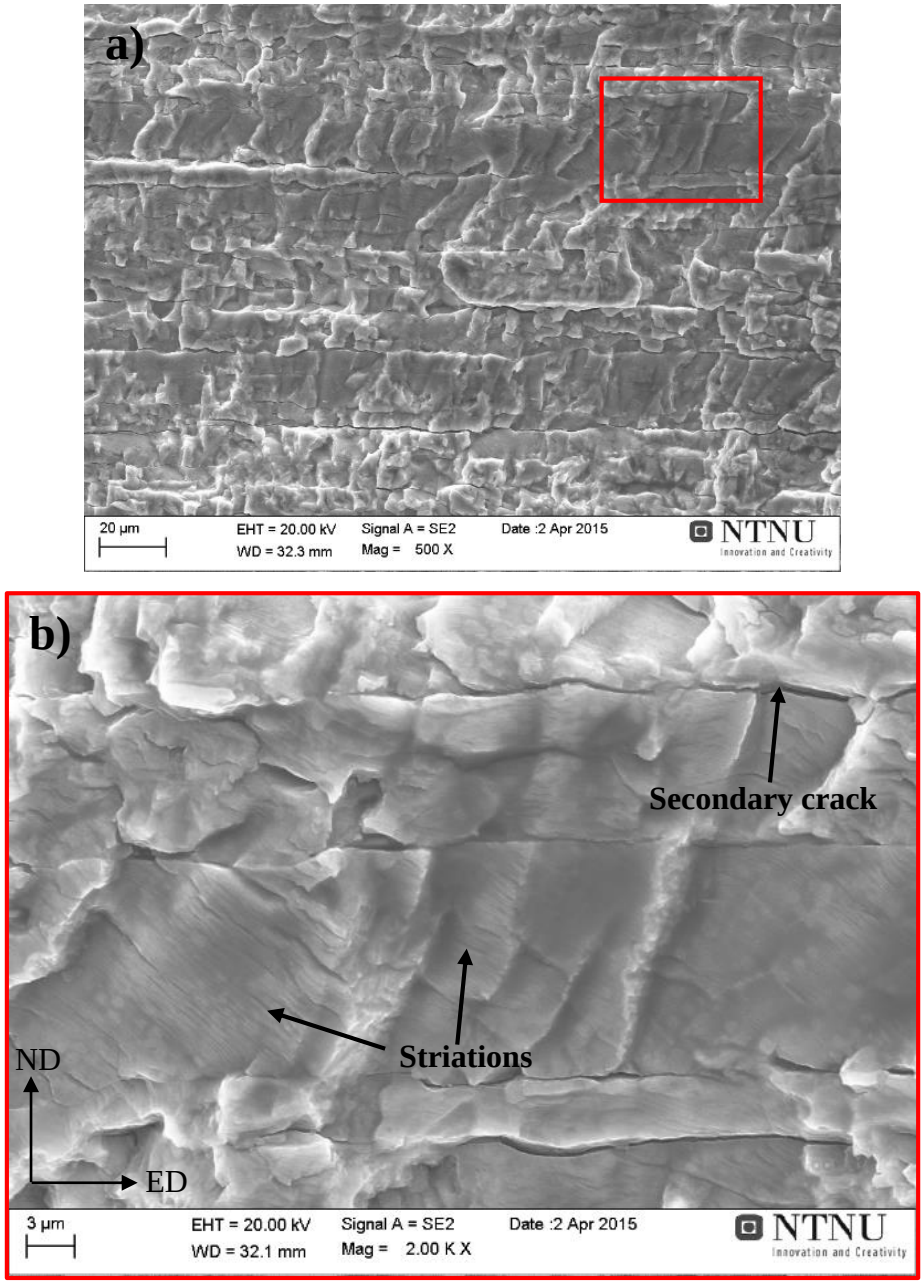

*Figure 88:**AA7108 T6 with the longest fatigue life**: Transgranular crack growth with 500X magnification, and b) short striations and a secondary crack with 2000X magnification.*

Final fracture

The final fracture in AA7108 T1 with the longest fatigue life is displayed in Figure 89. This temper state had sheared-off slip bands in between the dimples.

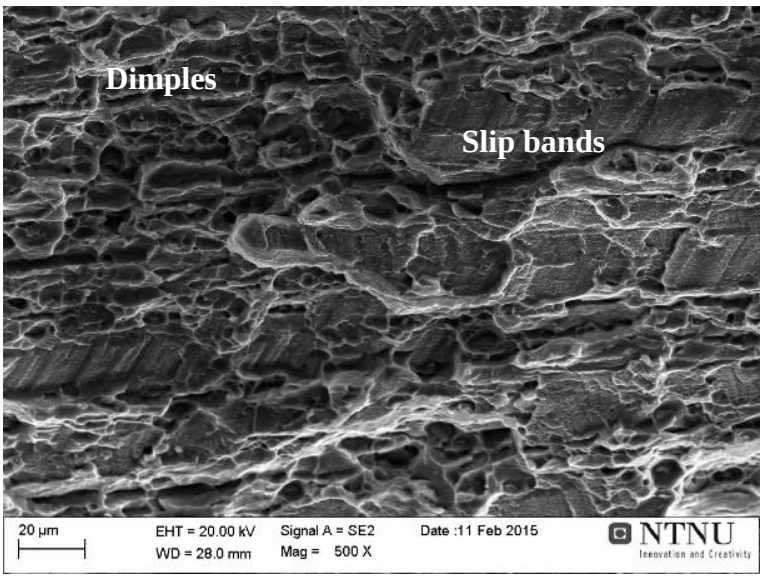

Figure 89: ***AA7108 T1 with the longest fatigue life:*** *The final fracture with dimples and sheared slip bands, with a magnification of 500X.*

All other investigated AA7108 specimens had final fractures as the one in Figure 90, a ductile mixed mode with both micro shear and dimples. Figure 90 is taken of T5 with the longest fatigue life.

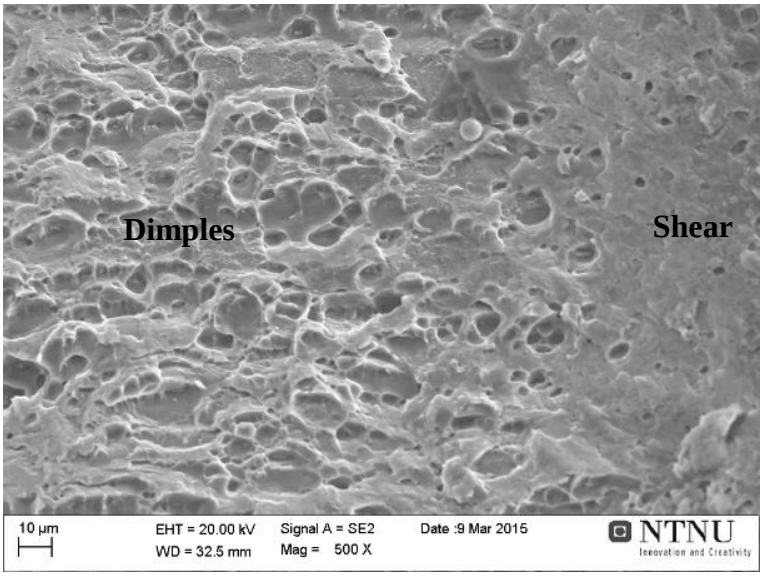

Figure 90: ***AA7108 T5 with the longest fatigue life:*** *The final fracture, with a magnification of 500X.*

Deviating specimens

The AA7108 had three clearly deviating specimens. These will be presented in the following.

The deviating AA7108 T1 specimen endured $2.40 \cdot 10^5$ cycles at a maximum stress of 255 MPa before failure. According to the rest of the results, a maximum stress of 255 MPa should lead RO, and hence this was the reason to investigate this fracture. A large crack (~1 mm) was observed and is displayed in Figure 91. It is most likely from machining of the fatigue specimens. Hence, the crack was probably present before fatigue testing and may be a reason for a deviating fatigue life.

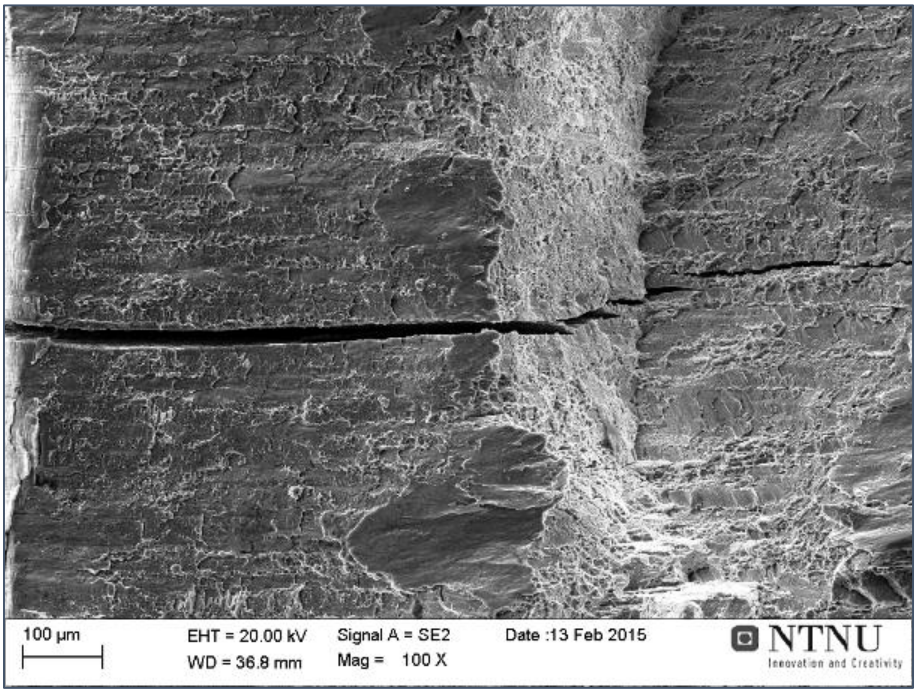

Figure 91: A crack, possible from machining of the fatigue specimen, 100X magnification.

The deviating AA7108 T4 specimen, fractured with a maximum stress of 200 MPa and $4.39 \cdot 10^5$ cycles before fracture. According to the rest of the results, a maximum stress of 200 MPa should lead to a longer fatigue life, and hence there was reason to investigate the fracture surface. Secondary cracks can be seen inside the fatigue fractured area in Figure 92 and Figure 93, respectively. The secondary cracks are numereous and quite large (300-500µm), and might be the reason for early failure.

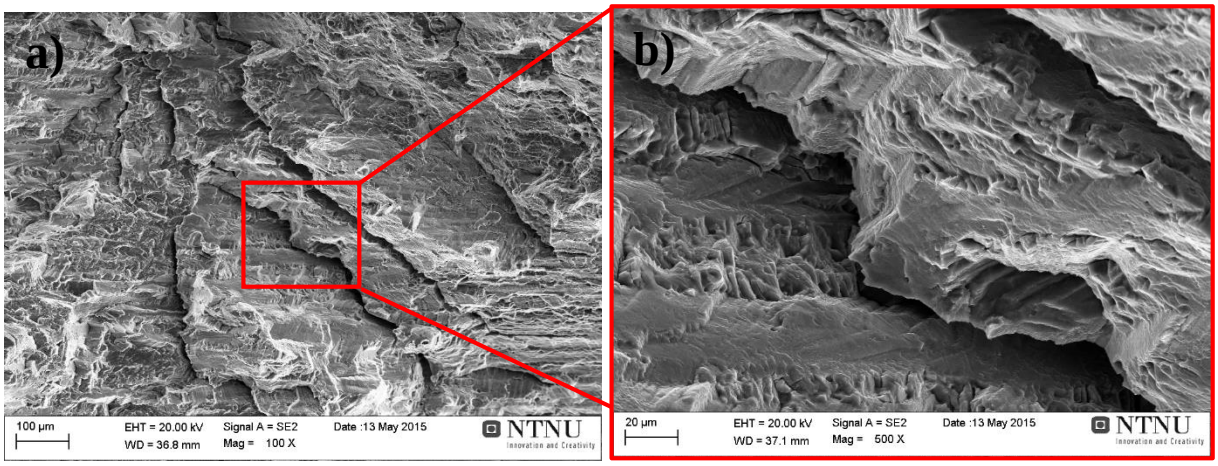

Figure 92: Secondary cracks in the fatigue fractured area taken with a magnification of a) 100X and b) 500X.

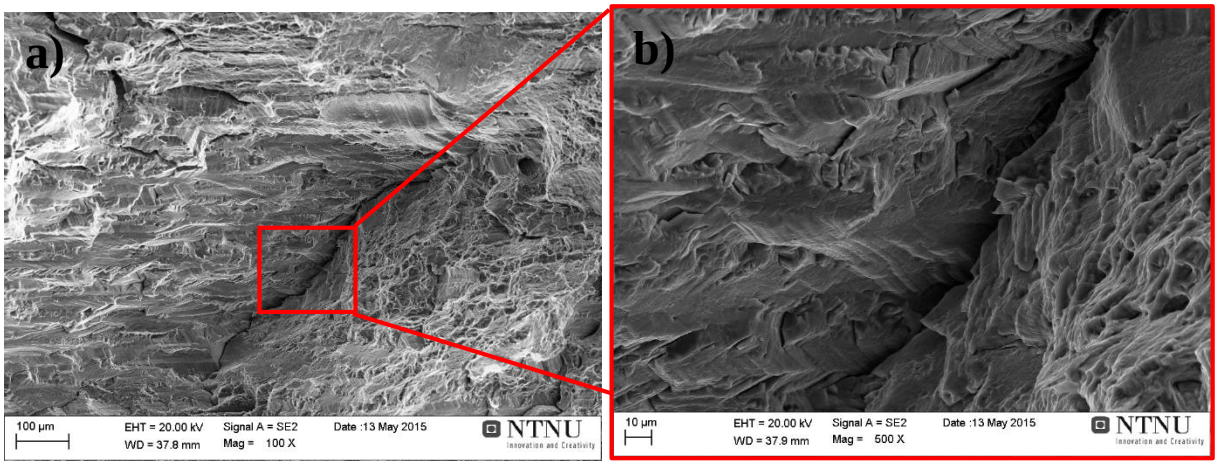

Figure 93: Secondary cracks in the fatigue fractured area taken with a magnification of a) 100X and b) 500X.

The deviating AA7108 T5 specimen endured $7.39 \cdot 10^5$ cycles at a maximum stress of 250 MPa before failure. This stress level should normally lead to RO, and hence further investigations were preformed. The area with deviation is presented in Figure 94, where corrosion seems to have happened.

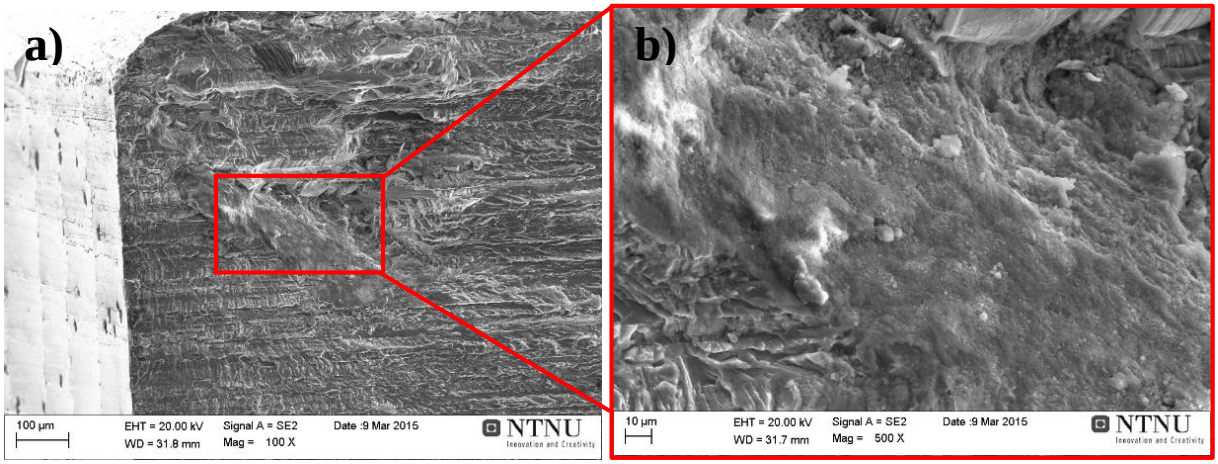

Figure 94: Possible corrosion fatigue, taken with a magnification of a) 100X and b) 500X.

EDS analysis confirmed corrosion in the area due to the high concentration of oxygen, see Table 20. EDS analysis was also done in an area where corrosion products were not found, and in this area the concentration of oxygen was low, see Table 21.

Table 20: Content in the corroded area.

Element	Oxygen	Aluminium	Magnesium	Zinc
wt%	46.65	48.44	0.91	4.00

Table 21: Content in an area without corrosion products.

Element	Oxygen	Aluminium	Magnesium	Zinc
wt%	4.46	87.55	1.12	6.51

Oxidation products were also observed on some other AA7108 specimens in the stage II crack propagation area, but as neither of these had a deviating fatigue life, these were not further investigated.

A summary of the different stage II crack mechanisms and final fractures of AA7108 is displayed in Table 22. All collected fractographs can be found in Appendix C – Fractography.

Table 22: A summary of the stage II crack propagation mechanisms and final fractures in the AA7108 tempers.

Specimen	**Stage II crack propagation mechanism**	**Final fracture**
T1 longest fatigue life	Slip localized Secondary GB cracking	Dimples Slip bands
T1 shortest fatigue life	Slip localized Secondary GB cracking	Dimples Micro shear
T4 longest fatigue life	Slip localized Transgranular growth Secondary GB cracking	Dimples Micro shear
T4 shortest fatigue life	Slip localized Transgranular Secondary GB cracking	Dimples Micro shear
T5 longest fatigue life	Slip localized Transgranular Secondary GB cracking	Dimples Micro shear
T5 shortest fatigue life	Slip localized Transgranular Secondary GB cracking	Dimples Micro shear
T6 longest fatigue life	Transgranular Secondary GB cracking	Dimples Micro shear
T6 shortest fatigue life	Slip localized Transgranular Secondary GB cracking	Dimples Micro shear

4.6 Grain structure and crystallographic texture

Here, grain maps and pole figures of as delivered material (the T1 temper state) and solution heat treated material (the T6 temper state) will be presented. The aim of texture analysis was to investigate the direct relationship between the directions of slip planes and the stress direction during fatigue.

4.6.1 Grain structure

The AA6082 T1 has a texture in the TD-ND-plane indicated by the grain map in Figure 95. This image shows the entire width of the TD-ND-plane, as can be recognized by the recrystallized edges. From the colors, one can imagine that the <111> (turquoise/blue) and <001> (red) are dominant orientations in the extrusion direction, which indicates a strong fiber texture.

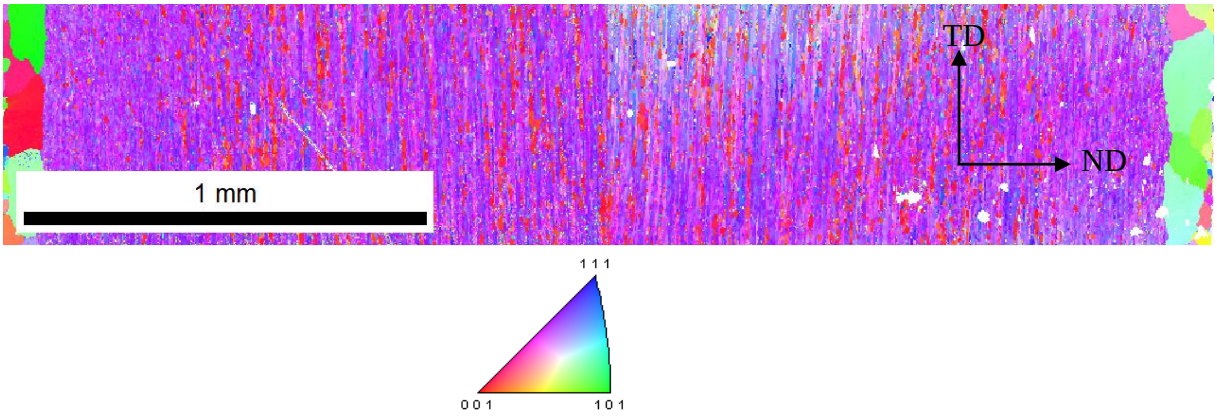

Figure 95: Grain map of AA6082 T1 with orientation color code below.

The AA6082 T6 has a texture in the TD-ND-plane indicated in the grain map in Figure 96. Again, the entire width of the TD-ND plane is shown, and the recrystallized layer from extrusion is visible. The texture is as expected very similar to the T1 condition. However, some recrystallized small grains are now visible as the red areas are smaller.

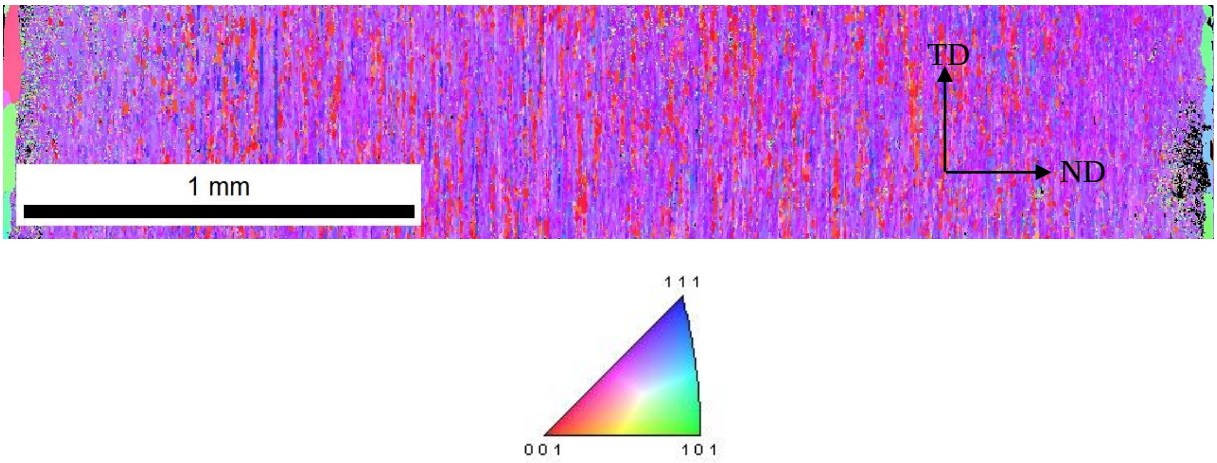

Figure 96: Grain map of AA6082 T6 with orientation color code below.

The AA7108 T1 had a texture in the TD-ND-plane indicated in the grain map in Figure 97. The grain map shows only one half of the surface width due to complications during EBSD analysis, but the pole figures below are made of data from the entire width of the TD-ND plane. As for AA6082, from the colors, one can imagine that the <111> (turquoise/blue) and <001> (red) are dominant orientations in the extrusion direction, which indicates a strong fiber texture.

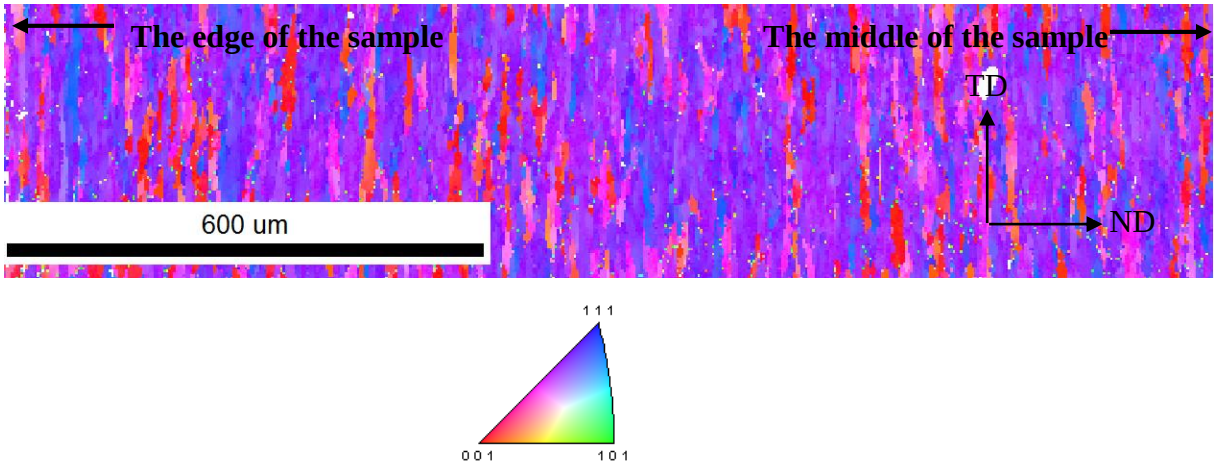

Figure 97: Grain map of AA7108 T1 with orientation color code below.

The AA7108 T6 has a texture in the TD-ND-plane indicated in the grain map in Figure 98. The grain map shows the entire width of the TD-ND plane. The texture is very similar to the T1 condition with the red color being the more dominant than for AA7108 T1.

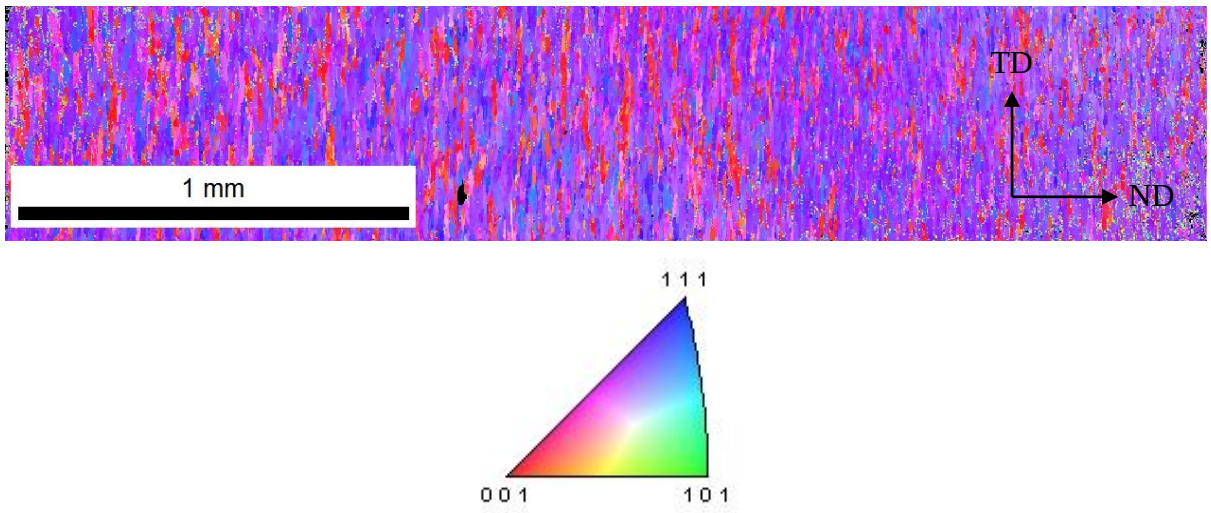

Figure 98: Grain map of AA7108 T6 with orientation color code below.

4.6.2 Crystallographic texture

The pole figures (shown below) all have clear intensity tops, hence these alloys and temper states have a texture. The grain maps indicate a similar texture of AA6082 and AA7108 in both temper states, and this is confirmed by the pole figures below, as they are all the same. The pole figures are made by data from the grain maps, which are sections of the TD-ND plane of approximately 0.6mm x 3mm. It is assumed that the texture of these sections represents the entire TD-ND-plane.

The (100) and (111) pole figures of AA6082 T1 and T6 and of AA7108 T1 and T6 is shown in Figure 99-Figure 102, respectively. The pole figures are all the same and hence the texture is the same for both alloys and all temper states. The intensity maximums are slightly larger for AA6082 than for AA7108, but the pole figures are still the same.

The (100) pole figure indicates the orientation of the unit cube, and the (111) pole figure indicates the slip directions. The (111) pole figures in Figure 99-Figure 102 have strong <111> projections, hence representing the plane normal of the {111} planes. The north and south pole of the (111) pole figure are made up from {111} planes with an angle of around 90º to TD, while the two dots in the middle are made up from {111} planes with an angle of close to 0º (~ 8-10º) to TD. The middle of the two half moons on the other hand, are made up from {111} planes with an angle of 45º to ND, while the ends of the two half moons are {111} with an angle ~ 45º to TD, ND and ED. These are marked only on Figure 99. The pertaining inverse pole figures for both alloys are found in Appendix D – Inverse pole figures.

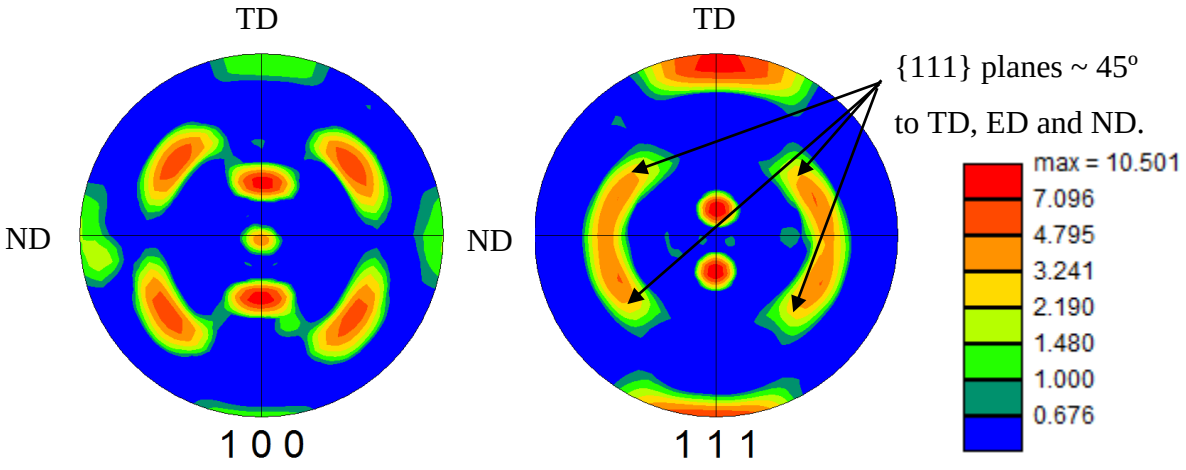

*Figure 99: (100) and (111) pole figures of **AA6082 T1** for the entire TD-ND-plane, with an intensity bar to the right. The {111} planes ~45º to TD are marked.*

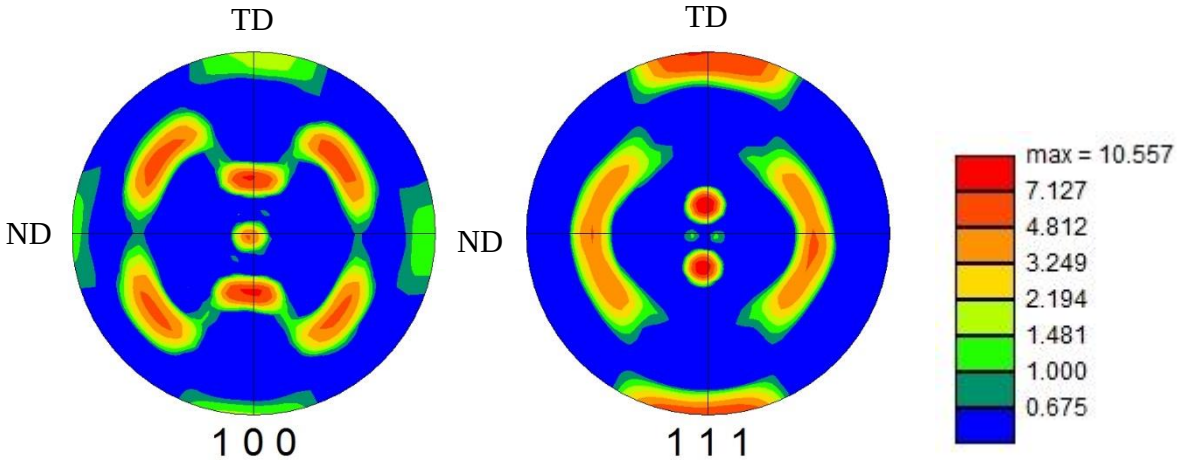

*Figure 100: (100) and (111) pole figures of **AA6082 T6** for the entire TD-ND-plane, with an intensity bar to the right.*

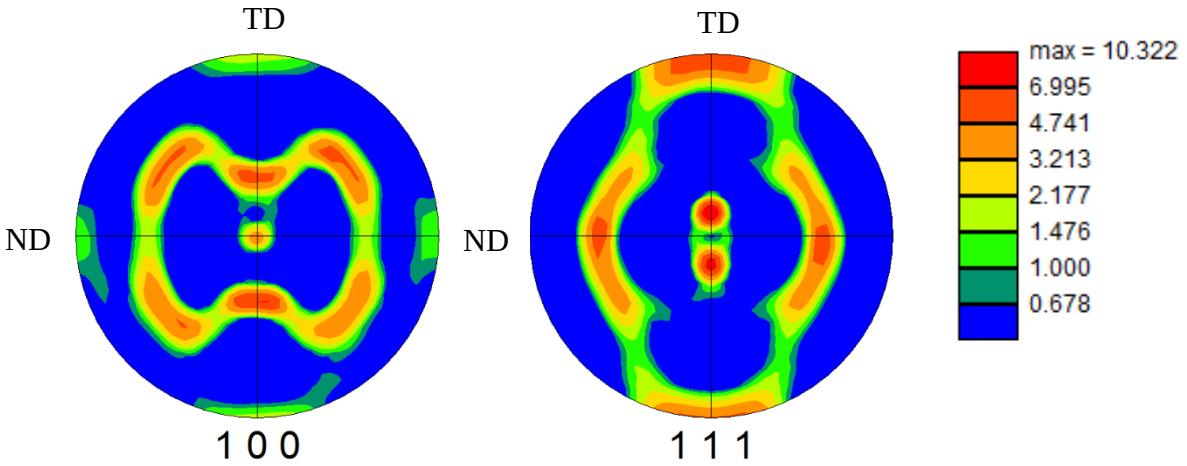

*Figure 101: (100) and (111) pole figures of **AA7108 T1** for the entire TD-ND-plane, with an intensity bar to the right.*

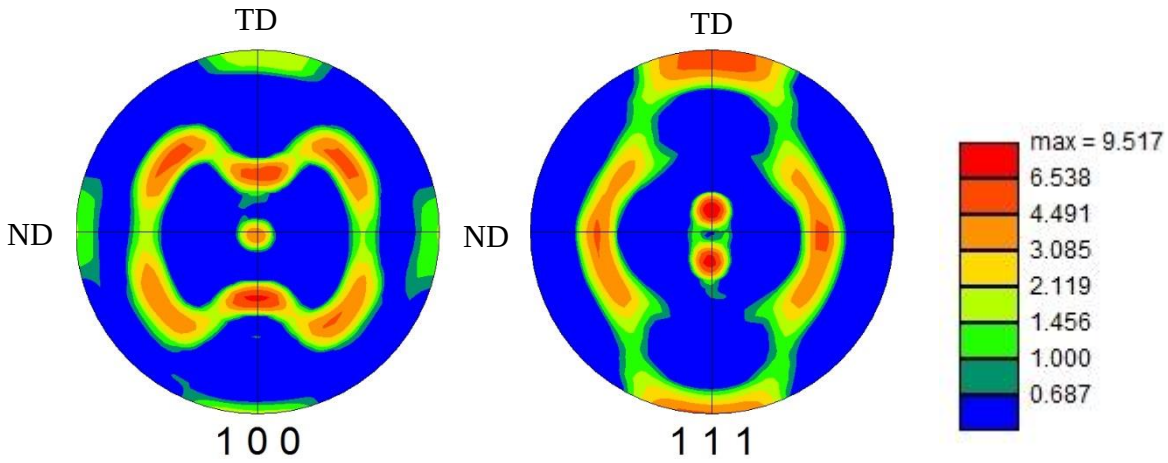

*Figure 102: (100) and (111) pole figures of **AA7108 T6** for the entire TD-ND-plane, with an intensity bar to the right.*

5 Discussion

In this chapter, the results from the experimental work will be discussed and evaluated according to established theory and published research. First, the effect of different parameters on the fatigue properties will be elucidated. Then, the fatigue properties of AA6082 and AA7108 will be discussed in terms of SN-curves, fractography and the relation to cyclic hardness change. At last, possible error sources will be accounted for.

The aim of this study was to investigate how the fatigue properties of AA6082 and AA7108 were affected by natural ageing compared to artificial ageing. Throughout the discussion this aim should be kept in mind. The AA6082 was extruded in 2001, and stored for 14 years, while the AA7108 was extruded in 2005 and stored for 10 years.

To understand how strengthening of aluminium is possible by either storage, heat treatment or both, an understanding of Fick's first law is important. Strengthening of aluminium depends on diffusion of the alloying elements. When the alloying elements diffuse and cluster together, strengthening particles are made. According to Fick's first law, the diffusion rate depends on both time and temperature. As the temperature is included in the exponential part of the law, and time is linear, an increase in temperature will be most efficient for diffusion. Never the less, if the time is large enough, diffusion will still be possible, hence strengthening of aluminium by long time storage is theoretically possible.

5.1 The effect of different parameters on fatigue

As described in the theory chapter, many parameters other than material strength can affect the fatigue strength. In this sub-chapter, several parameters that may have altered the fatigue strength will be accounted for. These parameters are important to keep in mind later on, when the fatigue properties are discussed.

The sampling direction of the fatigue specimens

The choice of having TD parallel to the specimen length was due to an initial aim of also investigate welded fatigue specimens, and compare them to not welded specimens. Due to time limitations welding was not done. Work done by N. Nanninga et al. on AA6082 [47, 48] states that there is a large difference in the fatigue life between specimens in ED and TD, but if the specimens are polished and the die lines from extrusion removed, then the direction of the specimen relative to ED does not influence the fatigue life significantly. Hence, the fatigue properties in TD can be representative for the properties in ED.

Fracture initiation point

Surface roughness is an important factor for crack initiation. For both alloys and all temper states, the surface roughness of the fatigue specimens were below 0.5μm. The work by N. Nanninga et al. [47, 48] states that when the specimens are grinded (i.e. have a low surface roughness value), the crack initiation often is due to stress concentrations, like corners. For many specimens the fracture did initiate at, or nearby a corner, indicating initiation due to a high stress concentration. On the other hand, most specimens had fracture initiation points nearby or at surface imperfections (grooves, notches), even if the initiation also was at corner. Therefore, it seems as surface roughness has affected the initiation, but it is inconclusive if it was due to cyclic surface roughening or the surface roughness before testing.

Cyclic surface roughening was observed on most fractographs of the fracture initiation point, where grooves larger than 2μm are visible on the outer surface. As the surface roughness was lower than 0.5μm before fatigue testing, these grooves could have been made during the fatigue testing. The grooves can be slip band extrusions or slip band intrusions, both of which can act as a fatigue crack initiation point.

Some of the AA6082 fatigue specimens tested at maximum stresses above the yield strength had several fatigue fractured areas. The number of fatigue fractured areas is most likely due to the higher tendency to localize plastic deformation in surface defects or corners at a maximum stress above the yield strength. Several locations on the specimen surface may therefore act as sites for crack initiation simultaneously.

Also particles or other defects in the material can work as fracture initiation points. During fatigue, the particles will have a higher stress concentration than the surrounding matrix, and therefore be favorable for crack initiation [1]. During final fracture, particles will be ripped out and pores will be left on the fractured surface. Pores were found on some of the AA6082 fractographs, and they are most likely from primary particles. The pores were evenly spread out and it is likely that they also was present at the fracture initiation point, hence that primary particles occasionally were present at the fracture initiation point and lead to fracture.

Please note that fracture initiation at, or nearby a corner does not rule out that the initiation happened due to cyclic surface roughening, a particle or the surface roughness. In this work, it is not possible to know what was the leading factor for crack initiation, and therefore all possible factors must be considered.

Recrystallized layer from extrusion

The fatigue specimens of AA6082 had a recrystallized layer from extrusion, while the recrystallized layer on the fatigue specimens of AA7108 was removed when the specimens were prepared by machining. According to the work of K. Pedersen et al. [49], fatigue crack initiation and growth are easier in specimens with a recrystallized layer, and therefore this could have affected the fatigue properties of AA6082.

It is the enlargement of the grain size in the recrystallized layer that will have a negative effect on the fatigue properties. A large grain size will lower the strength, which in turn will lower the fatigue strength (to be discussed later), but also lower the crack initiation resistance. The formation of persistent slip bands (PSB's) are easier in large grains, and therefore, crack initiation will be easier as the cracks propagate along PBS's before stage II cracking.

Recrystallization was observed in the micrograph of the AA6082 sample both solution heat treated and artificially aged. When solution heat treatment is done, the microstructure does not change during artificial ageing, because the temperature is too low. Therefore, the micrograph of AA6082 solution heat treated and artificially aged can represent both AA6082 T6 and T4.The additional grain growth, together with the presence of the recrystallized layer can therefore have a negative effect on the fatigue properties of AA6082 T4 and T6. It should be noted that the recrystallized layer on the AA6082 fatigue specimens is most likely more

narrow than on the micrographs due to grinding before fatigue testing. The recrystallized layer is not completely removed however, as can be seen on the grain maps of AA6082 from texture analysis, Figure 95 and Figure 96.

Microstructure analysis

Microstructure analysis, was carried out to provide information about the grain structure and the orientation of grains (the texture), and to investigate if the texture had a favorable orientation for slip during fatigue testing.

Texture analysis was performed in the TD-ND-plane, hence the plane normal to ED. The texture was investigated for the temper states T1 and T6. The texture will not change during artificial ageing, because the temperature is to low. Therefore, the texture of the T5 material should be the same as the texture of the T1 material, and the texture of the T4 material should be the same as the texture of the T6 material. Hence, only the T1 and T6 temper state were investigated.

For both alloys, the grain structure of the T6 temper (Figure 96 and Figure 98) is slightly altered from the T1 temper (Figure 95 and Figure 97) as expected due to the solution heat treatment. However, this did not change the texture, i.e., the texture was the same for both T1 and T6, as can be seen from the pole figures (Figure 99-Figure 102).

All (111) pole figures indicates {111} planes at an angle of approximately 45º towards TD (equivalent to the direction of load during fatigue), ED and ND. In all (111) pole figures, this is seen as the ends on the half moon shaped intensity maximums marked on Figure 99. Since the {111} planes are the slip planes of aluminium and the fact that they are oriented ~ 45º towards TD, these will be the planes with the highest Schimd factors and contribute to slip initiation. Hence, the microstructure have crystallographic planes that contributes to crack initiation and crack propagation.

The two intensity maximums in the middle of the pole figure is also {111} planes, but at an angle almost parallel (~8-10º) with TD and hence these planes will not contribute much to slip. The same goes for the intensity maximums found at the north and south poles, which are

also {111} planes, but at an angle of 90º towards TD, and therefore does not contribute to slip.

Temperature and humidity

The temperature was stable during every test and varied by the most ±1ºC. This shift in temperature during fatigue testing is too small to influence the fatigue properties[1]. The humidity was measured for most of the specimens. Due to an unstable humidity instrument, some of the specimens were fatigue tested without control of the humidity. When measured, the relative humidity varied between 10-30%. An increase in humidity will decrease the corrosion resistance, and hence lower the fatigue properties[1]. In this work, oxidation products were observed on several AA7108 specimens, and corrosion fatigue was found for one specimen, as will be evaluated in the next section.

Corrosion and cracks

AA7108 had several deviating specimens during fatigue testing. All deviating specimens failed when tested with a maximum stress which should have led to RO. On the T1 specimen, a large crack (~ 1mm) was found. Due to the size and location of the crack, it is likely that the crack was made when the specimen was machined, hence that the crack was existing before fatigue testing. The presence of such a large defect, can lower the fatigue properties and be the reason for early failure. The most deviating T4 specimen had several large (300-500μm) secondary cracks inside the fatigue fractured area. As these cracks lower the resistance against further crack propagation, they are most likely the reason for early failure. On the T5 specimen, corrosion was assumed by fractography and confirmed by EDS, as the oxygen concentration was high. An increase in humidity would increase the likelihood of corrosion, and corrosion would lower the fatigue properties. Hence, corrosion should be the reason for early failure in this case.

5.2 Fatigue properties

This sub-chapter will first deal with the general fatigue properties in terms of the SN-curves and Goodman diagrams. Then, the fatigue properties will be discussed in terms of strength, and the precipitated particles. At last, the relation to hardness change will be made.
Due to time limitations, the chosen RO for this master thesis ($2 \cdot 10^6$ cycles) is lower than the usual chosen RO of $5 \cdot 10^8$ cycles. Never the less, the results in this report will give an

indication of the RO's, and therefore an indication of the endurance limit. Normally, for aluminium, the endurance limit is approximately 1/3 (30%) of the yield strength at $5 \cdot 10^8$ cycles [32].

5.2.1 General observations of fatigue properties

AA6082

The fatigue properties of the AA6082 temper states are presented in terms of SN-curves in Figure 54. First, there is not a direct relation between the highest ultimate tensile strength and the highest fatigue strength. The T6 temper has the highest ultimate tensile strength (see Table 11), but at $5 \cdot 10^5$ cycles, the fatigue strength of the T4 temper is the highest, followed by the T1 and T5 tempers, which have approximately the same fatigue strength at $5 \cdot 10^5$ cycles. The same relationship between the different tempers and the fatigue strength applies at $2 \cdot 10^6$ cycles (RO).

Also included in Figure 54, is the yield strength of the different tempers. Even though the T1 temper has the lowest ultimate tensile strength, it is the temper state which endures the largest number of cycles, i.e. above the yield strength. Further, the T1 temper has RO closest to its yield strength, at a maximum stress of 82% of its yield strength.

The Goodman diagrams of AA6082 (Figure 57-Figure 58) also underline the good fatigue properties of the T4 and the T1 tempers, as they have the largest stress range where fatigue can be avoided at any given mean stress (or stress ratio). The T1 temper shows the largest amount of work hardening, also illustrated by the Goodman diagram.

AA7108

The fatigue properties of AA7108 tempers are displayed in terms of SN-curves in Figure 55. First, a direct relation between the ultimate tensile strength and the fatigue strength can be drawn. The T5 and T1 tempers have the highest ultimate tensile strength (see Table 11), and also tolerate the highest maximum stress at $5 \cdot 10^5$ cycles. In addition, these are the temper states with the most gradual SN-curves, and are therefore less affected by an increase in maximum stress, than the T4 and T6 tempers.

The yield strength of each temper state is also included in Figure 55. Even though the T4 temper has the lowest ultimate tensile strength, it is the only temper surviving a high number of cycles above the yield strength. The T4 temper is also the temper state that has RO closest to its yield strength, at a maximum stress of 90% of the yield strength.

As for AA6082, the Goodman diagrams of AA7108 (Figure 61-Figure 62) underlines the fatigue properties. The T1 temper state has the largest stress range where fatigue can be avoided at any given mean stress. The Goodman diagram illustrates the amount of work hardening very well, which is largest for the T4 temper state.

It should be noted that the T6 temper had six RO's, and therefore, the SN-curve is only made of four specimens. It is possible that the difference between $3 \cdot 10^5$ and $2 \cdot 10^6$ cycles (RO) is actually only 2 MPa, but it is also possible that the ageing was not even for all specimens. The reason for doubting the ageing will be further discussed in the sub-chapter regarding the relation to hardness change. Also, even though the T6 has the lowest fatigue strength at $5 \cdot 10^5$ cycles, it does not have the lowest fatigue strength at RO, this underlines that a new SN-curve of the T6 is desirable.

The two alloys compared

When comparing the two alloys it seems as the fatigue response of AA6082 is better than for AA7108. If one look carefully at the SN-curves, the points constituting the SN-curves of AA6082 are more evenly spread out between $5 \cdot 10^4$ and $2 \cdot 10^6$ cycles. Even though the fatigue test procedure was the same, it was easier to make an even curve of AA6082, as the results of AA7108 varied more. Large secondary cracks was not only found in the deviating AA7108 specimens, but also in other specimens, and they are much larger than the few observed in AA6082. The reason for the large cracks are not clear, but as AA7108 is more sensitive to the environment (e.g. humidity leading to stress corrosion cracking [50]) this could be one explanation.

5.2.2 The effect of precipitated particles

The peak hardened temper states, T5 and T6, are industrially the most used due to their high strength. Even so, the results in this thesis indicates that these tempers does not obviously have the best fatigue properties.

For both alloys, the T1 and T4 tempers have good fatigue properties, even though these are not the peak hardening temper states. The common feature of these temper states, observed in this thesis, is the ability to endure a large amount of work hardening.

As described in the theory, a large amount of work hardening indicates an ability to endure a large amount of plastic deformation before reaching the ultimate tensile strength. During fatigue, plastic deformation can start at stresses lower than the yield strength, and the ability to endure plastic deformation is therefore favorable during fatigue if cyclic hardening occurs. Work hardening of alloys hardened by heat treatment depends on the distribution and size of the precipitates and the solute level left in matrix [51]. Therefore, it is important to take closer look on the particles precipitated during ageing.

AA6082

The precipitated particles in the T1 and T4 temper state should be GP-zones formed during natural ageing in room temperature. The GP-zones are clusters of Mg and Si that diffuse together during ageing. As the hardening process of the T4 is the same as the hardening process of T1, but during less amount of time, it is reasonable to believe that the impelling power of creating hardening particles is alike. Hence, the precipitated particles in the T1 temper state should be GP-zones, but as the ageing time is longer, the formed GP-zones are most likely larger than in T4. From the ageing curves, presented in chapter 3.2.1, the peak hardness of the T1 is higher than the peak hardness of the T4. This indicates that the GP-zones in T1 and T4 are somewhat different as they influence the hardness differently.

The hardening particles in the T5 and T6 temper states should be the peak hardening particles β'' and β'. Even so, it is reason to believe that the T5 temper state also has coarse GP-zones, which formed during storage and did not dissolve in the beginning of the artificial ageing process. The presence of undissolved GP-zones lower the peak hardness, as can be seen on the artificial ageing curve (Figure 36).

During work hardening, dislocations move through the matrix and interact with the precipitated particles. This interaction will provide a strength contribution as described in the theory. To ensure an efficient work hardening, the particles must not restrict the dislocation

movement too much, and it seems as the GP-zones in AA6082 are ideal, especially in the T1 temper state. Hence, the GP-zones provides a larger resistance against fatigue failure. Note that the three temper states in AA6082, the T1, T4 and T5, with the best fatigue properties, all should have GP-zones.

AA7108

As for AA6082, the assumed hardening particles in AA7108 T1 and T4 are GP-zones formed during natural ageing in room temperature. The GP-zones are clusters of Mg and Zn that diffuse together during ageing. The GP-zones of T1 are most likely larger due to the longer ageing time. From the ageing curves, presented in chapter 3.2.1, the peak hardness of the T1 is higher than the peak hardness of the T4. This indicates that the GP-zones in T1 and T4 are somewhat different.

The hardening particles present in the T5 and T6 tempers should be the peak hardening particle η'. It is possible that the T5 temper also contains some undissolved GP-zones formed during storage, even as the T5 temper underwent a two step artificial ageing process. The artificial ageing curves (Figure 38), show that the peak hardness of the T5 is higher than the peak hardness of the T6 temper, indicating that the precipitated particle are somewhat different in size and distribution. This difference could be the presence of GP-zones in addition to η' in T5, even though η' alone theoretically provides peak strength.

As for AA6082, it seems as the GP-zones in AA7108 T1 and T4 also are ideal for work hardening and hence provides a large resistance against fatigue. The T5 temper state also has good fatigue properties, and if present, the GP-zones may have had an influence on that.

The relationship to fractography

The difference between the alloys and tempers can be seen on the fractographs as the stage II crack growth mechanisms are somewhat different. According to theory, fatigue fractures should have a transgranular stage II crack propagation.

All AA6082 tempers had a transgranular stage II crack growth, where some specimens had additional elements of slip localized growth. Both the AA6082 T1- and T4 temper with the shortest fatigue life had a larger degree of slip localized growth, seen as slip bands on the

fractographs. Slip localized growth was also found in some degree for AA6082 T5, and T1- and T4 with the longest fatigue life.

In difference to AA6082, the stage II crack propagation of AA7108 seems more slip dominated, however, most specimens had transgranular growth in addition to slip localized growth. The AA7108 T1 temper seems to have a very slip dominated growth.

The differences in the stage II growth mechanisms can be due to the precipitates formed during ageing. For both alloys, the tempers with slip localized growth was also the tempers where GP-zones were the assumed ageing precipitate. The GP-zones are shearable, i.e. they can make slip localized growth easier. The crystallographic texture can also explain the slip localized growth, as the {111} planes are in a favorable orientation for slip.

Secondary GB-cracking was observed on one AA6082 specimen, T1 with the shortest fatigue life, while it seems common for all AA7108 tempers, where it was observed in a different degree on all AA7108 fractographs. Crack propagation along the grain boundaries are favorable if e.g. precipitate free zones (PFZ's) exists. PFZ's are zones around the grain boundaries without precipitates and are therefore weaker than the surrounding matrix. Weaker areas are favorable for crack propagation due to stress localization, and hence they can be the reason for this type of crack propagation. Both AA6082 and AA7108 are prone to formation of PFZ's [4], which can made during ageing by a solute depletion mechanism [52, 53].

5.2.3 The relation to hardness change during fatigue

AA6082

The T1 temper state undergoes cyclic hardening at most maximum stresses (except the stresses leading to RO) and also endures the largest amount of work hardening. The T4 temper state, has the second largest amount of work hardening, and undergoes cyclic hardening mainly at high maximum stresses. The T5 and T6 temper states undergo cyclic softening. Hence, there seems to be a relation between the amount of work hardening and the hardness change during cyclic loading.

In the work done by K. Pedersen [54], cyclic hardening happens due to the formation of high density dislocation loops. The formation of high density dislocation loops during cyclic

hardening is also supported by S. Suresh [33] and by the great amount of work hardening, indicating storage of dislocations [19]. The cyclic hardening of the T1 and T4 temper states can therefore be due to formation of dislocation loops and accumulation of dislocations.

In the same work [54] , cyclic softening happens due to the formation of persistent slip bands when the material was recrystallized and aged to peak hardness (T6). The softening of the T6 temper is therefore in accordance with K. Pedersen's work, and formation of PBS's in T6 can be assumed. Formation of PBS's is the main reason for cyclic softening [33]. If the grooves seen on the outer surface on the fractographs, are slip band extrusions or intrusions, hence PSB's, then the grooves underlines the assumption of cyclic softening in T5 and T6 due to PSB's.

AA7108

For AA7108, only the T4 temper states undergo cyclic hardening, this is also the temper state with the largest amount of work hardening. The same argument made for AA6082 can be made for AA7108: cyclic hardening during fatigue involves formation of high density dislocation loops [33], which also promotes a large amount of work hardening [19] and storage of dislocations.

The T5 and T1 temper state undergo cyclic softening during fatigue testing and as for AA6082, cyclic softening happens due to formation persistent slip bands, or if the strengthening particles are coherent or easily sheared, as stated by S. Suresh [33]. In difference of AA6082, the GP-zones in AA7108 are coherent, which can promote cyclic softening. The presence of GP-zones in T1 and T5 (if any) may therefore cause cyclic softening, even though the T4 temper experienced cyclic hardening. It seems as the T4's ability to work harden might over rule the coherency of the GP-zones. Never the less, as for AA6082, the formation of PSB's as the cause of cyclic softening of T1 and T5, is also a possibility.

There is no clear relationship between fatigue and the change in hardness for the T6 temper state, as the hardness after fatigue testing is both lower and higher than the hardness before fatigue testing. The variation in hardness after fatigue testing can be due to an uneven

temperature in the oil bath because several specimens were heat treated at the same time. This would also affect the ageing process and hence the fatigue properties.

5.3 The final remark: Error sources

During laboratory work there will always be possible error sources. It is important to pay attention to these possible error sources without undermining the work done. This small section will elucidate some of the possible error sources in this thesis.

In order to strengthen the alloys in this master's thesis, different kinds of ageing treatments were done. The specimens were aged at specific temperatures in oil baths, salt baths and a muffle furnace. It is possible that the temperature in these furnaces were not 100% stable due to several specimens in the furnace at the same time, which could affect the ageing assumed in this thesis. As the hardness of the fatigue specimens are generally alike for specimens of the same alloy and in the same temper state before fatigue testing, it seems as the precipitation has been successful. Never the less, as the hardness was not measured on every fatigue specimen, this might be a source of error.

Hardness measurements can also provide error sources such as drawn out hardness indentions or faults in the machine causing the wrong weight on the indention. In fact drawn out hardness indentations were sometimes observed. These are most likely due to unleveled specimens and could have affected the average hardness value.

Error sources arising during fatigue testing are also possible. As all fatigue specimens were manually inserted in the test machine, there is a possibility that they were inserted slightly unaligned. Unaligned specimens will experience an uneven stress distribution during fatigue, which could affect the local resolved shear stress and hence the fatigue behaviour. Fatigue tested specimens with uneven gripping marks were also observed, hence the gripping force had been uneven. An uneven gripping force will lead to an altered stress distribution during fatigue testing, and the cause of spread in data related to this.

At last, this discussion will be rounded off by a paying a quick attention to the statistical nature on fatigue. As stated by G. E. Dieter [1], fatigue life and the fatigue limit are statistical quantities and therefore there will be variations in the fatigue results. To ensure the fatigue

properties, a large number of specimens should be tested, and it must be kept in mind that each fatigue specimen will have its own fatigue limit. Therefore, the statistical nature of fatigue will always be an underlying reason for fatigue behavior.

6 Conclusions

The effects of natural ageing compared to artificial ageing on fatigue properties of extruded AA6082 and AA7108 have been investigated. Both alloys were tested under one-axial cyclic stress in the direction transverse to the extrusion direction and in the temper states T1, T4, T5 and T6. The testing was done at R=0.1, and the tests were stopped at $2 \cdot 10^6$ (RO). The fractured surfaces, grain structures and texture were investigated by SEM. The change in hardness upon cyclic deformation and surface roughness were quantities also investigated and discussed.

- The fatigue properties are better for both alloys when naturally aged instead of artificially aged.

- For AA6082, the T4 temper state has the best fatigue properties, i.e. a combination of high fatigue strength at $5 \cdot 10^5$ cycles, and RO close to its yield strength. Hence, the strengthening particles formed during natural ageing, the GP-zones, seem to have the most positive effect on the fatigue properties. The T6 temper has the poorest fatigue properties, even though it has the highest ultimate tensile strength for AA6082. Here, the T4 temper state has the second highest ultimate tensile strength.

- For AA7108, the T1 temper state has the best fatigue properties, i.e. seen by the high fatigue strength at $5 \cdot 10^5$ cycles, and RO close to the yield strength. Hence, the strengthening particles formed during storage, the GP-zones, seem to have the most positive influence on fatigue properties. The T6 temper state has the poorest fatigue properties, and only the third highest ultimate tensile strength for AA7108. The T1 temper state has the highest ultimate tensile strength of AA7108.

- High tensile properties and good fatigue properties seems to be related, but when that relationship fails, the reason for good fatigue properties can be due to the ability to work harden.

- The fatigue response of AA6082 is better than for AA7108 as the behavior of AA6082 is more predictable (the number cycles increases as the maximum stress decreases). The reason for this difference might be the higher sensitivity to environment of AA7108, e.g. influence of air humidity on corrosion fatigue.

- Further work should include:

  - TEM images of the strengthening particles formed during storage to decide their shape, size and distribution.

  - An analysis of the primary particles in AA6082. These particles are likely to govern ductile dimple growth characteristics.

  - Due to several (six) RO's and inconclusive hardness measurements of AA7108 T6, this temper state could be tested under fatigue loading condition once more to assure reliability.

  - The presence of precipitate free zones (PFZ) should be investigated by TEM, as both alloys are prone to form PFZ and the work by K. Pedersen [55] on the influence of PFZ's on the fatigue life properties.

7 References

1. Dieter, G.E., *Fatigue Of Metals*, in *Mechanical Metallurgy*. 1988, McGraw-Hill Book Company (UK) limited. p. 375-431.
2. Schütz, W., *A history of fatigue.* Engineering Fracture Mechanics, 1996. **54**(2): p. 263-300.
3. Supple, W.J., *The 'Alexander L. Kielland' Accident: Norwegian Public Reports NOU 1981:11 Global Book Resources Ltd (1981) £12.80 Commission appointed by Royal Decree 28th March 1980; report presented to Ministry of Justice and Police March 1981*. International Journal of Fatigue, 1983. **5**(1): p. 50.
4. Solberg, J.K., *Aluminium og aluminiumslegeringer*, in *Teknologiske metaller og legeringer*. 2011, Institutt for materialteknologi, NTNU. p. 182-232.
5. Grong, Ø., *Sveisemetallurgi*. 1990, Metallurgisk institutt, NTH.
6. Sha, G. and A. Cerezo, *Early-stage precipitation in Al–Zn–Mg–Cu alloy (7050).* Acta Materialia, 2004. **52**(15): p. 4503-4516.
7. Li, X., et al., *HREM study and structure modeling of the< i> η</i>' phase, the hardening precipitates in commercial Al–Zn–Mg alloys.* Acta materialia, 1999. **47**(9): p. 2651-2659.
8. Hydro. *Physical properties*. 2014 04.11.14]; Available from: http://www.hydro.com/en/About-aluminium/Why-aluminium/Physical-properties/.
9. Hydro. *Recycling of aluminium*. 2014 04.11.14]; Available from: http://www.hydro.com/en/About-aluminium/Aluminium-life-cycle/Recycling/.
10. Mathers, G., *The welding of aluminium and its alloys*. 2002: Woodhead Publishing Ltd, CRC Press LLC
11. King, F., *Properties of Aluminium alloys*, in *Aluminium and its alloys*. 1987, Ellis Horwood Limited. p. 140-159.
12. aluMatter. *Intergranular Corrosion of Aluminium I*. 2015; Available from: http://aluminium.matter.org.uk/content/html/eng/default.asp?catid=180&pageid=2144416695.
13. aluMatter. *7xxx Series Alloys*. 2015; Available from: http://aluminium.matter.org.uk/content/html/eng/default.asp?catid=214&pageid=2144417086.
14. Reiso, O., *Extrusion of AlMgSi Alloys.* Materials Forum, 2004. **28**.
15. Hydro. *How it's made*. 2014; Available from: http://www.hydro.com/en/About-aluminium/How-its-made/.
16. Dieter, G.E., *Extrusion*, in *Mechanical Metallurgy* 1988, McGraw-Hill Book Company (UK) Limited. p. 616-634.
17. Dieter, G.E., *The Tension Test*, in *Mechanical Metallurgy*. 1988, McGraw-Hill Book Company (UK) Limited. p. 275-324.
18. Dieter, G.E., *Plastic Deformation of Single Crystals*, in *Mechanical Metallurgy*. 1988, McGraw-Hill Book Company (UK) Limited.
19. Dieter, G.E., *Dislocation Theory*, in *Mechanical Metallurgy*. 1988, McGraw-Hill Book Company (UK) Limited.
20. aluMatter. *7xxx Series Alloys*. 2014; Available from: http://aluminium.matter.org.uk/content/html/eng/default.asp?catid=214&pageid=2144417086.

21. aluMatter. *6xxx Series Alloys*. 2014; Available from: http://aluminium.matter.org.uk/content/html/eng/default.asp?catid=214&pageid=2144417085.
22. Callister, W.D.J., *Precipitation hardening*, in *Materials Science and Engineering an Introduction*. 2007, John Wiley & Sons Inc p. 402-407.
23. Dieter, G.E., *Strengthenig Mechanisms*, in *Mechanical Metallurgy*. 1988, McGraw-Hill Book Company (UK) Limited. p. 184-240.
24. Westermann, I., *Conversation*. 2014.
25. Holmedal, B., *Lecture notes TMT4222 (not published)*. 2013, Institutt for Materialteknologi, NTNU.
26. Marioara, C., et al., *The influence of temperature and storage time at RT on nucleation of the β "phase in a 6082 Al–Mg–Si alloy.* Acta Materialia, 2003. **51**(3): p. 789-796.
27. Mrówka-Nowotnik, G., *Influence of chemical composition variation and heat treatment on microstructure and mechanical properties of 6xxx alloys.* Archives of materials science and engineering, 2010. **46**(2): p. 98-107.
28. Hayoune, A., *Thermal Analysis of the Impact of RT Storage Time on the Strengthening of an Al-Mg-Si Alloy.* Materials Sciences and Applications, 2012. **3**: p. 460.
29. Waterloo, G., et al., *Effect of predeformation and preaging at room temperature in Al–Zn–Mg–(Cu, Zr) alloys.* Materials Science and Engineering: A, 2001. **303**(1): p. 226-233.
30. Almar-Næss, A., *Utmatting og utmattingsprøving*, in *Metalliske materialer*. 1981, Tapir Forlag. p. 179-200.
31. Callister, W.D.J., *Failure*, in *Materials Science and Engineering an Introduction*. 2007, John Wiley & Sons Inc. p. 227-237.
32. Roven, H.J., *Personal Communication*. 2015.
33. Suresh, S., *Cyclic deformation in polycrystalline ductile solids*, in *Fatigue of Materials*. 1998, Press Syndicate of the University of Cambridge.
34. Sahoo, P., *Engineering Surfaces - Properties and Measurements*, in *Engineering Tribology*. 2005, Prentice-Hall of India Private Limited. p. 12.
35. Hjelen, J., *Scanning elektron-mikroskopi*. 1989: Metallurgisk institutt NTH.
36. Dieter, G.E., *Fracture*, in *Mechanical Metallurgy*. 1988, McGraw-Hill Book Company (UK) Limited.
37. Metals, K.t. *Macroscopic Aspects of Fracture*. 2014 [cited 2014; Available from: http://steel.keytometals.com/Articles/Art154.htm.
38. Ashby, M.F. and D.R.H. Jones, *Fatigue failure*, in *Engineering Materials 1*. 2005, Elsevier.
39. Bolton, W., *Engineering materials technology*. 2013: Elsevier.
40. Callister, W.D.J., *Hardness*, in *Materials Science and Engineering an Introduction*. 2007, John Wiley & Sons, Inc. p. 155-160.
41. Verlinden, B., et al., *Thermo-mechanical processing of metallic materials*. Vol. 11. 2007: Elsevier.
42. Randle, V. and O. Engler, *Introduction to texture analysis: macrotexture, microtexture and orientation mapping*. 2000: CRC Press.
43. Schwarzer, R.A., et al., *Present state of electron backscatter diffraction and prospective developments*, in *Electron backscatter diffraction in materials science*. 2009, Springer. p. 1-20.
44. Utne, S.C., *Fatigue of welded AA6082 Alloys - Effects of PWHT and Shot Peening*. 2013, IMTE, NTNU: Master's Thesis.

45. Furu, T. and A. Clausen, *Strain Rate Sensitivity in som Heat Teatable Aluminium Alloys in T6 and T7 Conditions*. 2005, Hydro Aluminium R&D Materials Technology.
46. Designation, A. *E466-07, Standard practice for conducting force controlled constant amplitude axial fatigue tests of metallic materials*. 2007. ASTM.
47. Nanninga, N. and C. White, *The relationship between extrusion die line roughness and high cycle fatigue life of an AA6082 alloy.* International Journal of Fatigue, 2009. **31**(7): p. 1215-1224.
48. Nanninga, N., et al., *Effect of orientation and extrusion welds on the fatigue life of an Al–Mg–Si–Mn alloy.* International Journal of Fatigue, 2008. **30**(9): p. 1569-1578.
49. Pedersen, K., O. Helgeland, and O. Lohne. *The effect of grain structure on fatigue life of age hardening aluminium alloys*. in *ECF4, Leoben 1982*. 1982.
50. Ghali, E., *Corrosion resistance of aluminum and magnesium alloys: understanding, performance, and testing*. Vol. 12. 2010: John Wiley & Sons.
51. Friis, J., et al. *Work hardening behaviour of heat-treatable Al-Mg-Si-alloys*. in *Materials science forum*. 2006. Trans Tech Publ.
52. Jha, S., T. Sanders, and M. Dayananda, *Grain boundary precipitate free zones in Al-Li alloys.* Acta Metallurgica, 1987. **35**(2): p. 473-482.
53. Raj, B., *Frontiers in Materials Science*. 2005: Universities Press.
54. Pedersen, K., *Cyclic deformation of an extruded AlMgSi alloy.* Virginia Univ, Fatigue 87, 1987. **1**.
55. Pedersen, K. *Fatigue mechanism in an AlMgSi alloy*. in *Fourth international conference on fatigue and fatigue thresholds*. 1990.

Appendix A – Fatigue test data

The fatigue test data are presented below. The fatigue tests were manually stopped at $2 \cdot 10^6$ cycles, so-called redeemed run-outs (RO), due to the aim of investigating fatigue properties between 10^5 and 10^6 cycles.

Fatigue test data of AA6082

Table 23: Fatigue test data for AA6082 T1

Specimen number	**Stress amplitude [MPa]**	**Maximum stress [MPa]**	**Mean stress [MPa]**	**Area [mm^2]**	**Cycles to failure**
1	45	100	55	15.69	RO
2	67.5	150	82.5	16.59	915777
3	72.	160	88	15.42	504334
4	76.5	170	93.5	15.39	226895
5	78.75	175	96.25	15.36	265798
6	83.25	185	101.75	15.33	190236
7	69.75	155	85.25	15.56	1042688
8	87.75	195	107.25	15.65	143441
9	74.25	165	90.75	14.93	353622
10	63	140	77	14.87	RO

Table 24: Fatigue test data for AA6082 T4

Specimen number	**Stress amplitude [MPa]**	**Maximum stress [MPa]**	**Mean stress [MPa]**	**Area [mm^2]**	**Cycles to failure**
1	103.5	230	126.5	15.58	119682
2	90	200	110	15.11	251134
3	81	180	99	15.76	RO
4	87.75	195	107.25	14.99	303397
5	85.5	190	104.5	16.05	251312
6	83.25	185	101.75	16.24	660031
7	110.25	245	134.75	16.37	56750
8	83.25	185	101.75	14.77	569138

Table 25: Fatigue test data for AA6082 T5

Specimen number	**Stress amplitude [MPa]**	**Maximum stress [MPa]**	**Mean stress [MPa]**	**Area [mm^2]**	**Cycles to failure**
1	72	160	88	16.79	206919
2	45	100	55	16.67	RO
3	58.5	130	71.5	16.45	RO
4	67.5	150	82.5	16.67	1452522
5	70.2	156	85.8	16.03	774112
6	71.1	158	86.9	16.55	319216
7	78.75	175	96.25	16.46	355442
8	87.75	195	107.25	16.82	183022
9	62.25	145	79.75	16.56	722835

Table 26: Fatigue test data for AA6082 T6

Specimen number	Stress amplitude [MPa]	Maximum stress [MPa]	Mean stress [MPa]	Area [mm^2]	Cycles to failure
1	157.5	350	192.5	15.16	5873
2	135	300	165	15.26	19940
3	90	200	110	15.08	86594
4	54	120	66	15.37	RO
5	67.5	150	82.5	15.27	216938
6	58.5	130	71.5	15.28	491299
7	56.25	125	68.75	15.25	903627
8	57.38	127.5	70.12	15.43	1845861
9	58.05	129	70.95	15.33	413218

Fatigue test data of AA7108

Table 27: Fatigue test data for AA7108 T1

Specimen number	Stress amplitude [MPa]	Maximum stress [MPa]	Mean stress [MPa]	Area [mm^2]	Cycles to failure
1	103.5	230	126.5	17.54	RO
2	126	280	154	17.54	277743
3	117	260	143	17.85	289353
4	112.5	250	137.5	17.66	RO
5	114.8	255	140.3	18.06	240204
6	115.2	256	140.8	17.85	RO
7	116.1	258	141.9	17.72	343724
8	115.7	257	141.4	17.78	1514470
9	128.7	286	157.3	17.93	267652
10	115.2	256	140.8	18.02	RO

Table 28: Fatigue test data for AA7108 T4.

Specimen number	**Stress amplitude [MPa]**	**Maximum stress [MPa]**	**Mean stress [MPa]**	**Area [mm^2]**	**Cycles to failure**
1	90	200	110	18.15	438645
2	76.5	170	93.5	17.90	RO
3	94.5	210	115.5	17.97	626388
4	103.5	230	126.5	18.03	395545
5	112.5	250	137.5	17.54	123917
6	85.5	190	104.5	17.60	RO
7	89.1	198	108.9	17.94	RO
8	92.25	205	112.75	17.84	485223

Table 29: Fatigue test data for AA7108 T5

Specimen number	**Stress amplitude [MPa]**	**Maximum stress [MPa]**	**Mean stress [MPa]**	**Area [mm^2]**	**Cycles to failure**
1	112.5	250	137.5	18.10	739334
2	135	300	165	17.93	286926
3	123.8	275	151.3	17.84	1258316
4	144	320	176	17.75	92802
5	108	240	132	17.72	RO
6	130.5	290	160	17.78	1047127
7	132.8	295	162.3	18.1	166258
8	131.4	292	160.6	17.82	718264
9	132.1	293.5	161.4	18.10	386967

Table 30: Fatigue test data for AA7108 T6.

Specimen number	**Stress amplitude [MPa]**	**Maximum stress [MPa]**	**Mean stress [MPa]**	**Area [mm^2]**	**Cycles to failure**
1	139.5	310	170.5	18.06	124771
2	117	260	143	18.36	198568
3	130.5	290	159.5	17.94	151808
4	103.5	230	126.5	18.00	288042
5	67.5	150	82.5	18.2	RO
6	76.5	170	93.5	17.79	RO
7	85.5	190	104.5	17.84	RO
8	94.5	210	115.5	17.79	RO
9	99	220	121	17.84	RO
10	102.5	227	124.85	17.90	RO

Appendix B – Hardness of fatigue specimens

The hardness was measured on two arbitrary fatigue specimens before fatigue testing and on all fatigue specimens after fatigue testing. The results are included in this appendix, first AA6082 and then AA7108. High standard deviations can be due to unleveled specimens. It can also be due to deviation in the hardness measurement apparatus.

Hardness of AA6082 fatigue specimens

Table 31: The hardness of AA6082 T1 before fatigue testing.

Arbitrary T1 specimen	Hardness [HV1]	Standard deviation
Number 1	84.42	2.26
Number 2	83.72	2.95

Table 32: The hardness of the AA6082 T1 fatigue specimens after fatigue testing.

Specimen number	Average hardness [HV1]	Standard deviation	Number of cycles	Maximum stress [MPa]
1	81.45	1.96	RO	100
2	90.30	3.67	915777	150
3	84.04	4.89	504334	160
4	88.77	2.23	226895	170
5	84.30	2.62	265798	175
6	86.65	2.95	190236	185
7	85.48	2.24	1042688	155
8	87.18	4.52	143441	195
9	85.95	1.30	353622	165
10	83.03	1.67	RO	140

Table 33: The hardness of AA6082 T6 before fatigue testing.

Arbitrary T6 specimen	Hardness [HV1]	Standard deviation
Number 1	129.18	3.28
Number 2	129.9	1.58

Table 34: The hardness of the AA6082 T6 fatigue specimens after fatigue testing.

Specimen number	Average hardness [HV1]	Standard deviation	Number of cycles	Maximum stress [MPa]
1	124.15	2.71	5873	350
2	125.83	3.24	19940	300
3	120.78	4.52	86594	200
4	125.13	3.97	RO	120
5	126.90	1.84	216938	150
6	127.95	1.89	491299	130
7	127.73	1.62	903627	125
8	127.65	1.06	1845861	127.5
9	127.32	3.25	413218	129

Table 35: The hardness of AA6082 T4 before fatigue testing.

Arbitrary T4 specimen	Hardness [HV1]	Standard deviation
Number 1	99.82	2.69
Number 2	98.37	2.23

Table 36: The hardness of the AA6082 T4 fatigue specimens after fatigue testing.

Specimen number	Average hardness [HV1]	Standard deviation	Number of cycles	Maximum stress [MPa]
1	105.08	1.93	119682	230
2	191.35	10.06	251134	200
3	99.10	3.46	RO	180
4	98.83	4.30	303397	195
5	98.60	4.53	251312	190
6	99.24	4.98	660031	185
7	104.52	3.67	56750	245
8	100.64	3.58	569138	185

Table 37: The hardness of AA6082 T5 before fatigue testing.

Arbitrary T5 specimen	Hardness [HV1]	Standard deviation
Number 1	104.5	2.01
Number 2	106.25	2.54

Table 38: The hardness of the AA6082 T5 fatigue specimens after fatigue testing.

Specimen number	Average hardness [HV1]	Standard deviation	Number of cycles	Maximum stress [MPa]
1	102.62	5.13	206919	160
2	104.43	3.52	RO	100
3	105.32	4.22	RO	130
4	102.15	2.59	1452522	150
5	101.57	2.60	774112	156
6	100.63	3.64	319216	158
7	102.52	2.29	355442	175
8	103.67	3.88	183022	195
9	105.78	2.21	722835	145

Hardness of AA7108 fatigue specimens

Table 39: The hardness of AA7108 T1 before fatigue testing.

Arbitrary T1 specimen	Hardness [HV1]	Standard deviation
Number 1	137.73	3.87
Number 2	147.83	4.88

Table 40: The hardness of the AA7108 T1 fatigue specimens after fatigue testing.

Specimen number	Average hardness [HV1]	Standard deviation	Number of cycles	Maximum stress [Mpa]
1	139.9	7.0	RO	230
2	125.4	6.4	277 743	280
3	147.2	5.3	289 353	260
4	140.2	7.1	RO	250
5	146.3	5.7	240 204	255
6	150.5	3.3	RO	256
7	146.3	1.9	343 724	258
8	134.5	8.9	1 514 470	257
9	149.5	6.3	267 652	286
10	138.4	7.7	RO	256

Table 41: The hardness of AA7108 T4 before fatigue testing.

Arbitrary T4 specimen	Hardness [HV1]	Standard deviation
Number 1	104.32	3.27
Number 2	104.70	2.79

Table 42: The hardness of the AA7108 T4 fatigue specimens after fatigue testing.

Specimen number	Average hardness [HV1]	Standard deviation	Number of cycles	Maximum stress [MPa]
1	105.07	5.35	438645	200
2	108.72	4.22	RO	170
3	109.67	6.99	626388	210
4	113.27	3.84	395545	230
5	109.65	3.20	123917	250
6	108.86	1.28	RO	190
7	109.92	1.37	RO	198
8	107.70	3.24	485223	205

Table 43: The hardness of AA7108 T5 before fatigue testing.

Arbitrary T5 specimen	Hardness [HV1]	Standard deviation
Number 1	125.4	2.17
Number 2	126.15	2.32

Table 44: The hardness of the AA7108 T5 fatigue specimens after fatigue testing.

Specimen number	Average hardness [HV1]	Standard deviation	Number of cycles	Maximum stress [Mpa]
1	123.7	4.6	739 334	250
2	122.7	4.1	286 926	300
3	123.4	3.3	1 258 316	275
4	126.9	4.4	92 802	320
5	126.35	4.8	RO	240
6	123.0	3.4	1 047 127	290
7	121.6	3.4	166 258	295
8	120.7	3.8	718 264	292
9	120	3.8	386 967	293.5

Table 45: The hardness of AA7108 T6 before fatigue testing.

Arbitrary T6 specimen	Hardness [HV1]	Standard deviation
Number 1	122.74	5.86
Number 2	116.35	3.03

Table 46: The hardness of the AA7108 T6 fatigue specimens after fatigue testing.

Specimen number	Average hardness [HV1]	Standard deviation	Number of cycles	Maximum stress [Mpa]
1	115.03	3.25	124771	310
2	114.9	4.29	198568	260
3	116.63	5.41	151808	290
4	121.95	5.30	288042	230
5	126.85	3.07	RO	150
6	121.18	2.67	RO	170
7	131.87	2.34	RO	190
8	126.72	5.34	RO	210
9	115.10	3.32	RO	220
10	127.07	12.24	RO	227

Appendix C - Fractography

Fractographs were taken on selected specimens from each SN-curve, hence from each temper state of each alloy. For each curve, fractographs were taken from the specimen with the longest fatigue life before RO, the specimen with the shortest fatigue life and, if any, the most deviating specimen. For the specimens with the longest and shortest fatigue life, crack initiation, crack growth and the final fracture will be presented. The most deviating specimens will not be presented here as they were presented in chapter 4.5.

A coordinate system, indicating ND and ED, will be placed on the first image of each specimen. The orientation of this coordinate system is valid for every image of the specimen.

Fractography of AA6082

The AA6082 T1 specimen with the longest fatigue life

The AA6082 T1 specimen with the longest fatigue life before RO endured $1.04 \cdot 10^6$ cycles before failure. Figure 103 shows an overview of the fractured surface. The red line encloses the fatigue fractured area. The numbers 1-3 is the fracture initiation point, the fatigue growth area and the final fracture, respectively. The number 1-3 are shown below in Figure 104-Figure 106.

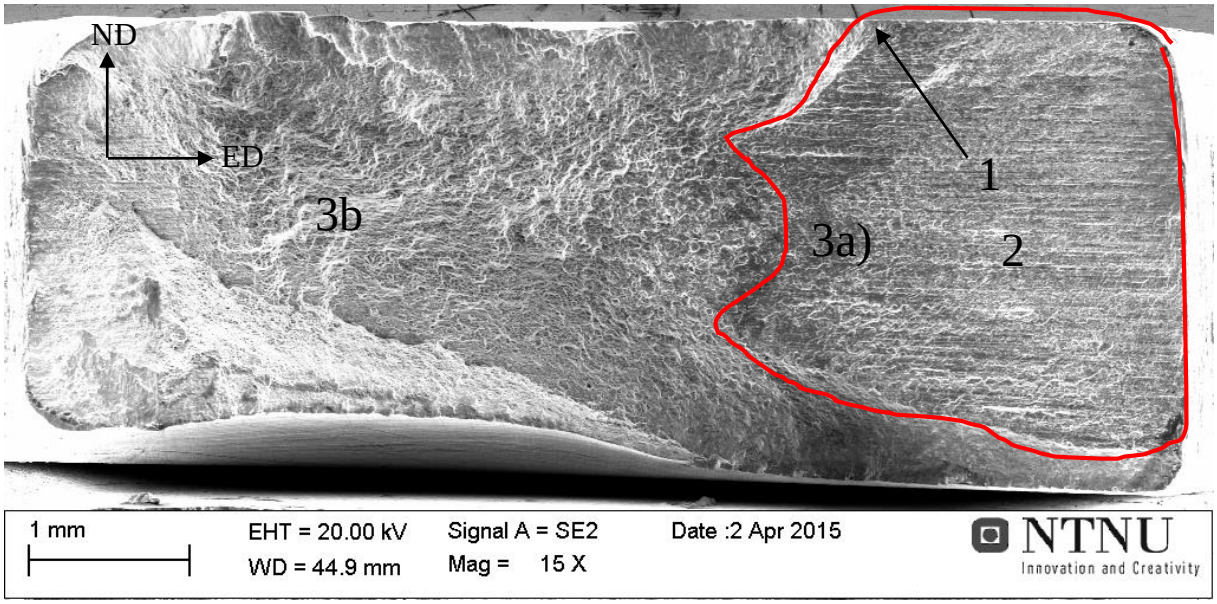

Figure 103: An overview of the fractured surface of AA6082 T1 with the longest fatigue life, 15X magnification. The fatigue fractured area is enclosed by the red line.

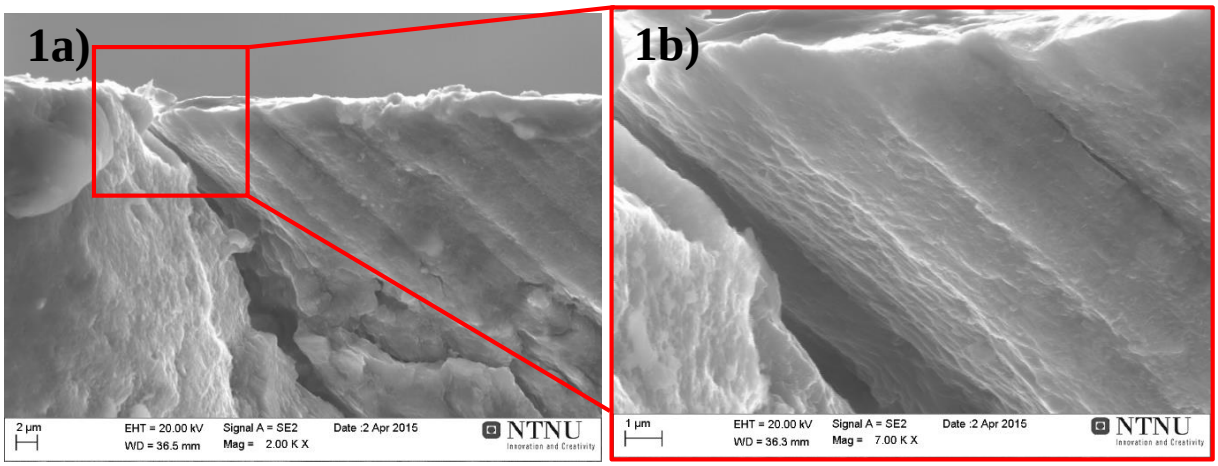

Figure 104: 1a) One possible initiation point due to intersection slip bands, with 2000X magnification, note the large secondary crack, and 1b) slip bands with 7000X magnification.

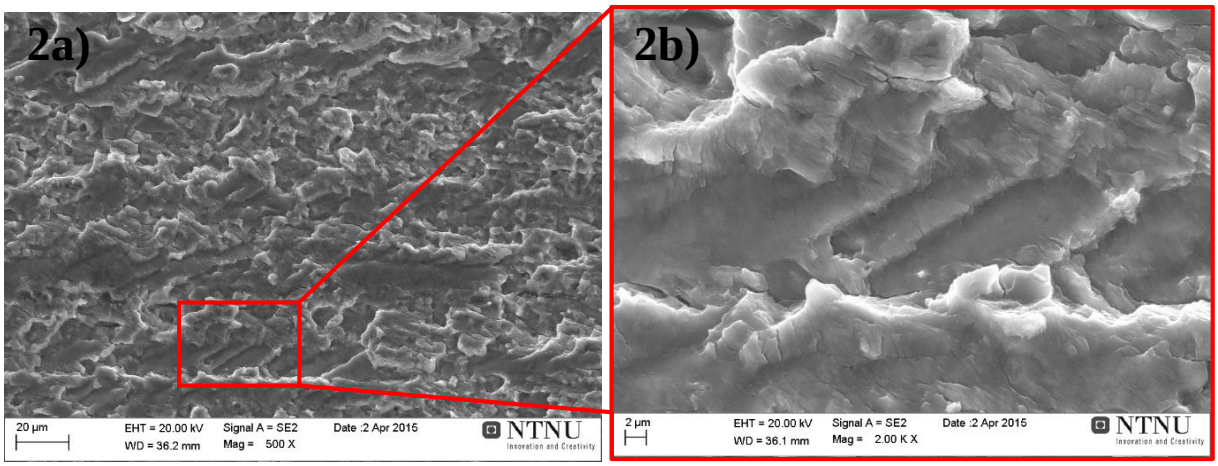

Figure 105: 2a) Transgranular crack propagation, with 500X magnification, and 2b) slip bands with short striations, with 2000X magnification.

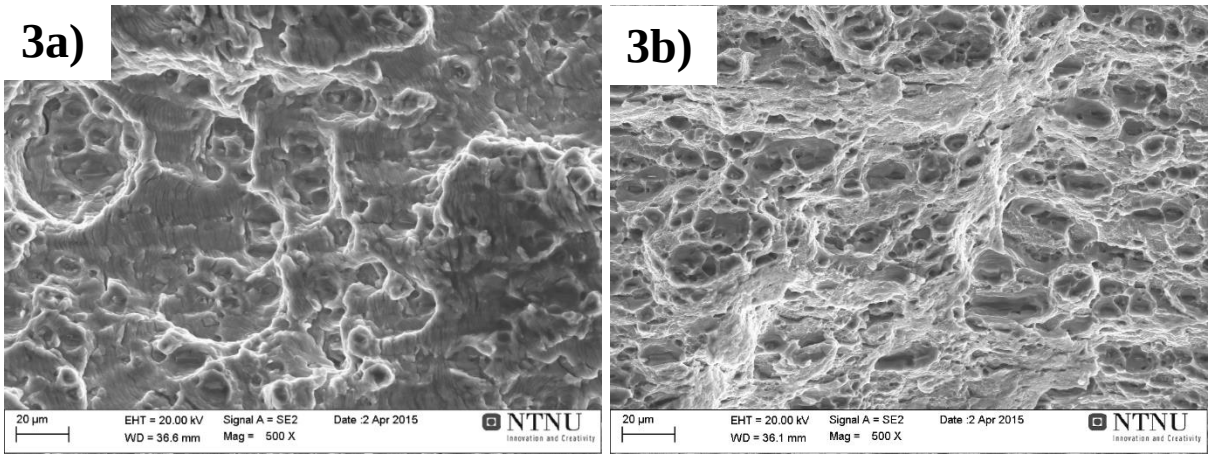

Figure 106: 3a) The transition area from fatigue crack propagation to the final fracture. 3b) The final fracture a mixed mode with both shear and dimples, both at 500X magnification.

The AA6082 T1 specimen with the shortest fatigue life

The AA6082 T1 specimen with the shortest fatigue life, endured $1.43 \cdot 10^5$ cycles before failure. Figure 107 shows an overview of the fractured surface. The red lines encloses the fatigue fractured areas. The numbers 1-3 is the fracture initiation point, the fatigue growth area and the final fracture, respectively. The number 1-2 are shown below in Figure 108 and Figure 109. The final fracture was the same as for the specimen with the longest fatigue life (Figure 106).

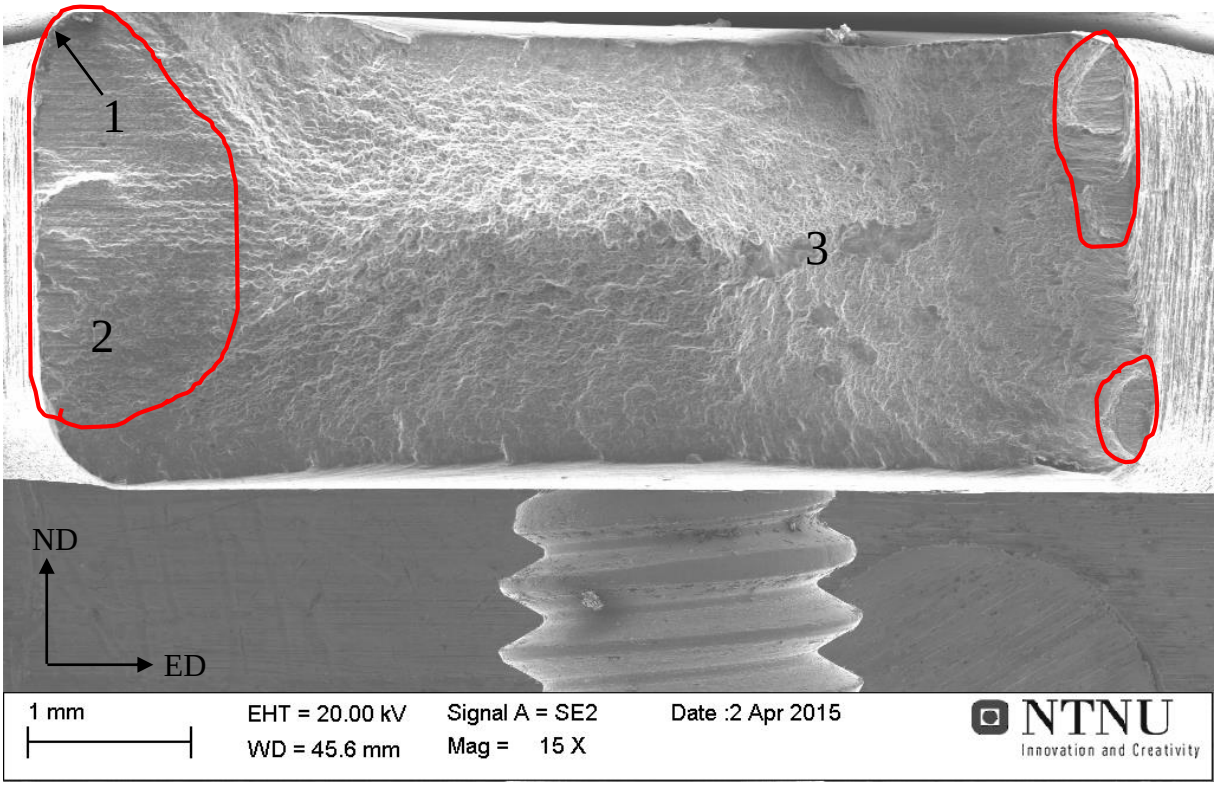

Figure 107: An overview of the fractured surface of AA6082 T1 with the shortest fatigue life, 15X magnification. The fatigue fractured areas are enclosed by the red lines.

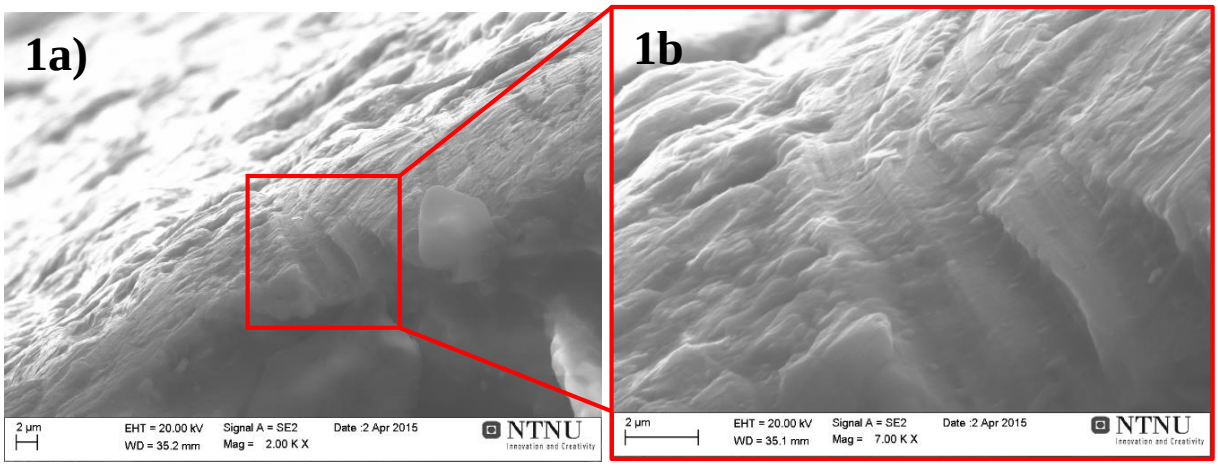

Figure 108: 1a) One possible initiation point due to an increase in surface roughness with 2000X magnification, and 1b) with 7000X magnification.

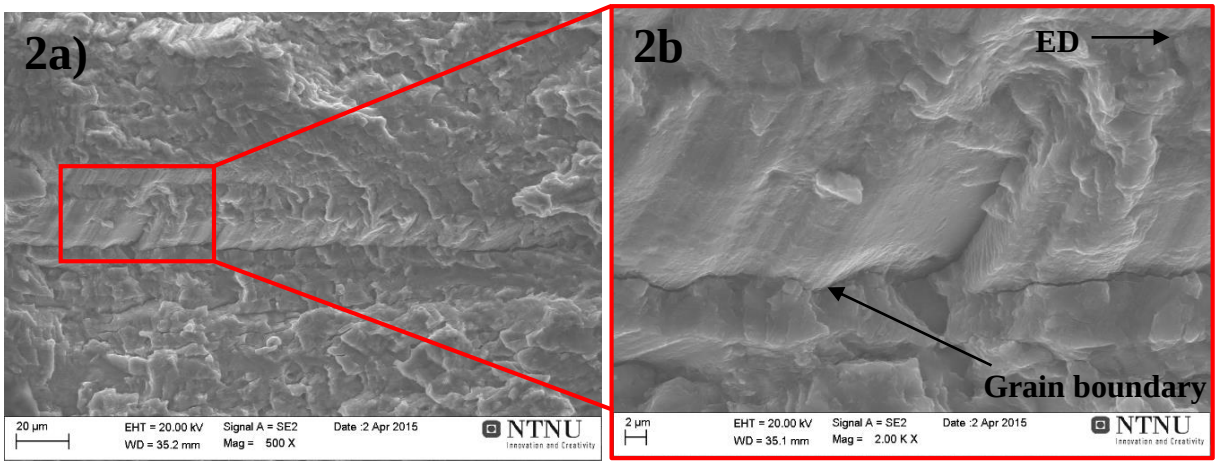

Figure 109: 2a) Transgranular crack propagation with some degree of slip localization, with 500X magnification, and 2b) slip localized growth in between the transgranular growth, with 2000X magnification.

The AA6082 T4 fatigue specimen with the longest fatigue life

The AA6082 T4 specimen with the longest fatigue life before RO, endured $6.60 \cdot 10^5$ cycles before failure. Figure 110 shows an overview of the fractured surface. The red line encloses the fatigue fractured area. The numbers 1-3 is the fracture initiation point, the fatigue growth area and the final fracture, respectively. The number 1-3 are shown below in Figure 111-Figure 113.

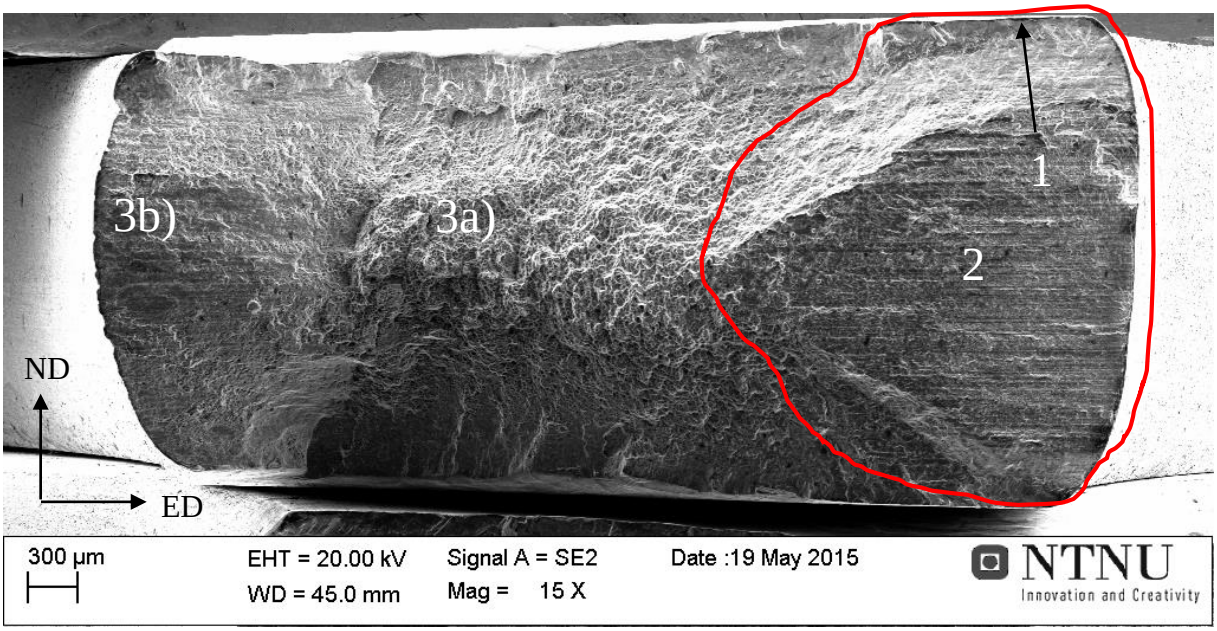

Figure 110: An overview of the fractured surface of AA6082 T4 with the longest fatigue life, 15X magnification. The fatigue fractured area is enclosed by the red line.

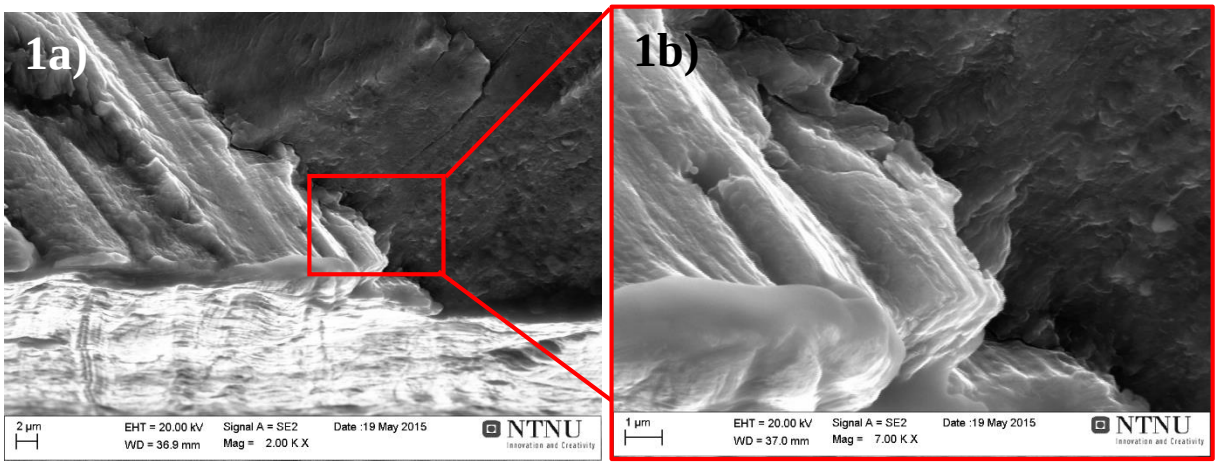

Figure 111: 1a) One possible initiation point due to an increase in surface roughness with 2000X magnification, and 1b) with 7000X magnification.

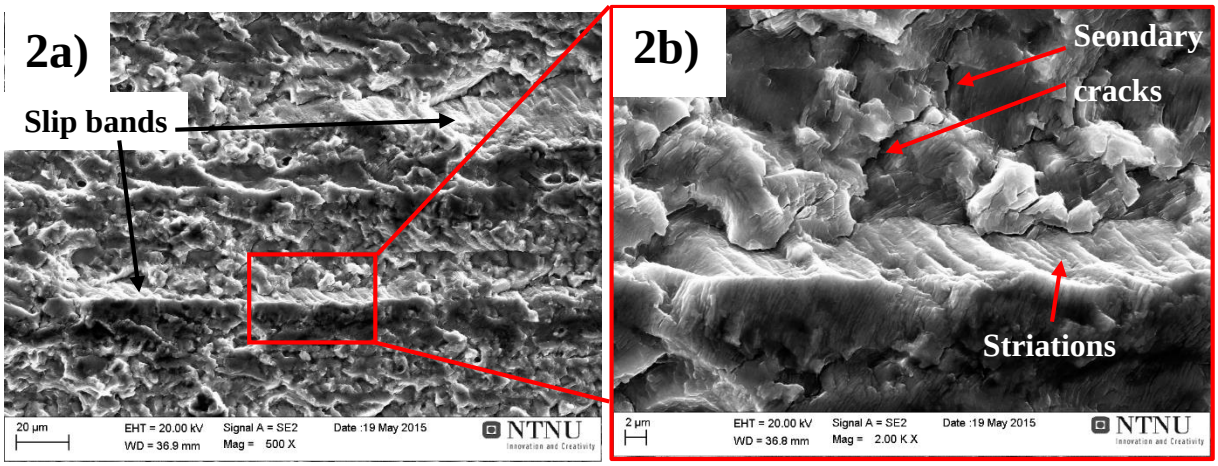

Figure 112: 2a) Transgranular crack propagation, with 500X magnification, and 2b) secondary cracks and slip bands with striations, with 2000X magnification.

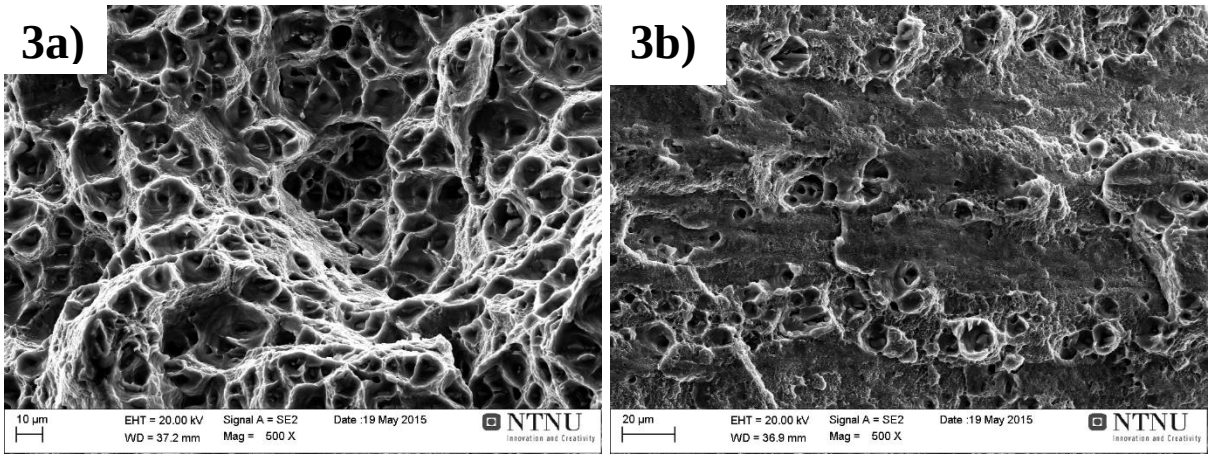

Figure 113: The final fracture, 500X magnification, 3a) dimples in the middle of the fractured surface, 3b) some dimples, micro shear and maybe fatigue crack propagation, at the left side of the fractured surface. This area was not further investigated.

The AA6082 T4 fatigue specimen with the shortest fatigue life

The AA6082 T4 specimen with the shortest fatigue life, endured $5.67 \cdot 10^5$ cycles before failure. Figure 114 shows an overview of the fractured surface. The red lines encloses the fatigue fractured areas. The numbers 1-3 is the fracture initiation point, the fatigue growth area and the final fracture, respectively. The number 1-3 are shown below in Figure 115-Figure 117.

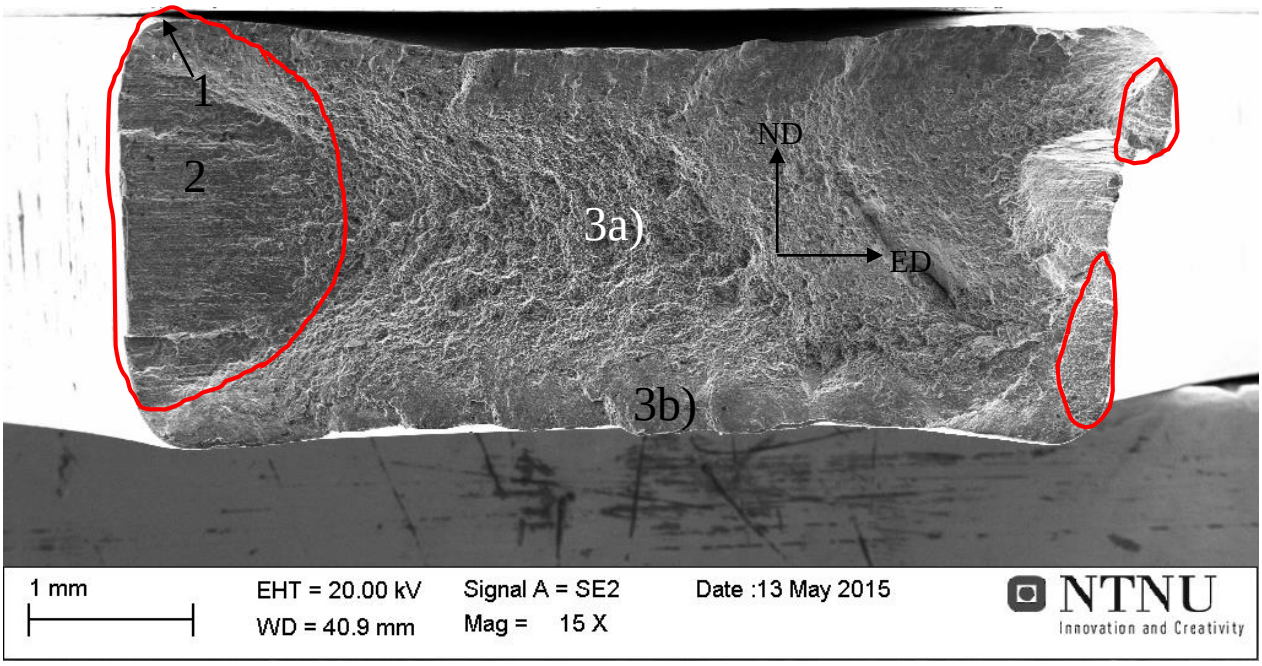

Figure 114: An overview of the fractured surface of AA6082 T4 with the shortest fatigue life, 15X magnification. The fatigue fractured areas are enclosed by the red lines.

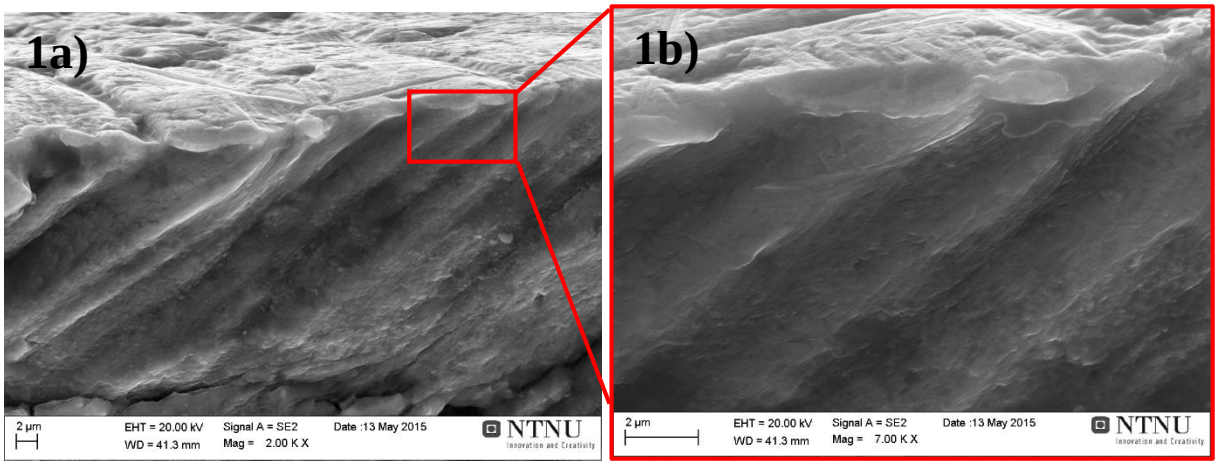

Figure 115: 1a) One possible initiation point due to an increase in surface roughness with 2000X magnification, and 1b) slip bands, with 7000X magnification.

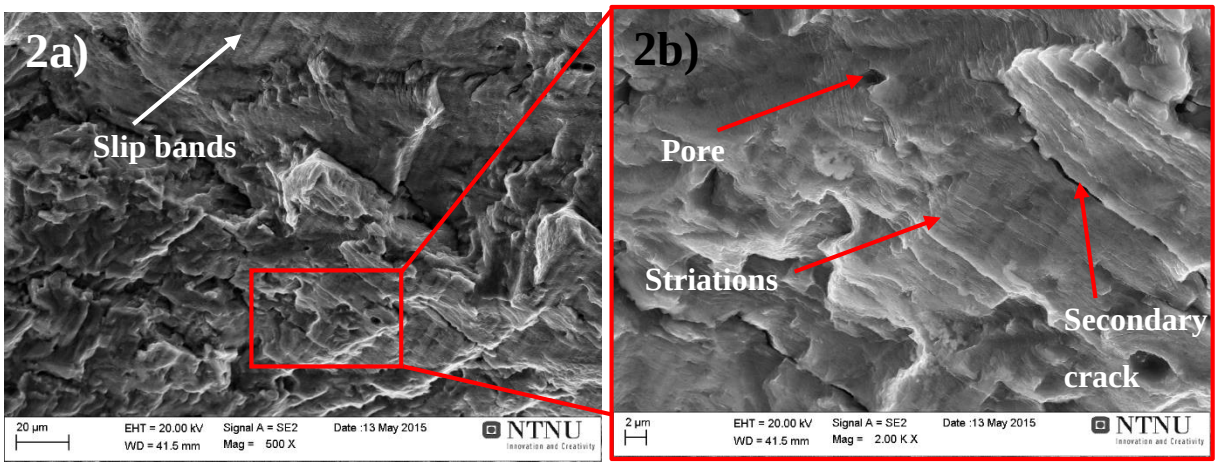

Figure 116: 2a) Transgranular crack propagation with slip localization in between, with 500X magnification, and 2b) striations, a pore and a secondary crack, with 2000X magnification.

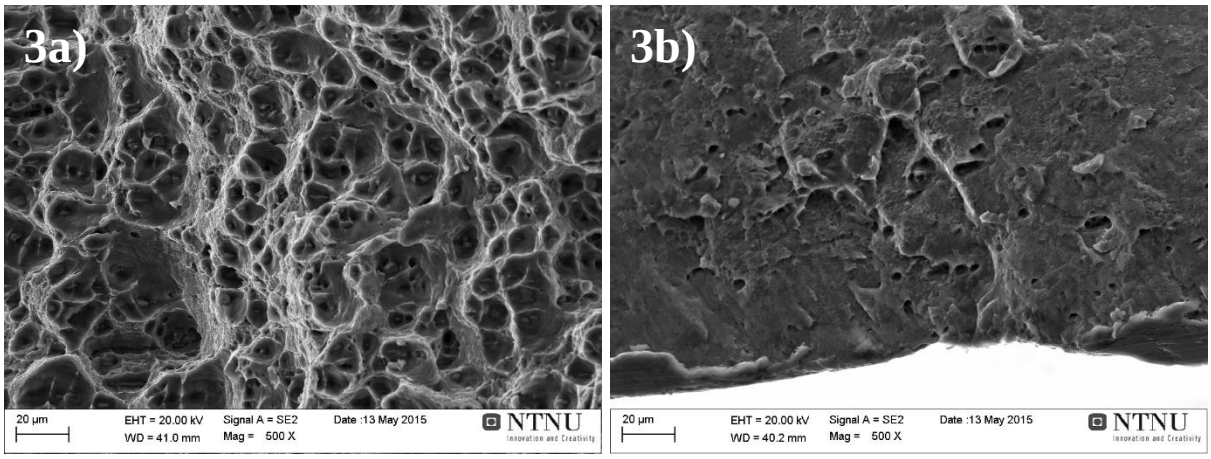

Figure 117: The final fracture with 500X magnifications 3a) dimples in the middle of the fractured surface and 3b) micro shear at the edge of the fractured surface.

The AA6082 T5 specimen with the longest fatigue life

The AA6082 T5 specimen with the longest fatigue life before RO, endured $1.45 \cdot 10^6$ cycles before failure. Figure 118 shows an overview of the fractured surface. The red line encloses the fatigue fractured area. The numbers 1-3 is the fracture initiation point, the fatigue growth area and the final fracture, respectively. The number 1-3 are shown below in Figure 119-Figure 121.

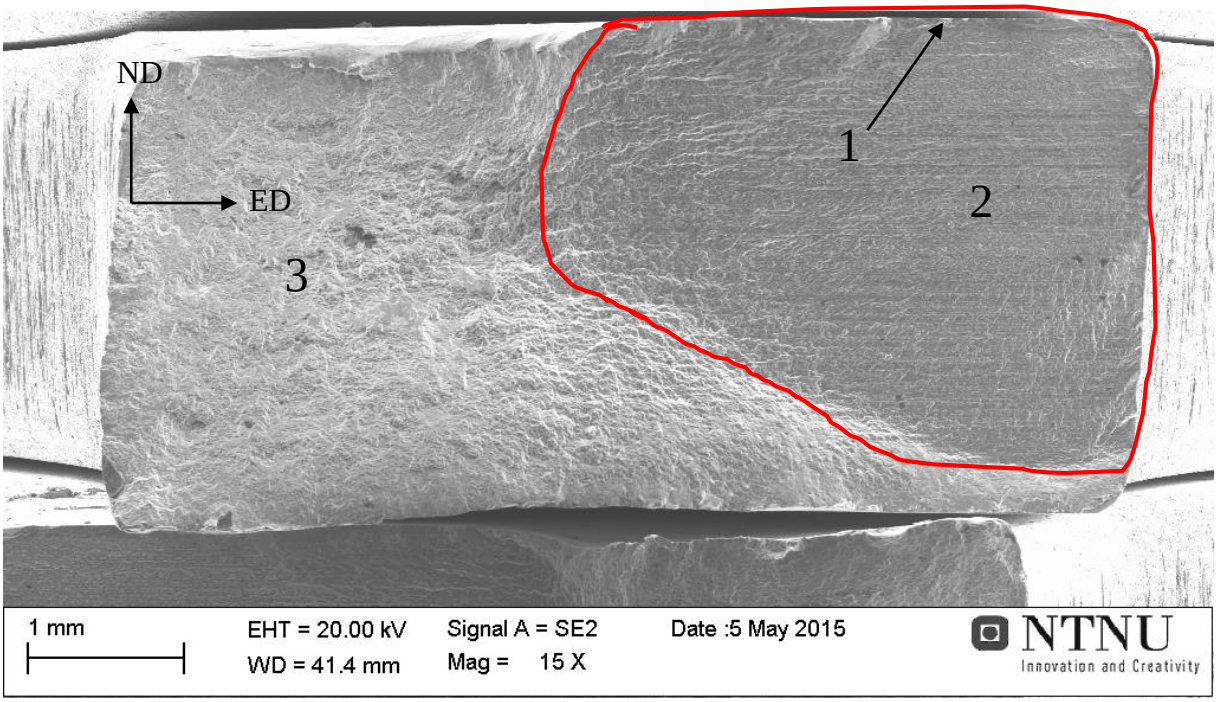

Figure 118: An overview of the fractured surface of AA6082 T5 with the longest fatigue life, 15X magnification. The fatigue fractured area is enclosed by the red line.

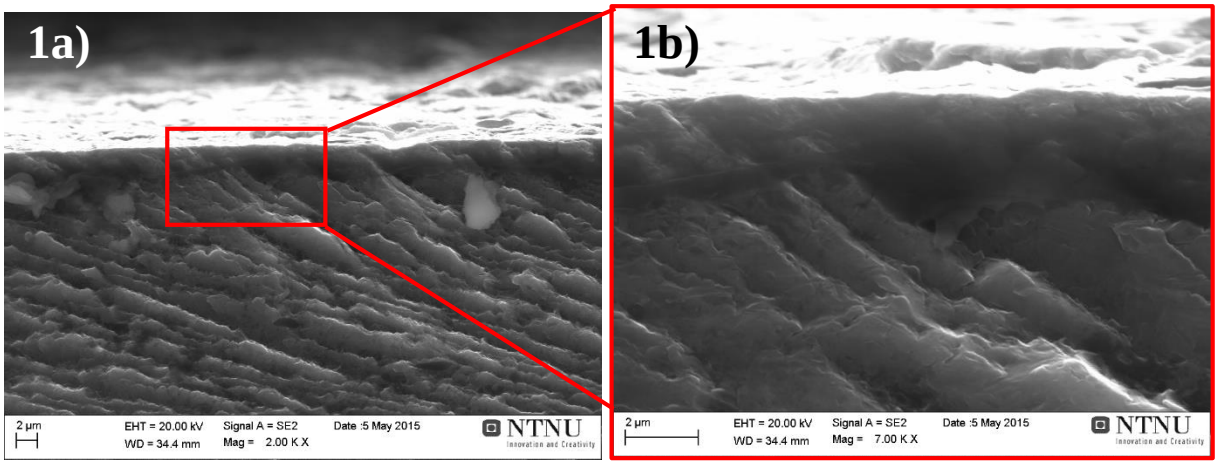

Figure 119: 1a) One possible initiation point due to an increase in surface roughness with 2000X magnification, and 1b) striations with 7000X magnification.

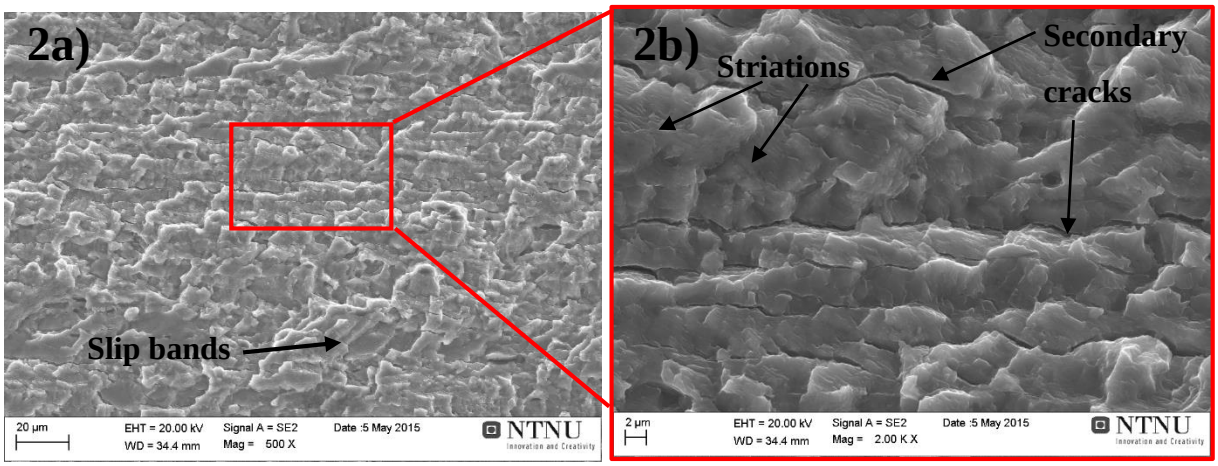

Figure 120: 2a) Transgranular crack propagation area (with a small degree of slip bands), with 500X magnification, and 2b) short striations and secondary cracks, with 2000X magnification.

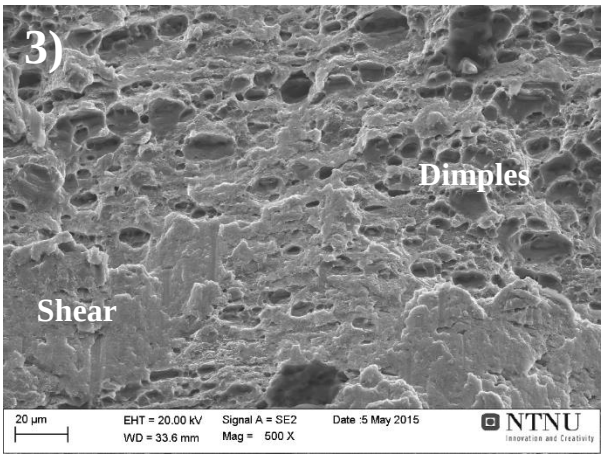

Figure 121: 3) The final fracture, a mixed mode of dimples and micro shear, with 500X magnification.

The AA6082 T5 specimen with the shortest fatigue life

The AA6082 T5 with the shortest fatigue life, endured $1.83 \cdot 10^5$ cycles before failure. Figure 122 shows an overview of the fractured surface. The red line encloses the fatigue fractured area. The numbers 1-3 is the fracture initiation point, the fatigue growth area and the final fracture, respectively. The number 1-2 are shown below in Figure 123 and Figure 124 . The final fracture, point number 3, is the same as for the specimen with the longest fatigue life, hence see Figure 121.

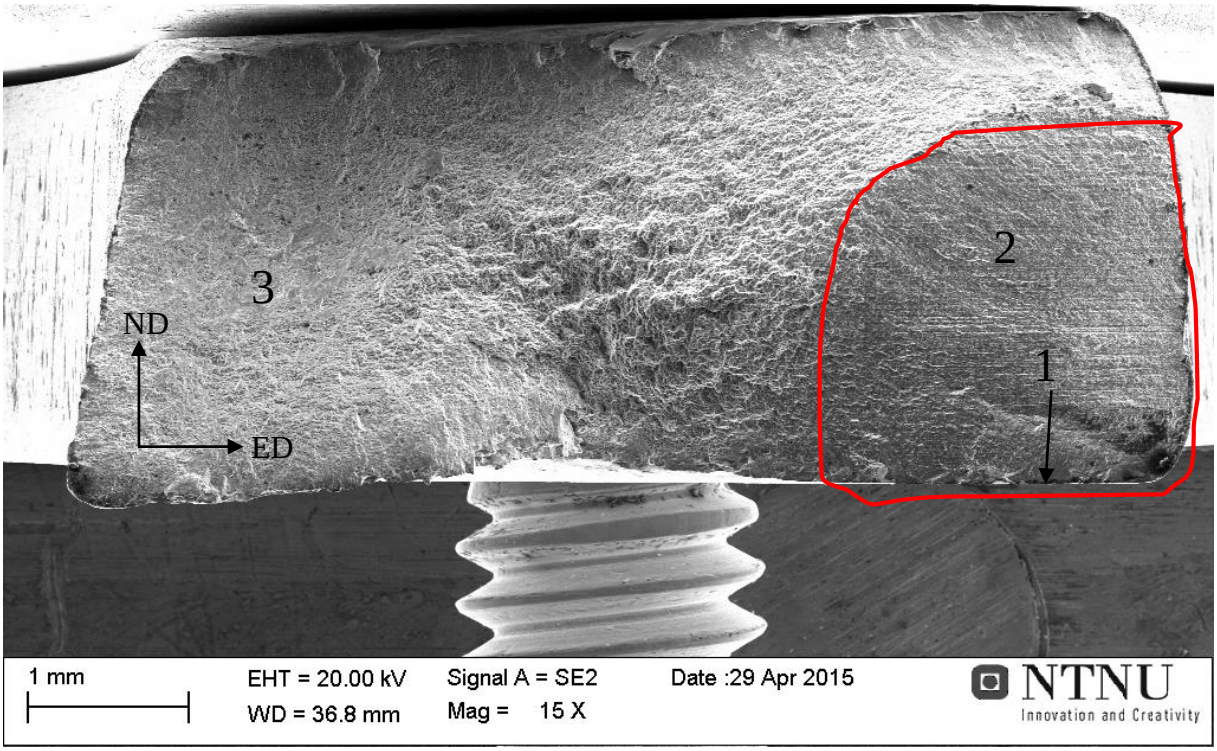

Figure 122: An overview of the fractured surface of AA6082 T5 with the shortest fatigue life, 15X magnification. The fatigue fractured area is enclosed by the red line.

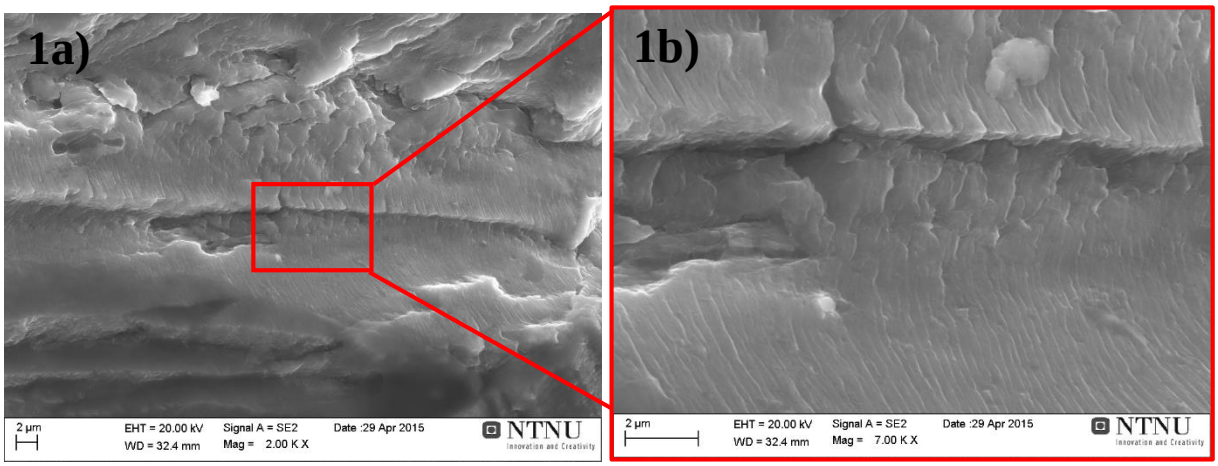

Figure 123: 1a) One possible initiation point, with 2000X magnification, and 1b) striations, with 7000X magnification.

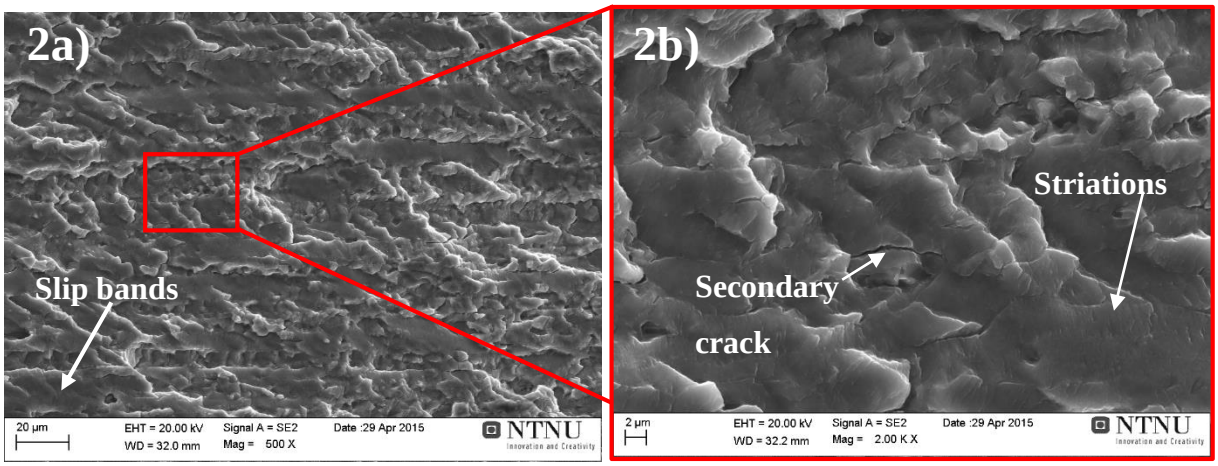

Figure 124: 2a) Transgranular crack propagation area (with a small degree of slip bands), with 500X magnification, and 2b) short striations and secondary cracks, with 2000X magnification.

The AA6082 T6 specimen with the longest fatigue life

The AA6082 T6 specimen with the longest fatigue life before RO, endured $1.85 \cdot 10^6$ cycles before failure. Figure 125 shows an overview of the fractured surface. The red line encloses the fatigue fractured area. The numbers 1-3 is the fracture initiation point, the fatigue growth area and the final fracture, respectively. The number 1-3 are shown below in Figure 126-Figure 128.

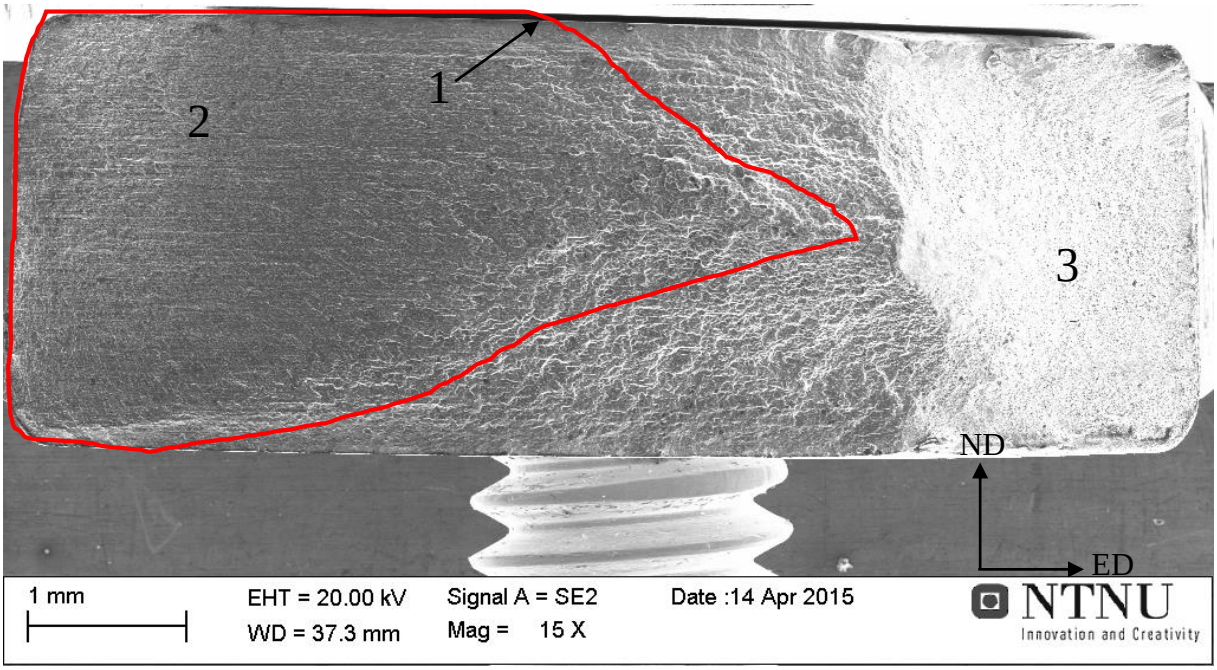

Figure 125: An overview of the fractured surface of AA6082 T6 with the longest fatigue life, 15X magnification. The fatigue fractured area is enclosed by the red line.

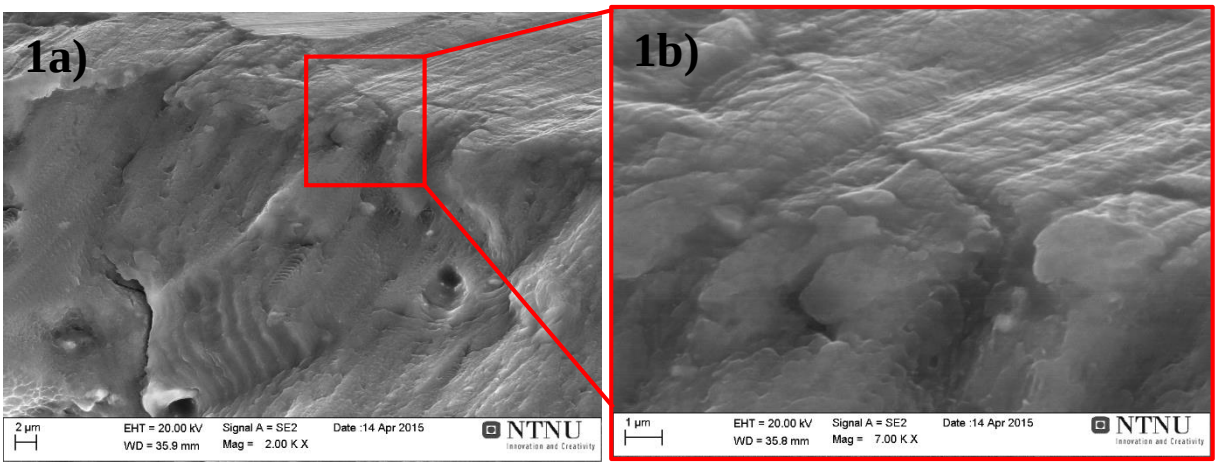

Figure 126: 1a) One possible initiation point due to an increase in surface roughness with 2000X magnification, and 1b) striations nearby, with 7000X magnification.

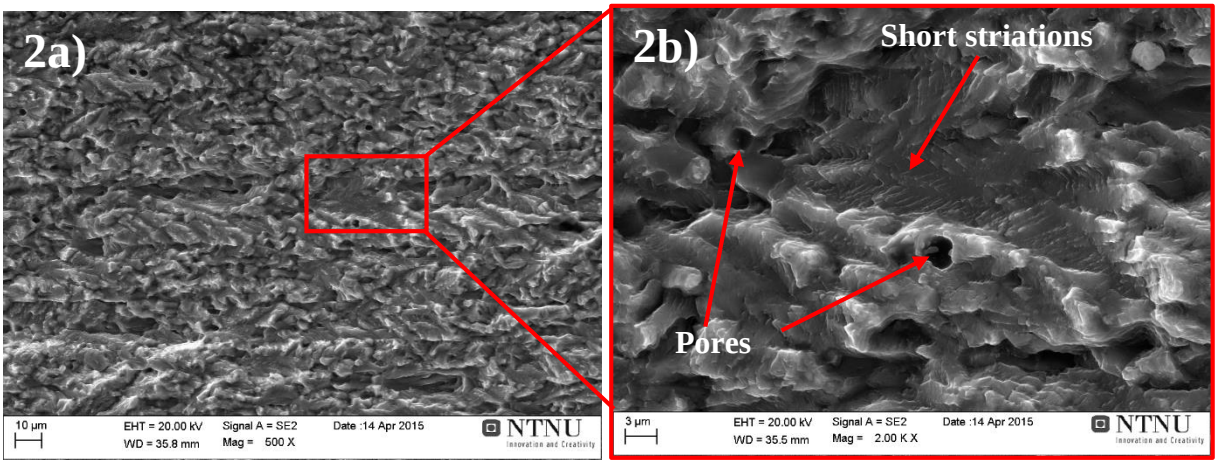

Figure 127: 2a) Transgranular growth, with 500X magnification, and 2b) pores and short striations, with 2000X magnification.

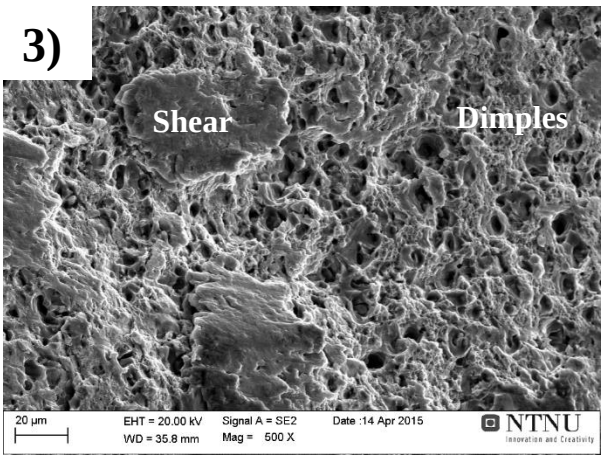

Figure 128: The final fracture, a mixed mode of both micro shear and dimples, with a magnification of 500X.

The AA6082 T6 specimen with the shortest fatigue life

The AA6082 T6 specimen with the shortest fatigue life, endured $5.87 \cdot 10^3$ cycles before failure. Figure 129 shows an overview of the fractured surface. The red line encloses the fatigue fractured areas. The numbers 1-3 is the fracture initiation point, the fatigue growth area and the final fracture, respectively. The number 1-3 are shown below in Figure 130 and Figure 131. The final fracture, point number 3 is the same as for the specimen with the longest fatigue life.

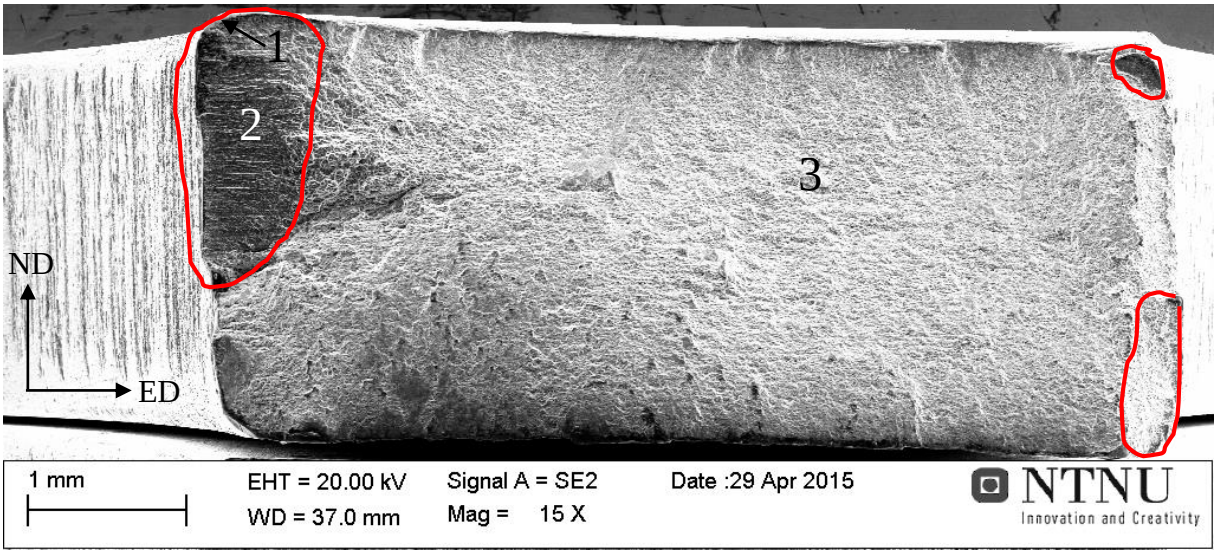

Figure 129: An overview of the fractured surface of AA6082 T6 with the longest fatigue life, 15X magnification. The fatigue fractured areas are enclosed by the red lines.

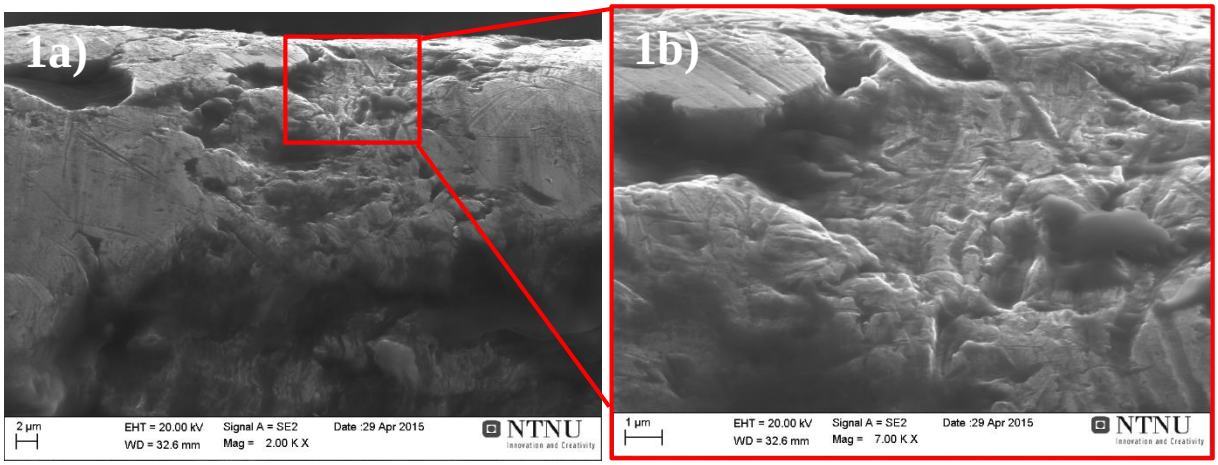

Figure 130: 1a) One possible initiation point at a notch due to an increase in surface roughness with 2000X magnification, and 1b) the notch, with 7000X magnification.

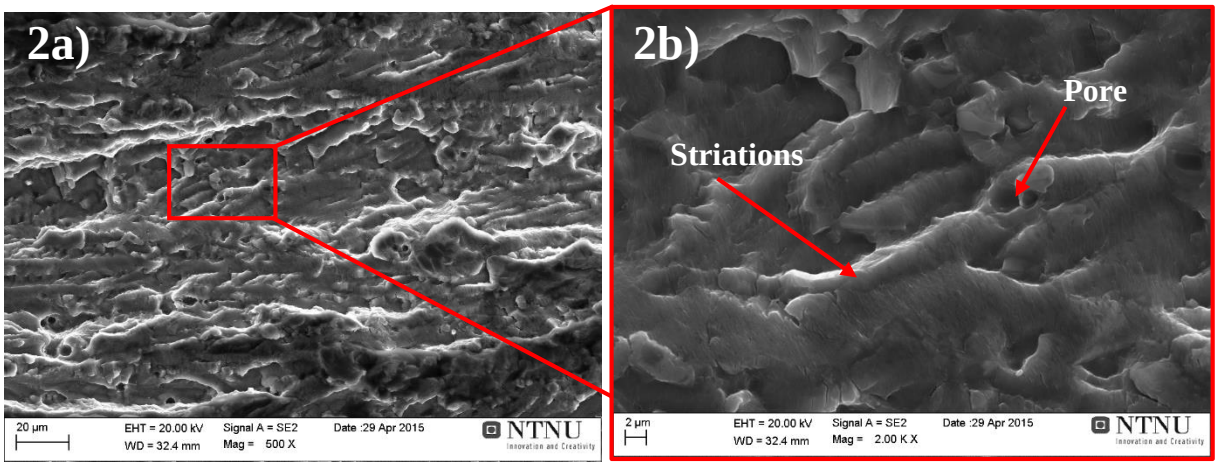

Figure 131: 2a) Transgranular crack propagation with 500X magnification, and 2b) striations and pores.

Fractography of AA7108

The T1 specimen with the longest fatigue life

The AA7108 T1 specimen with the longest fatigue before RO, endured $1.51 \cdot 10^6$ cycles before failure. Figure 132 shows an overview of the fractured surface. The red line encloses the fatigue fractured area. The numbers 1-3 is the fracture initiation point, the fatigue growth area and the final fracture, respectively. The number 1-3 are shown below in Figure 133-Figure 135.

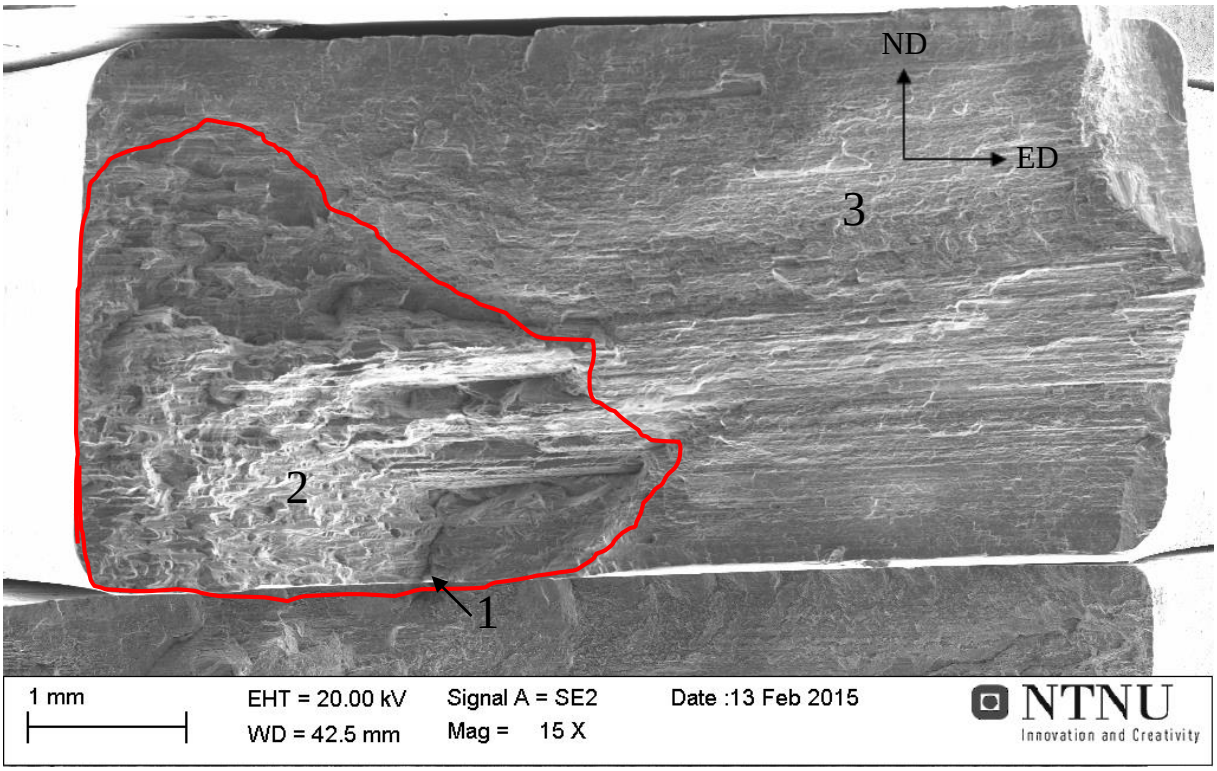

Figure 132: An overview of the fractured surface of AA7108 T1 with the longest fatigue life, 15X magnification. The fatigue fractured area is enclosed by the red line.

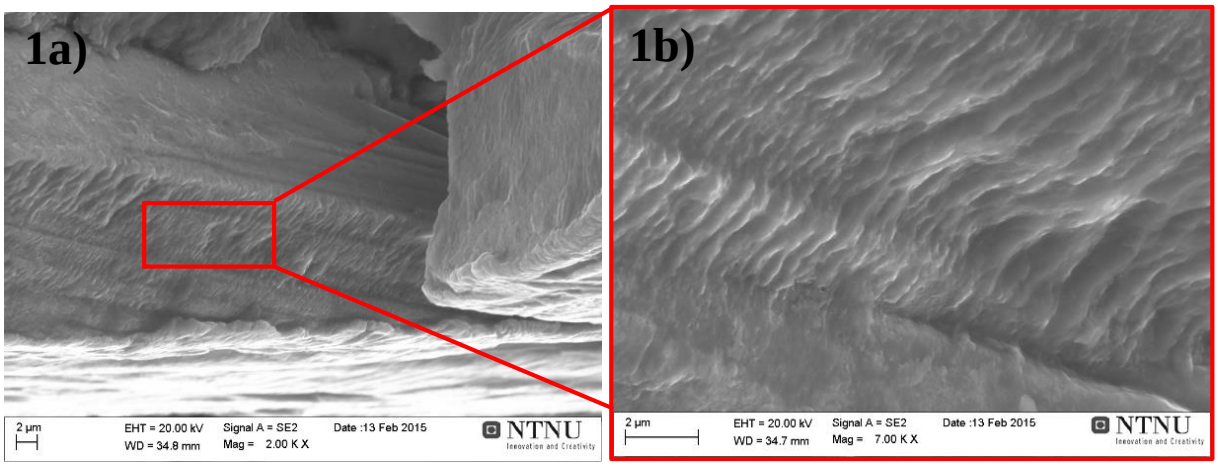

Figure 133: 1a) One possible initiation point at the groove, with 2000X magnification, and 1b) striations nearby, with 7000X magnification.

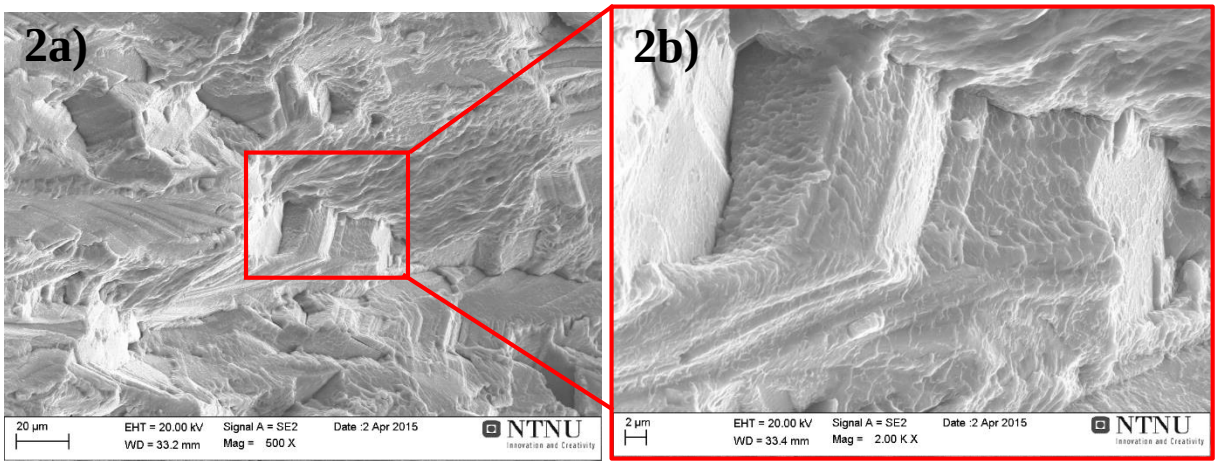

Figure 134: 2a) Slip localized stage II growth, with 500X magnification, and 2b) with 2000X magnification.

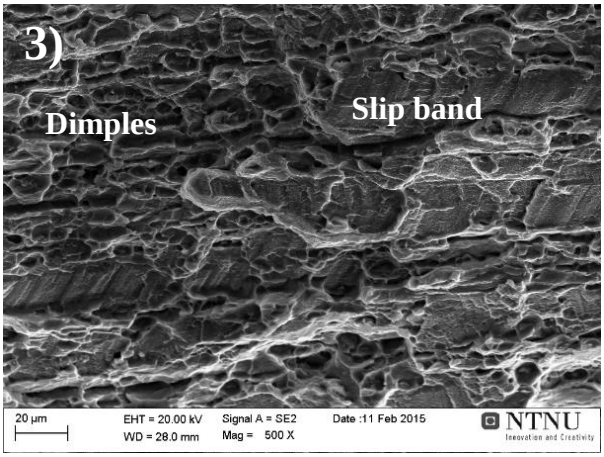

Figure 135: 3) The final fracture taken, a mixed mode of dimples and micro shear, with 500X magnification.

The AA7108 T1 specimen with the shortest fatigue life

The AA7108 T1 specimen with the shortest fatigue life, endured $2.68 \cdot 10^5$ cycles before failure. Figure 136 shows an overview of the fractured surface. The red line encloses the fatigue fractured area. The numbers 1-3 is the fracture initiation point, the fatigue growth area and the final fracture, respectively. The number 1-3 are shown below in Figure 137-Figure 139.

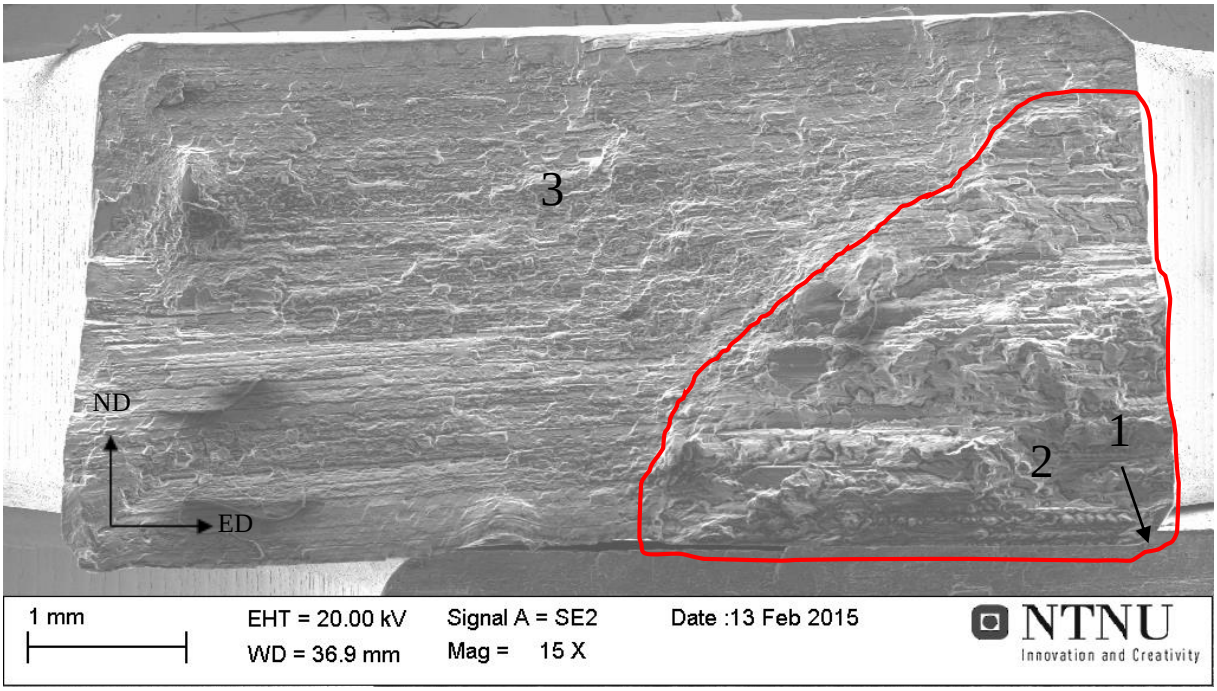

Figure 136: An overview of the fractured surface of AA7108 T1 with the shortest fatigue life, 15X magnification. The fatigue fractured area is enclosed by the red line.

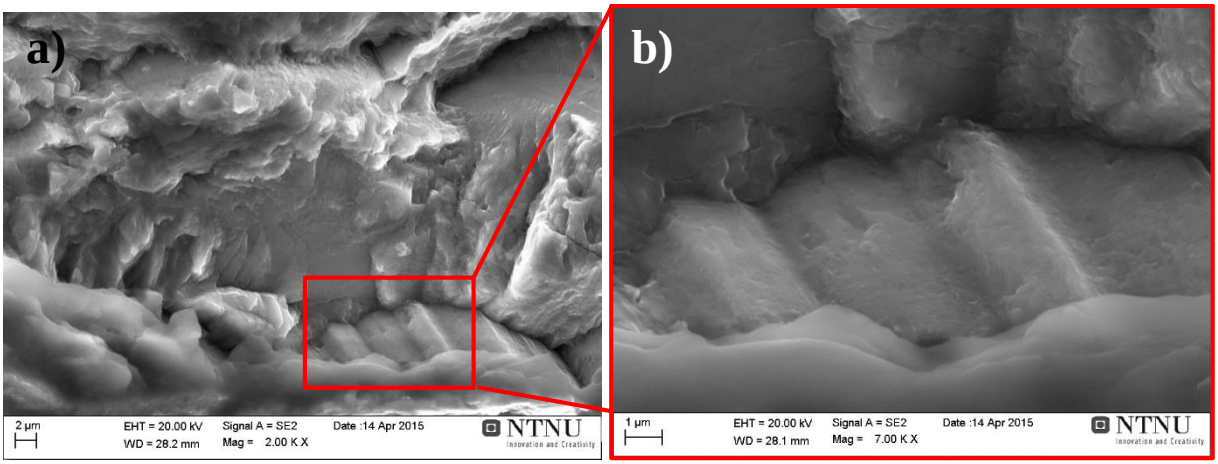

Figure 137: 1a) One possible initiation point, with 2000X magnification, and 1b) slip bands below with 7000X magnification.

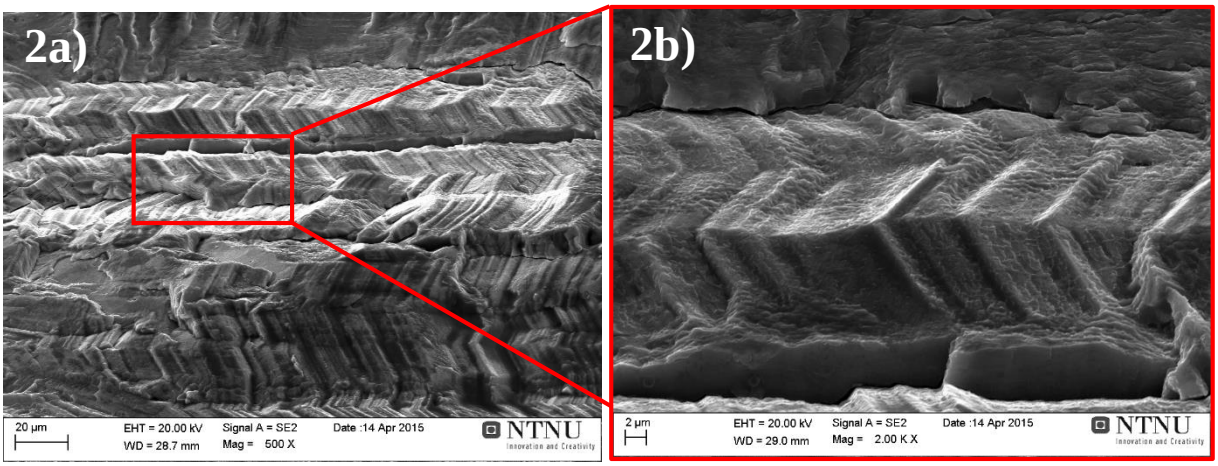

Figure 138: 2a) Slip localized stage II growth, with 500X magnification, and 2b) a close up on slip steps, with 2000X magnification.

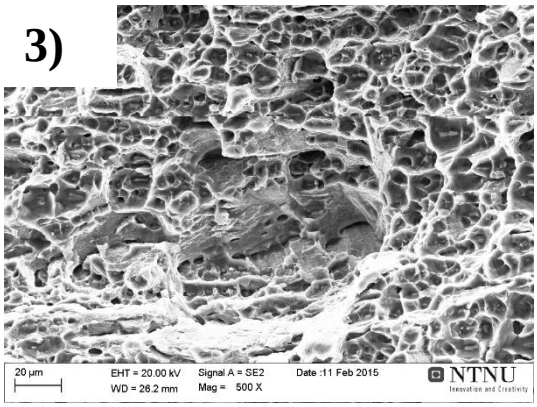

Figure 139: 3) The final fracture taken, dimples and micro shear, with 500X magnification.

The AA7108 T4 specimen with the longest fatigue life

The AA7108 T4 specimen with the longest fatigue life before RO, endured $6.3 \cdot 10^6$ cycles before failure. Figure 140 shows an overview of the fractured surface. The red line encloses the fatigue fractured area. The numbers 1-3 is the fracture initiation point, the fatigue growth area and the final fracture, respectively. The number 1-3 are shown below in Figure 141-Figure 143.

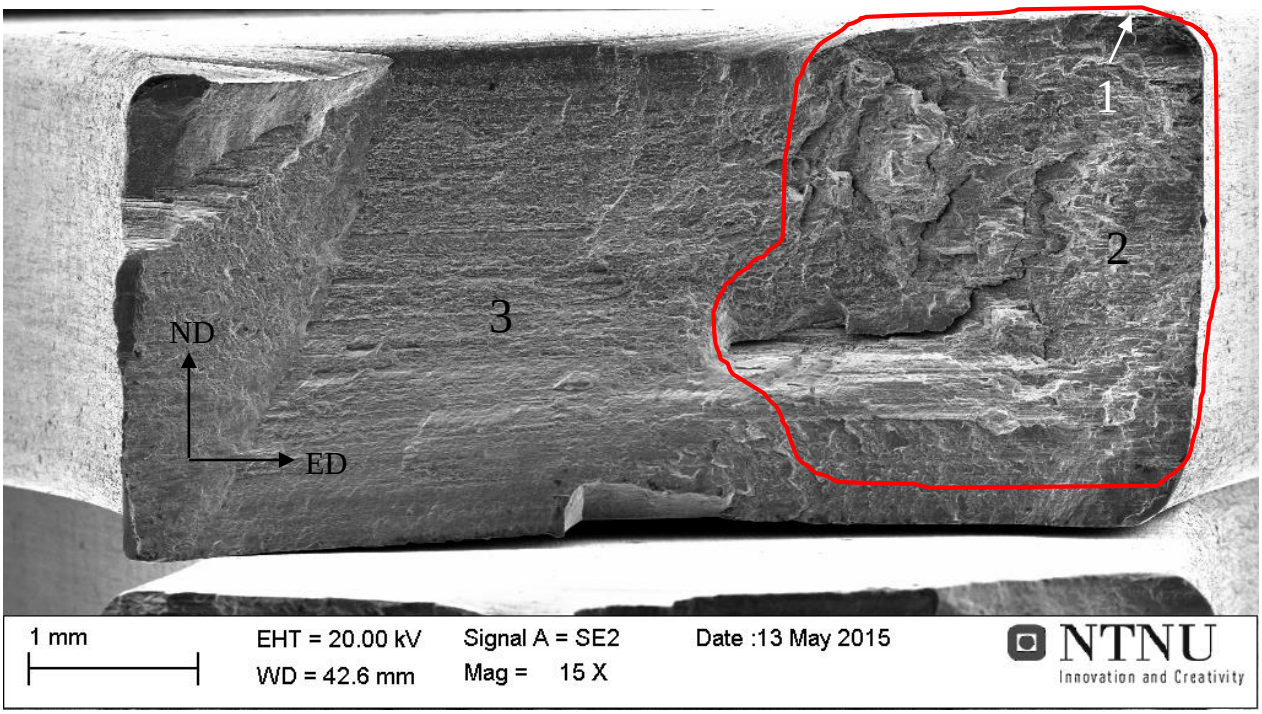

Figure 140: An overview of the fractured surface of AA7108 T4 with the longest fatigue life, 15X magnification. The fatigue fractured area is enclosed by the red line.

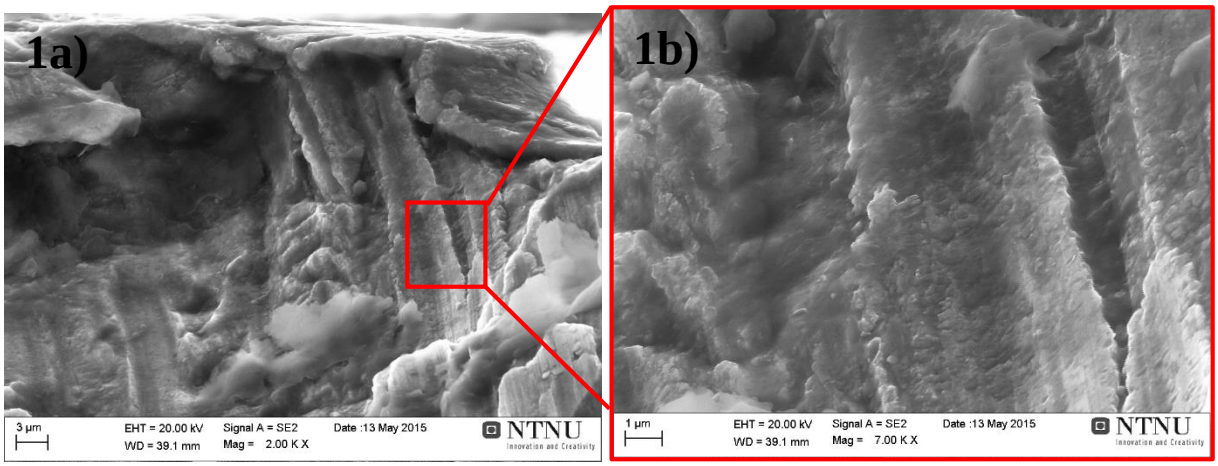

Figure 141: 1a) One possible initiation point along the specimen edge, with 2000X and b) slip band and striations nearby, with 7000X.

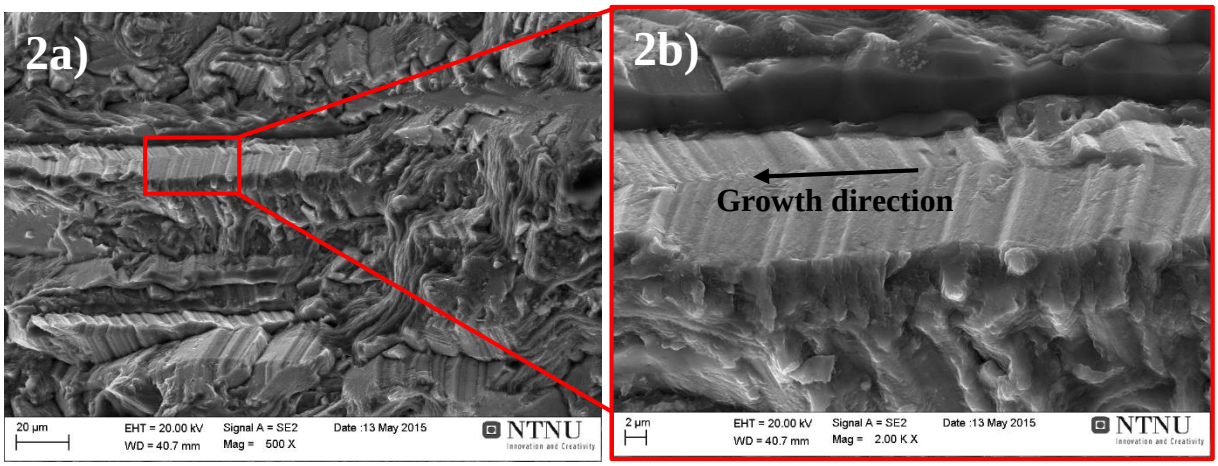

Figure 142: 2a) Slip localized stage II growth, with 500X magnification, and 2b) slip bands and striations, with 2000X magnification.

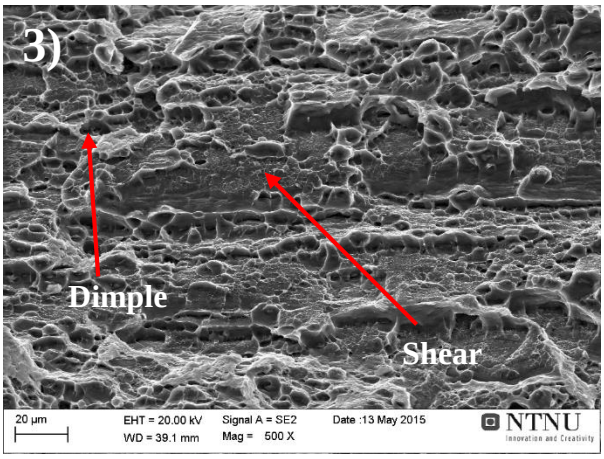

Figure 143: 3) The final fracture, a mixed mode of dimples and micro shear, with 500X magnification.

The AA7108 T4 specimen with the shortest fatigue life

The AA7108 T4 specimen with the shortest fatigue life, endured $1.24 \cdot 10^5$ cycles before failure. Figure 144 shows an overview of the fractured surface. The red line encloses the fatigue fractured area. The numbers 1-3 is the fracture initiation point, the fatigue growth area and the final fracture, respectively. The number 1-2 are shown below in Figure 145-Figure 146 . For point number 3, the final fracture was the same as for AA7108 T1 with the longest fatigue life, see Figure 143 for more information.

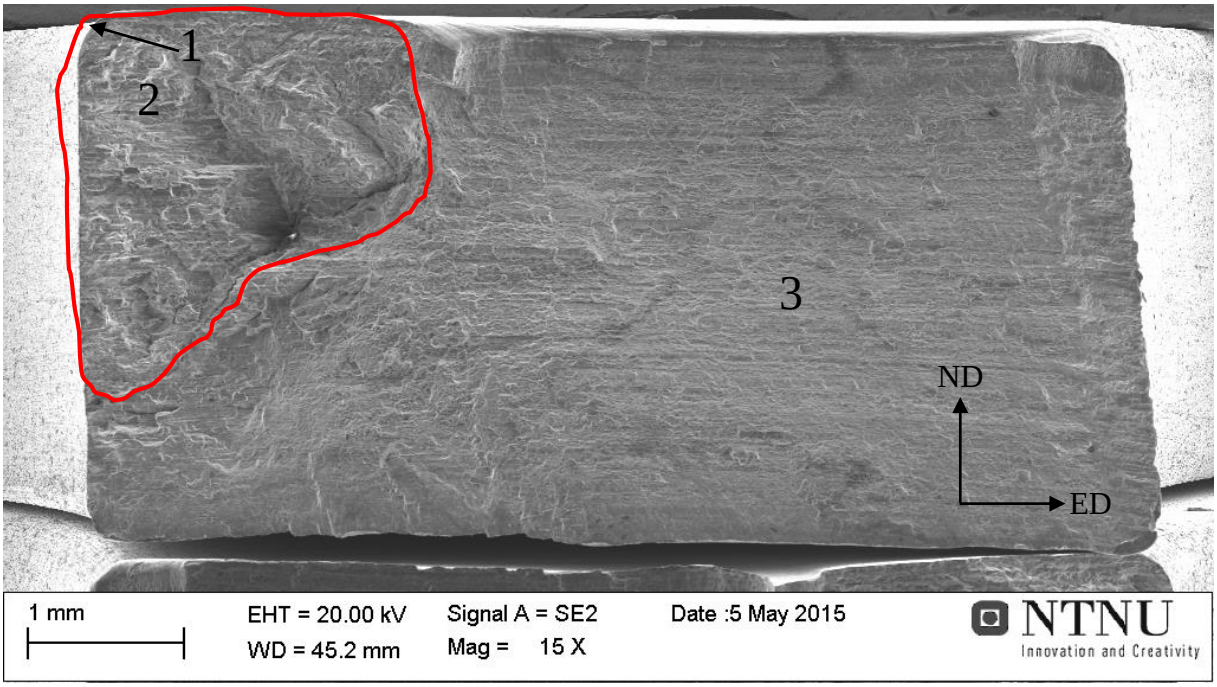

Figure 144: An overview of the fractured surface of AA7108 T4 with the shortest fatigue life, 15X magnification. The fatigue fractured area is enclosed by the red line.

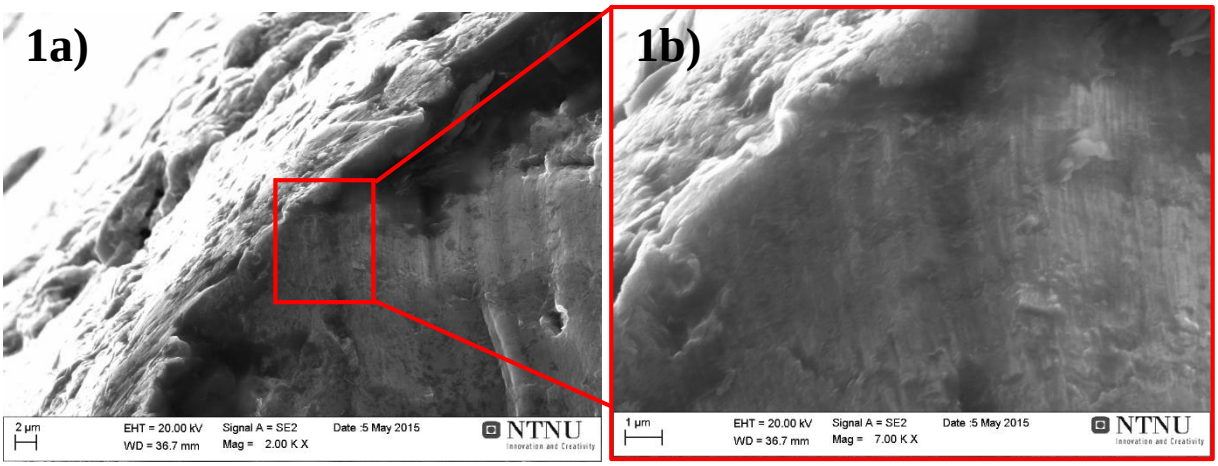

Figure 145: 1a) One possible initiation point taken at the specimen surface with 2000X magnification and 1b) striations, with 7000X magnification.

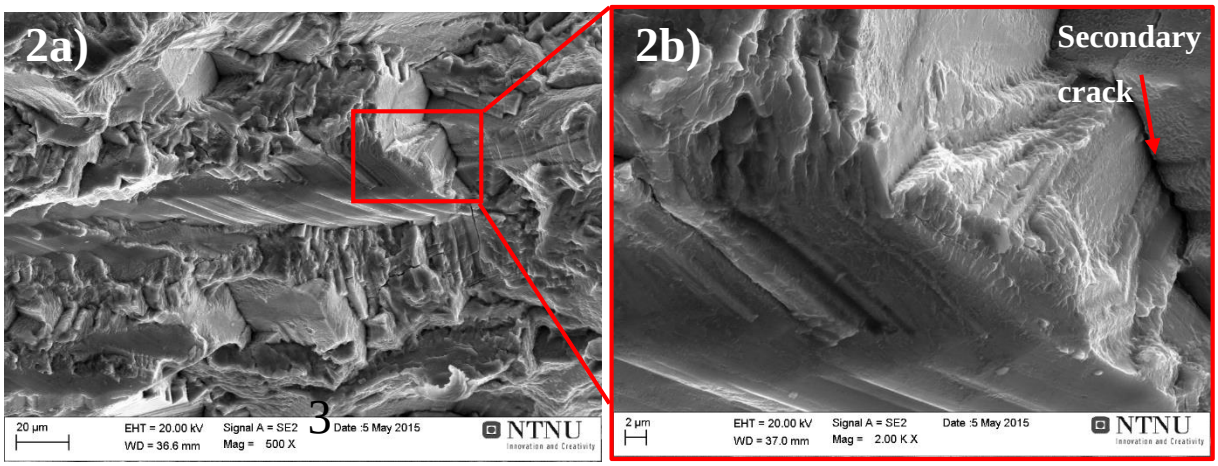

Figure 146: 2a) Slip localized stage II growth, with 500X magnification, and 2b) slip bands, striations and a secondary crack, with 2000X magnification.

The AA7108 T5 specimen with the longest fatigue life

The AA7108 T5 specimen with the longest fatigue life before RO, endured $1.26 \cdot 10^6$ cycles before failure. Figure 147 shows an overview of the fractured surface. The red line encloses the fatigue fractured area. The numbers 1-3 is the fracture initiation point, the fatigue growth area and the final fracture, respectively. The number 1-3 are shown below in Figure 148-Figure 150.

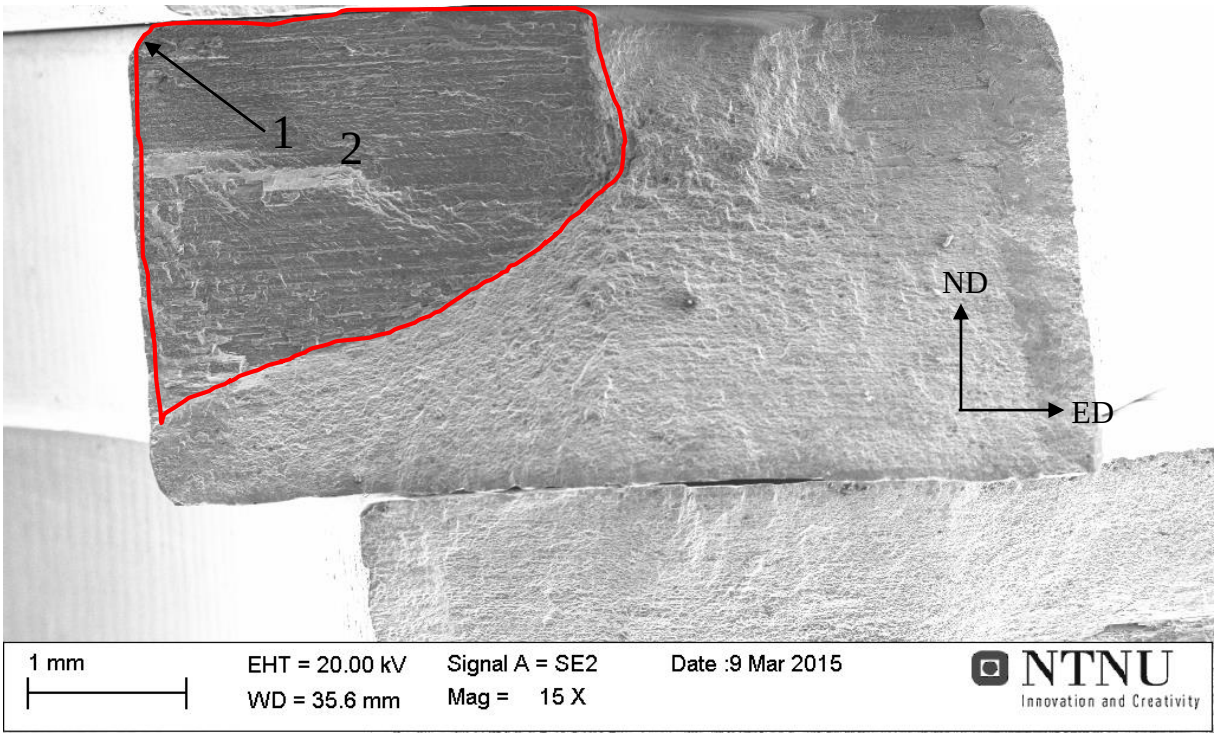

Figure 147: An overview of the fractured surface of AA7108 T5 with the longest fatigue life, 15X magnification. The fatigue fractured area is enclosed by the red line.

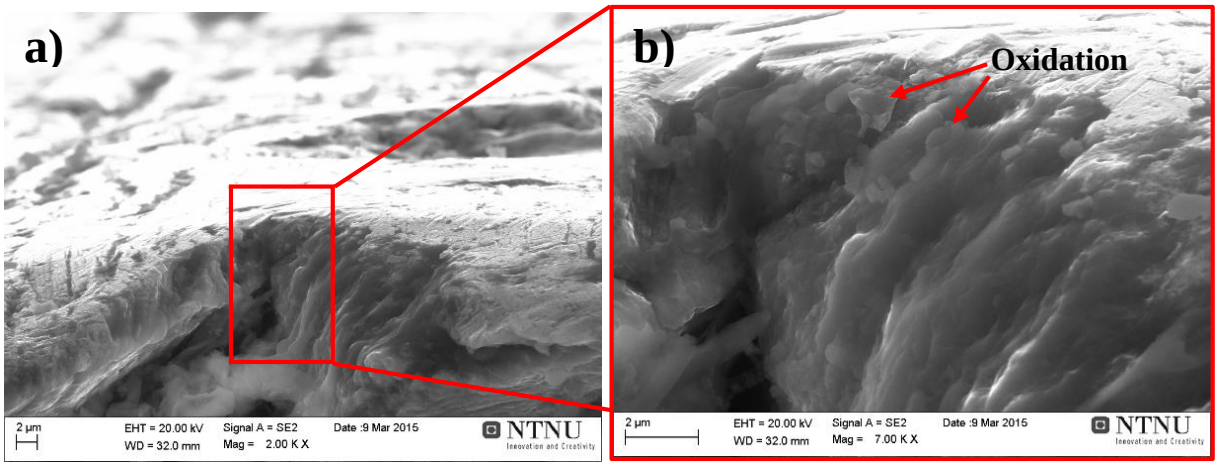

Figure 148: 1a) One possible initiation point at the notch on the specimen surface, with 2000X magnification and 1b) inside the notch with oxidation, with 7000X magnification.

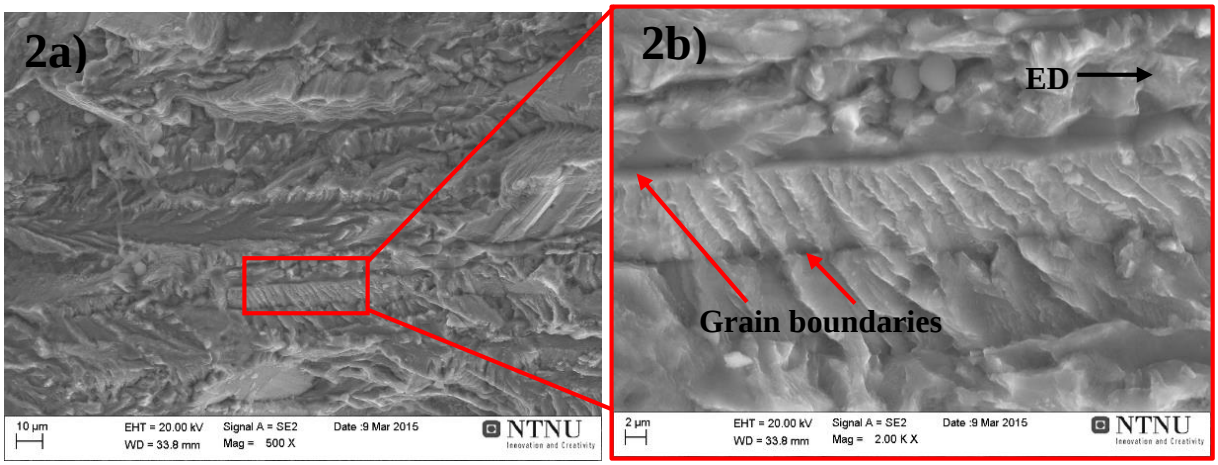

Figure 149: 2a) Transgranular crack propagation, with 500X magnification, and 2b) striations, with 2000X magnification.

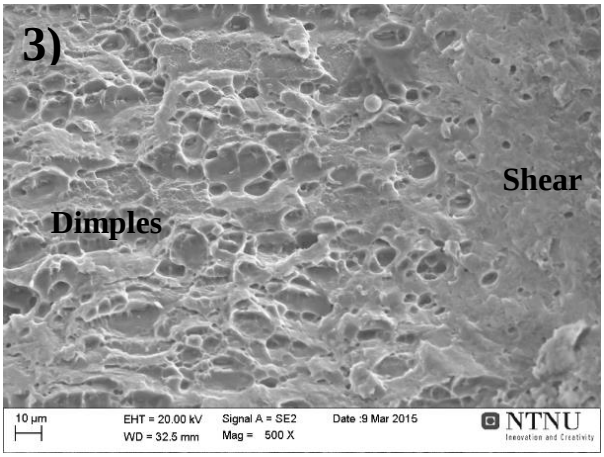

Figure 150: The final fracture, a mixed mode of micro shear and dimples, with a magnification of 500X.

The AA7108 T5 specimen with the shortest fatigue life

The AA7108 T5 specimen with the shortest fatigue life, endured $9.28 \cdot 10^4$ cycles before failure. Figure 151 shows an overview of the fractured surface. The red line encloses the fatigue fractured area. The numbers 1-3 is the fracture initiation point, the fatigue growth area and the final fracture, respectively. The number 1-2 are shown below in Figure 152 and Figure 153 . For point number 3, see Figure 150.

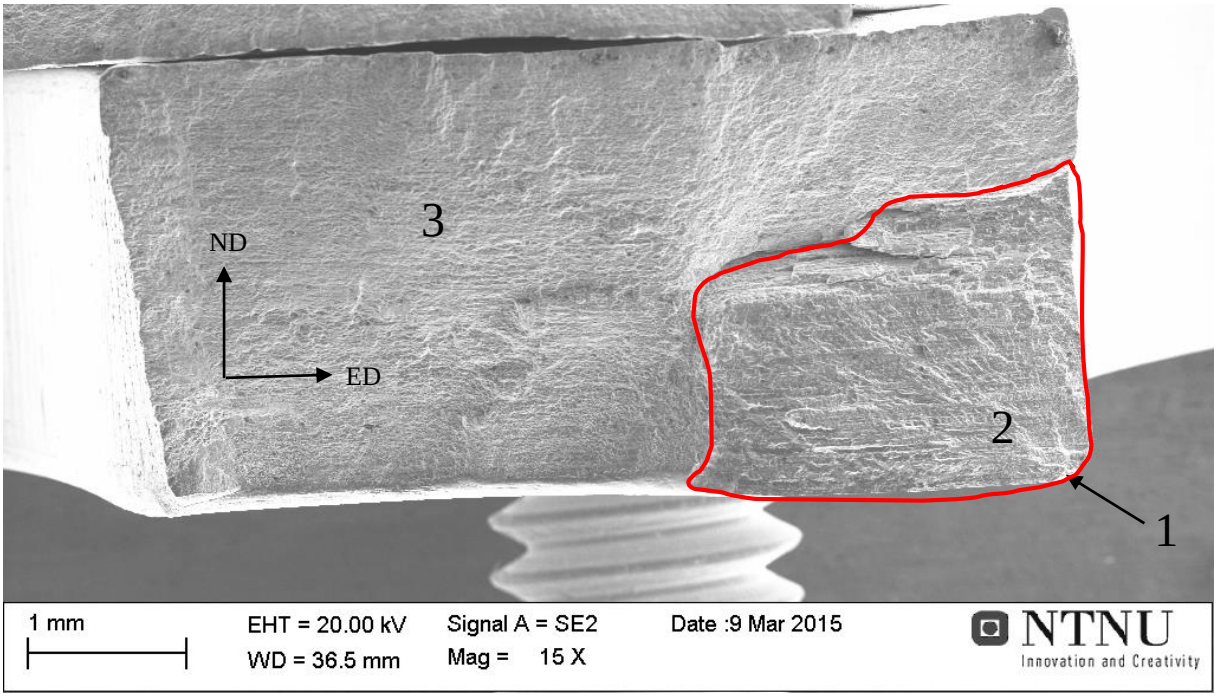

Figure 151: An overview of the fractured surface of AA7108 T5 with the shortest fatigue life, 15X magnification. The fatigue fractured area is enclosed by the red line.

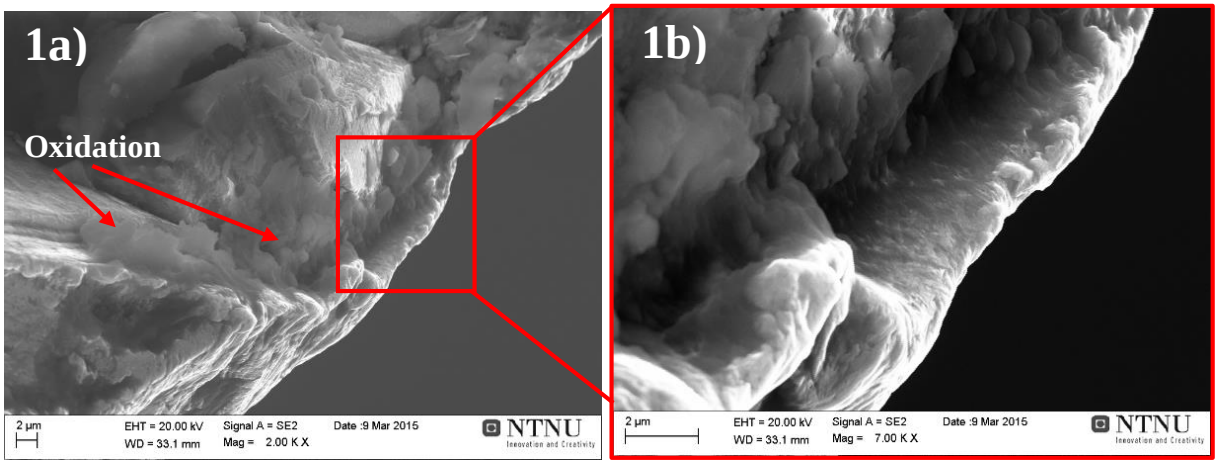

Figure 152: 1a) A notch, one possible initiation point nearby the corner, note the oxidation products, with 2000X magnification and b) with 7000X magnification.

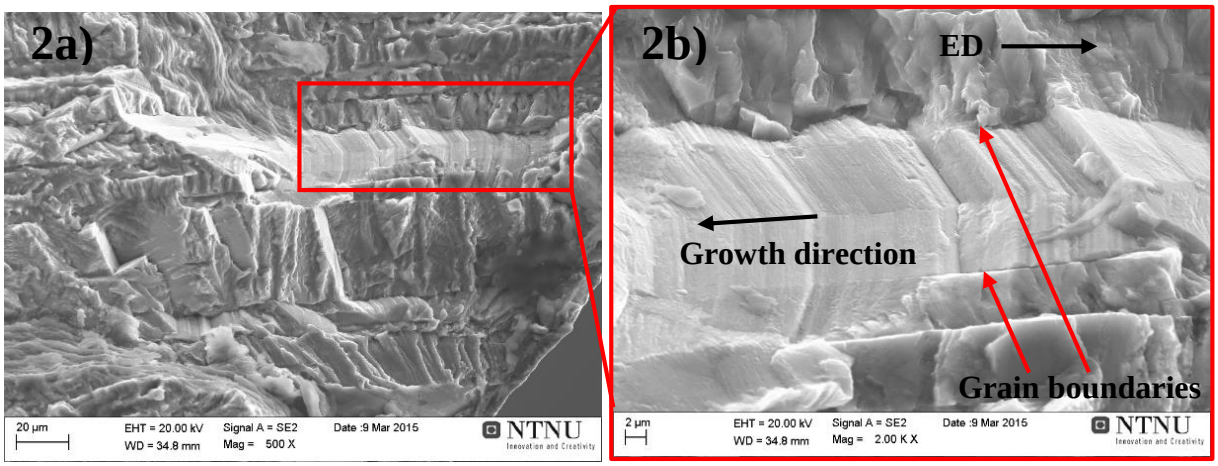

Figure 153: 2a) Both transgranular and slip localized growth, with 500X magnification, and b) GB-cracking, with 2000X magnification.

The AA7108 T6 specimen with the longest fatigue life

The AA7108 T6 specimen with the longest fatigue life before RO, endured $2.88 \cdot 10^5$ cycles before failure. Because the fractured surfaces of the specimen with the shortest fatigue life was very similar, only this specimen will be presented. Figure 154 shows an overview of the fractured surface. The red line encloses the fatigue fractured area. The numbers 1-3 is the fracture initiation point, the fatigue growth area and the final fracture, respectively. The number 1-3 are shown below in Figure 155-Figure 157.

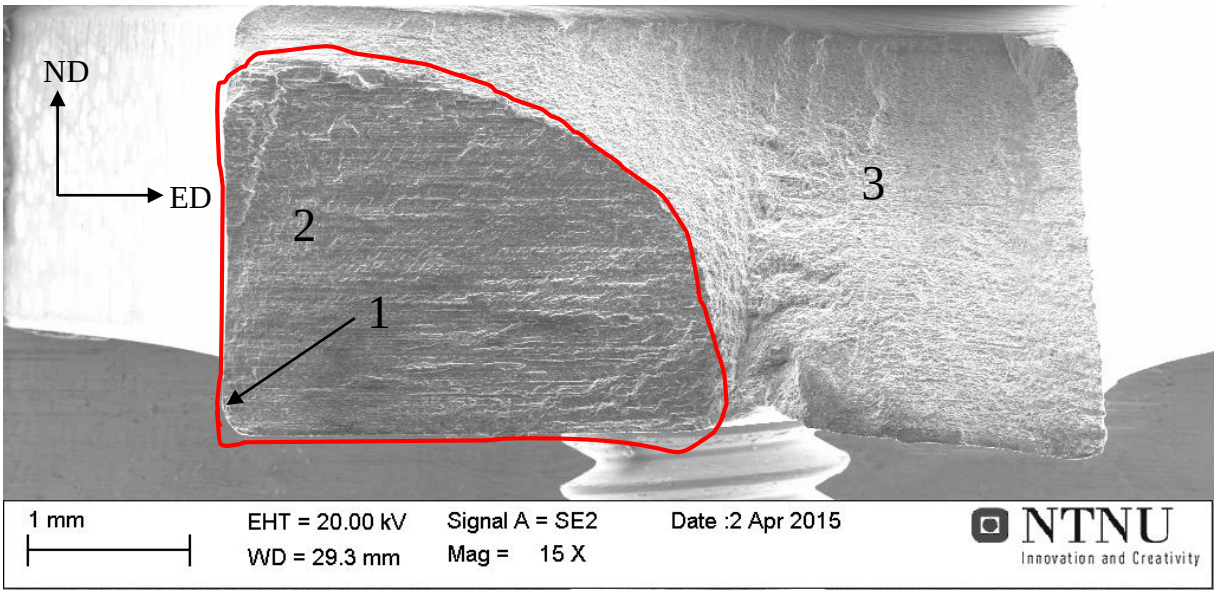

Figure 154: An overview of the fractured surface of AA7108 T6 with the longest fatigue life, 15X magnification. The fatigue fractured area is enclosed by the red line.

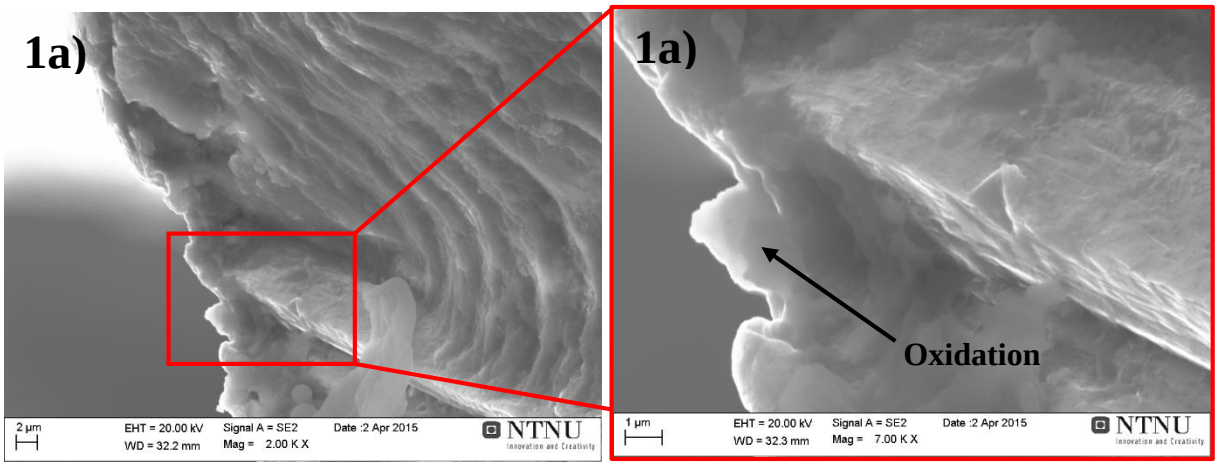

Figure 155: One possible initiation point, a) taken with 2000X and b) taken with 7000X.

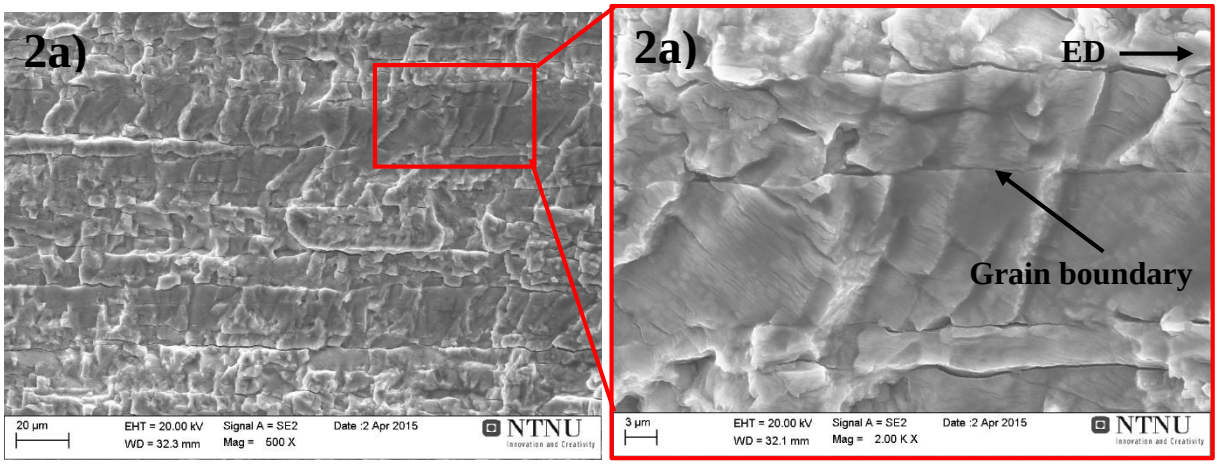

Figure 156: 2a) Transgranular stage II cracking, with 500X magnification, and 2b) short striations, with 2000X magnification.

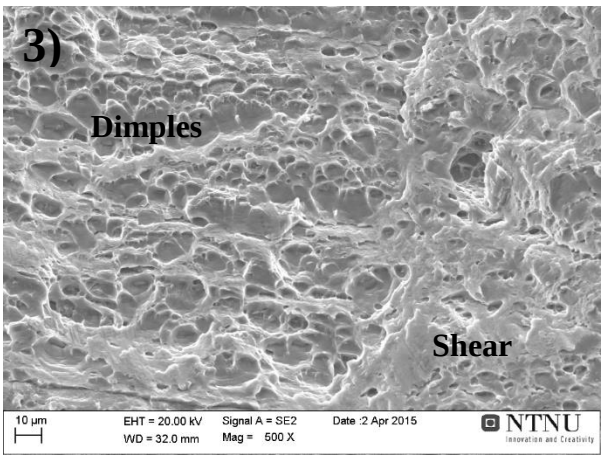

Figure 157: 3) The final fracture, a mixed mode of micro shear and dimples, 500X magnification.

Appendix D – Inverse pole figures

AA6082

The inverse pole figures are displayed in Figure 158 (T1 temper) and Figure 159 (T6 temper) In both figures the {111} planes gives the largest deflection and they have the same texture.

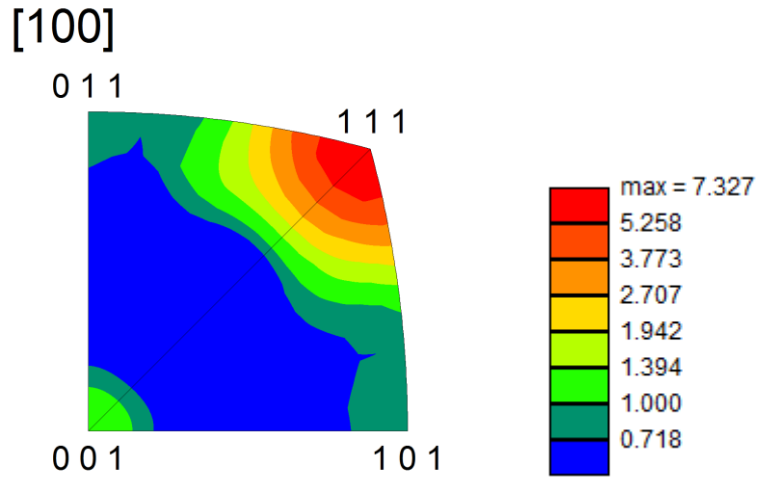

Figure 158: The inverse (100)-pole figure of AA6082 T1 for the entire TD-ND-plane, with an intensity bar to the right.

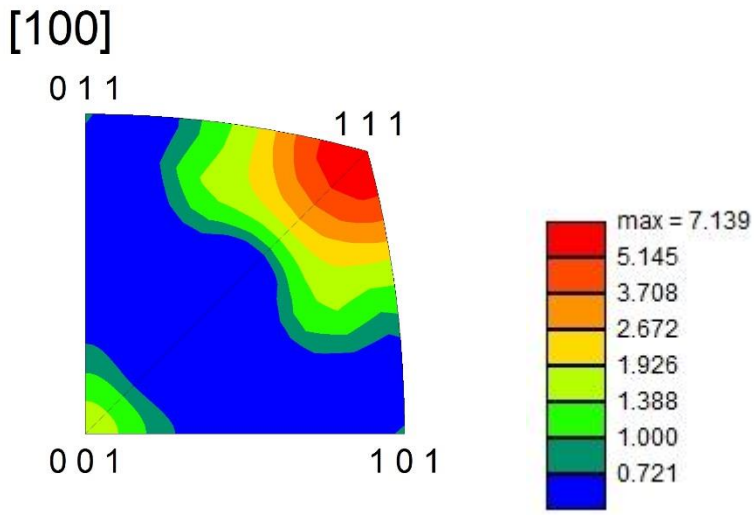

Figure 159: The inverse (100)-pole figure of AA6082 T6 for the entire TD-ND-plane, with an intensity bar to the right.

AA7108

The inverse pole figures are displayed in Figure 160 (T1 temper) and Figure 161 (T6 temper). In both figures the {111} planes gives the largest deflection and they have the same texture.

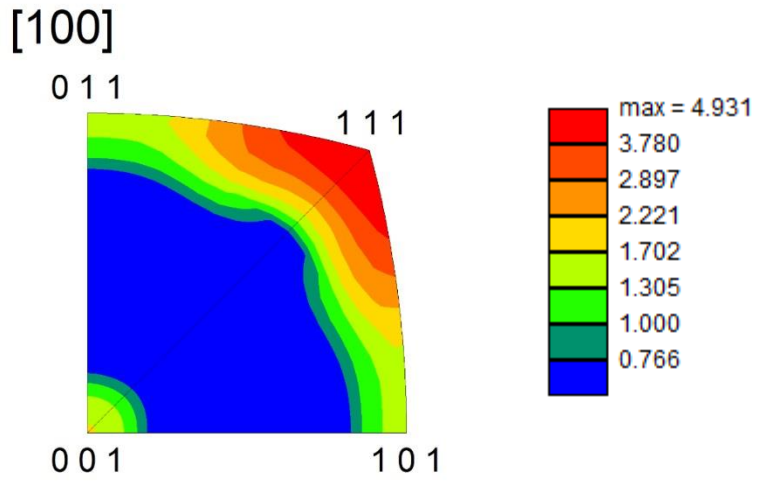

Figure 160: The inverse (100)-pole figure of AA7108 T1 for the entire ND-TD-plane, with an intensity bar to the right.

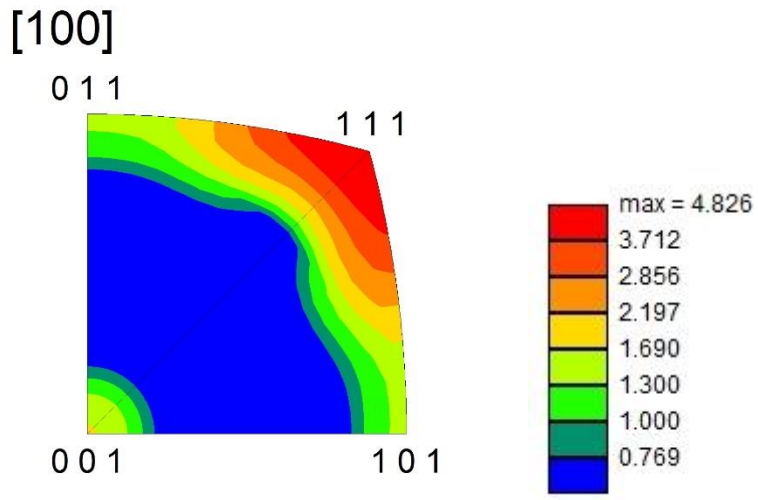

Figure 161: The inverse (100)-pole figure of AA7108 T6 for the entire ND-TD-plane, with an intensity bar to the right.